

Advances in Radiation Heat Transfer and Applied Optics, Including Application of Machine Learning

Mehran Yarahmadi

Dissertation submitted to the faculty of the Virginia Polytechnic Institute and
State University in fulfillment of the requirements for the degree of

Doctor of Philosophy
In
Mechanical Engineering

James R Mahan, Chair

Brian Vick

Vinh Nguyen

Scott Huxtable

December 15, 2020

Blacksburg, Virginia

Keywords: Radiation Heat Transfer, Monte Carlo Ray-Trace Method, Machine
Learning, Applied Optics

Abstract

Advances in Radiation Heat Transfer and Applied Optics, Including Application of Machine Learning

Mehran Yarahmadi

Artificial neural networks (ANNs) have been widely used in many engineering applications. This dissertation applies ANNs in the field of radiation heat transfer and applied optics. The topics of interest in this dissertation include both forward and inverse problems.

Forward problems involve applications in which numerical simulation is expensive in terms of time consumption and resource utilization. Artificial neural networks can be applied in these problems for speeding up the process and reducing the required resources. The Monte Carlo ray-trace (MCRT) method is the state-of-the-art approach for modeling radiation heat transfer. It has the disadvantage of being a complex and computationally expensive process. In this dissertation, after first identifying the uncertainties associated with the MCRT method, artificial neural networks are proposed as an alternative whose computational cost is greatly reduced compared to traditional MCRT method.

Inverse problems are concerned with situations in which the effects of a phenomenon are known but the cause is unknown. In such problems, available data in conjunction with ANNs provide an effective tool to derive an inverse model for recovering the cause of the phenomenon. Two problems are studied in this context. The first is concerned with an imager for which the readout power distribution is available and the viewed scene is of interest. Absorbed power distributions on a microbolometer array making up the imager is produced by discretized scenes using a high-fidelity Monte Carlo ray-trace model. The resulting readout array/scene pairs are then used to train an inverse ANN. It is demonstrated

that a properly trained ANN can be utilized to convert the readout power distribution into an accurate image of the corresponding discretized scene. The recovered scene of the imager is helpful for monitoring the Earth's radiant energy budget.

In the second problem, the collection of scattered radiation by a sun-photometer, or aureolemeter, is simulated using the MCRT method. The angular distribution of this radiation is summarized using the probability density function (PDF) of the incident angles on a detector. Atmospheric water cloud droplets are known to play an important role in determining the Earth's radiant energy budget and, by extension, the evolution of its climate. An extensive dataset is produced using an improved atmospheric scattering model. This dataset is then used to train and test an inverse ANN capable of recovering water cloud droplets properties from solar aureole observations.

General Audience Abstract

Advances in Radiation Heat Transfer and Applied Optics, Including Application
of Machine Learning

Mehran Yarahmadi

This dissertation is intended to extend the research in the field of theoretical and experimental radiation heat transfer and applied optics. It is specifically focused on efforts for more precisely implementing the radiation heat transfer, predicting the temperature evolution of the Earth's ocean-atmosphere system and identifying the atmospheric properties of the water clouds using the tools of Machine learning and artificial neural networks (ANNs). The results of this dissertation can be applied to the conception of advanced radiation and optical modeling tools capable of significantly reducing the computer resources required to model global-scale atmospheric radiation problems. The materials of this thesis are organized for solving the following three problems using ANNs:

1: Application of artificial neural networks into radiation heat transfer

The application of artificial neural networks), which is the basis of AI methodologies, to a variety of real-world problems is an on-going active research area. Artificial intelligence, or machine learning, is a state-of-the-art technology that is ripe for applications in the field of remote sensing and applied optics. Here a deep-learning algorithm is developed for predicting the radiation heat transfer behavior as a function of the input parameters such as surface models and temperature of the enclosures of interest. ANN-based algorithms are very fast, so developing ANN-based algorithms to replace ray trace calculations, whose execution currently dominates the run-time of MCRT algorithms, is useful for speeding up the computational process.

2. Numerical focusing of a wide-field-angle Earth radiation budget imager using an Artificial Neural Network:

Traditional Earth radiation budget (ERB) instruments consist of downward-looking telescopes in low earth orbit (LOE) which scan back and forth across the orbital path. While proven effective, such systems incur significant weight and power penalties and may be susceptible to eventual mechanical failure. This dissertation intends to support a novel approach using ANNs in which a wide-field-angle imager is placed in LOE and the resulting astigmatism is corrected algorithmically. The application of this technology is promising to improve the performance of freeform optical systems proposed by NASA for Earth radiation budget monitoring.

3: Recovering water cloud droplets properties from solar aureole photometry using ANNs:

Atmospheric aerosols are known to play an important role in determining the Earth's radiant energy budget and, by extension, the evolution of its climate. Data obtained during aerosol field studies have already been used in the vicarious calibration of space-based sensors, and they could also prove useful in refining the angular distribution models (ADMs) used to interpret the contribution of reflected solar radiation to the planetary energy budget. Atmospheric aerosol loading contributes to the variation in radiance with zenith angle in the circumsolar region of the sky. Measurements obtained using a sun-photometer have been interpreted in terms of the aerosol single-scattering phase function, droplet size distribution, and aerosol index of refraction, all of which are of fundamental importance in understanding the planetary weather and climate. While aerosol properties may also be recovered using lidar, this dissertation proposes to explore a novel approach for recovering them via sun-photometry. The atmospheric scattering model developed here can be used to produce the extensive dataset required to compose, train, and

test an artificial neural network capable of recovering water cloud droplet properties from solar aureole observations.

Dedication

I dedicate this dissertation work to my dear family. A special feeling of love and gratitude to my parents, Ghodrat and Fatemeh whose encouragement always supported me throughout the process. My brother, Mostafa, and sister, Minoo who never left my side and are very special to me.

I also dedicate this dissertation to my many friends for their understanding and encouragement in many moments of crisis. They are always in my mind and their friendship makes my life a wonderful experience.

Finally, I would like to dedicate this dissertation to Professor J.R. Mahan. This little dissertation is the fruit of the training which I have been receiving from him for the last 3 years. I am deeply blessed for having such a great academic father whom I always had his great support and continuous care.

Acknowledgment

I would like to thank Dr. Brian Vick, Dr. Vinh Nguyen and Dr. Scott Huxtable for their will to serve on my advisory committee.

I would like to appreciate Dr. Kory J. Priestley and Dr. Anum Barki Ashraf of the NASA Langley Research Center for their invaluable assistance to my research. I would like to thank NASA and Science Systems and Applications, Inc. (SSAI), for supporting this research under contract NNL16AA05C, and Subcontract No. 21606-16-036, Task Assignment M.001C (CERES) with Virginia Tech.

I would also like to thank Dr. Kevin McFall for guiding me over questions on artificial intelligence. His insight and knowledge were vital in steering me through the research.

Finally, I would also like to thank my colleagues in Thermal Radiation Group at Virginia Tech. I am in particular thankful to Pat Meehan for his significant help and contribution to this study.

Table of Contents

Preface	1
Chapter 1: Introduction	3
1.1. Brief review of the Monte Carlo ray-trace (MCRT) method	3
1.2. Two-dimensional enclosures in radiation heat transfer	8
1.3. Uncertainty analysis in the MCRT method	11
1.4. An alternative to the MCRT method	11
Chapter 2: Two-Dimensional Monte Carlo Ray-Trace Methodology	13
2.1. Problem description	14
2.2. Finding the minimum length of the three-dimensional industrial oven	16
2.3. Two-dimensional MCRT method	17
2.4. Results and discussion	19
Chapter 3: Uncertainty Analysis in the MCRT Environment – Part 1	21
3.1. Radiation distribution factors in the absence of a participating medium	22
3.2. Importance of establishing the accuracy of the MCRT method	24
3.3. Uncertainty formulation	27
3.3.1. Uncertainty in the distribution factors	27
3.3.2. Uncertainty in heat transfer results	29
3.4. Validation of the uncertainty formulation	34
3.4.1. Example Problem 1	34
3.4.1.1. Validation of the distribution factor mean uncertainty relation for Example Problem 1	36
3.4.1.2. Validation of the net heat flux uncertainty predictor for Example Problem 1	38
3.4.2. Example Problem 2	40
3.4.2.1. Validation of the distribution factor mean uncertainty relation for Example Problem 2	41
3.4.2.2. Validation of the net heat flux uncertainty predictor for Example Problem 2	42
3.4.3. Discussion of the distribution factor mean uncertainty results	43
3.5. Experimental design of MCRT algorithms	46
3.6. Conclusions and recommendations	48
Chapter 4: Uncertainty Analysis in the MCRT Environment – Part 2	50
4.1. Median of the distribution factor histogram and its importance	51
4.2. Statistical properties of the distribution factor matrix	53
4.3. Experimental study of skew for two-dimensional enclosures	55
4.4. Discussion and interpretation of results	69
4.5. Conclusions	71

Chapter 5: Introduction to the Artificial Neural Network (ANN)	73
5.1. Background	74
5.2. The ANN in thermal applications	74
5.3. Description of the ANN	75
5.3.1. An example of ANN application	78
Chapter 6: Artificial Neural Networks in Radiation Heat Transfer Analysis	81
6.1. Motivation	82
6.2. The ANN as the alternative approach	83
6.2.1. Case Study 1: A long box channel with uniform emissivity.	83
6.2.2. Case Study 2: A long box channel with non-uniform emissivity.	89
6.2.3. Case Study 3: A long box channel with an interior obstruction.	95
6.3. Conclusions and recommendations	98
Chapter 7: Numerical Focusing Using an Artificial Neural Network	99
7.1. Introduction	100
7.2. Image deblurring	104
7.3. Instrument model	109
7.4. Use of the Artificial Neural Network	111
7.5. Implementation and results	112
7.6. Summary and conclusions	118
Chapter 8: Recovery of Water Cloud Properties Using an Artificial Neural Network	120
8.1. Introduction	121
8.2. Simulation of scattering in water clouds	122
8.2.1. Mie scattering in the MCRT environment	122
8.2.2. Cloud properties	125
8.2.3. MCRT-based multiple scattering simulation	129
8.2.4. Parameterization of the PDF profile	136
8.3. Property recovery using an Artificial Neural Network (ANN)	138
8.3.1. Creation and training of the ANN	139
8.3.2. ANN implementation	140
8.4. Results	141
8.5. Discussion	145
8.6. Conclusions and Recommendations	147
References	148

Preface

This dissertation is the enduring record of the author's contributions to expanding the scope and utility of radiation heat transfer pedagogy and practice, with particular emphasis on the roles played by Monte Carlo ray-trace (MCRT) method and machine learning. The results of this dissertation can be applied to the conception of advanced radiation and optical modeling tools to significantly reduce the computer resources required to model global-scale atmospheric radiation and the instruments intended for its measurement.

This document includes evaluation of the accuracy of the MCRT method, which is required to evaluate the performance of next-generation instruments intended to monitor the Earth's radiant energy budget in support of ongoing climate studies. It also contains the extension of the MCRT method to other fields, in particular to applied optics, and the marriage of the MCRT and machine learning to accelerate the applications involving radiation heat transfer and applied optics.

The dissertation is organized around a series of peer-reviewed journal articles, augmented by unpublished original research, describing groundbreaking contributions by the author in the course of his doctoral research. Chapter 1 introduces and briefly reviews the MCRT method and prepares the ground for other chapters in which this method is used to model radiation heat transfer. Chapter 2 reviews the two-dimensional MCRT environment and evaluates the legitimacy of the methods used for radiation analysis in long enclosures. This chapter is important since the two-dimensional MCRT method is frequently used

throughout this dissertation. Chapters 3 and 4 evaluate the accuracy of the MCRT method and provide formal statistical methodology for reporting the uncertainty in a Monte Carlo ray-trace analysis. Chapter 5 is an introduction to artificial neural networks (ANNs), a state-of-the-art technology that is ripe for applications in the field of remote sensing and applied optics. Chapter 6 documents the development of an ANN-based method to replace ray-tracing in order to speed up the computational process in a radiation heat transfer analysis. Chapter 7 is the extension of the MCRT method and ANNs to the field of applied optics, and presents a remarkable application for numerical focusing used in monitoring the earth's radiant energy budget. Finally, Chapter 8 demonstrates a significant example of the simultaneous use of MCRT method in a participating medium and ANNs in the field of atmospheric science with the target of water cloud properties recovery.

Mehran Yarahmadi
Blacksburg
December 2020

Chapter 1:

Introduction

1.1. Brief review of the Monte Carlo ray-trace (MCRT) method

Radiation is the dominant mode of heat transfer in many applications of practical engineering interest. These include situations, such as instrumentation, cryogenics, solar energy utilization, and certain space applications, where other modes of heat transfer have been suppressed or eliminated. Radiation is also important in high-temperature processes, such as those associated with electronics, thermal plasmas, combustion, and detonation.

The Monte Carlo ray-trace method [1-3] has emerged as the dominant tool for formulating high-fidelity models (HFMs) of radiation heat transfer processes. This is because of its universal applicability to problems involving radiant exchange among surfaces and within participating media, the ease with which it conforms to complicated irregular geometries, and its ability to treat directional and wavelength-dependent optical properties. The Monte Carlo ray-trace method is a statistical solution technique in which energy bundles are traced as they are emitted, scattered, and absorbed within an enclosure. The method produces very accurate solutions within limits of statistical accuracy which can be estimated to a stated level of confidence. In addition to the applicability of the MCRT method in complex

geometries, it is also a very flexible method and benefits from a straightforward formulation that enables easier handling of further complexities such as directionally absorbing and reflecting surfaces and directional scattering in participating media [2, 3]. Furthermore, compared to other methods such as the finite-volume method (FVM), the Zonal method, the discrete ordinates method (DOM), the discrete transfer method (DTM), and the finite element method (FEM), the MCRT method, when properly formulated, avoids the ray effect and false scattering [4]. With the emergence of the Monte Carlo ray-trace method as the predominate tool in radiation heat transfer analysis, it has become artificial to separate the disciplines of radiation heat transfer and applied optics. The method is briefly reviewed here.

In thermodynamics, a system is a region of space or a quantity of matter set aside for study. It includes anything whose thermodynamic properties are of interest and is embedded in and intersected with its surroundings, or environment. In radiation heat transfer, the system of interest is the enclosure which is the central and essential concept in all approaches to radiation heat transfer. It is defined as an ensemble of surfaces, both real and imaginary, bounding a closed volume such that a ray, once having entered the volume, cannot escape. Energy is conserved within the enclosure under this definition. In the event that a ray does leave the enclosure through an opening, represented by an imaginary surface, the energy it carries is deducted from the overall energy balance.

The Monte Carlo ray-trace (MCRT) method as commonly practiced by the radiation heat transfer community begins with the creation of a matrix of *radiation distribution factors*, defined here and elsewhere [2, 3] as

$$D_{ijk} \equiv Q_{a,ijk}/Q_{e,ik}, \quad 1 \leq i \leq n, \quad 1 \leq j \leq n, \quad 1 \leq k \leq K. \quad (1-1)$$

In Eq. (1-1), n is the number of surface and volume elements making up the enclosure; K is the number of wavelength intervals, or bands, occupied by the

radiation; $Q_{e,ik}$ is the power emitted by surface or volume element i in band k ; and $Q_{a,ijk}$ is the power emitted by surface or volume element i that is absorbed by surface or volume element j in band k . Equation (1-1) is completely general in that it holds whether the radiative interchange is among surface or volume elements or a combination of the two, without regard to the directionality or wavelength dependence of surface or volume properties.

It is perhaps worth noting that the distribution factor considered here is distinctly different from the *geometrical factor*—also variously referred to as the *angle factor*, the *shape factor*, the *view factor*, and the *configuration factor*—which dominated radiation heat transfer pedagogy and practice in the second half of the 20th C [5-13]. Several such factors have been defined and used down through the years to calculate radiant exchange, but the distribution factor defined by Eq. (1-1) lies at the heart of the MCRT method. The earliest mention of this quantity is attributed to Gebhart, who refers to it as the *absorption factor* in a 1961 article [14]. Gebhart showed that, for the special case of a gray diffuse enclosure, the elements of his absorption factor matrix could be constructed from surface properties and geometrical factors. In 1968, Howell [15] introduced the term *exchange fraction* for the version of the absorption factor evaluated using the Monte Carlo method. Later Mahan and Eskin [16, 17] refer to this same quantity as the *radiation distribution factor* because of its essential role in distributing radiation emitted by surface or volume element i to surface or volume element j . While this latter term is in common usage, other authorities refer to the distribution factor as the *exchange factor* [18-20], although the exchange factor used by Yuen [20] is more directly akin to Gerhart's absorption factor since it is evaluated analytically without recourse to ray-tracing. Finally, Larsen and Howell [21] attribute the term exchange factor to a family of auxiliary factors that, when used together, describe radiative exchange in the zonal method. It should also be noted that Lin and Sparrow [22] use the term exchange factor to describe radiant

interchange among a mixture of diffuse and specular surfaces in the net-exchange method.

If the enclosure contains a participating medium and the first N out of n are surface elements and the remaining $n - N$ are volume elements, then the power absorbed by surface or volume element i is [3]

$$Q_{i,a} = \Delta A_i \sum_{k=1}^K \left[\varepsilon_{ik} \sum_{j=1}^N e_b(\Delta\lambda_k, T_j) D_{ijk} \right] + 4\pi\Delta V_i \sum_{k=1}^K \left[\kappa_{ik} \sum_{j=N+1}^n i_b(\Delta\lambda_k, T_j) D_{ijk} \right], \quad (1-2)$$

and the power emitted by surface or volume element i is

$$Q_{i,e} = \begin{cases} \Delta A_i \sum_{k=1}^K \varepsilon_{ik} e_b(\Delta\lambda_k, T_i), & 1 \leq i \leq N \\ 4\pi\Delta V_i \sum_{k=1}^K \kappa_{ik} i_b(\Delta\lambda_k, T_i), & N + 1 \leq i \leq n, \end{cases} \quad (1-3)$$

In Eqs. (1-2) and (1-3), ΔA_i is the area of surface element i , ΔV_i is the volume of volume element i , ε_{ik} is the emissivity of surface element i in band $\Delta\lambda_k$, κ_{ik} is the absorption coefficient of volume element i in band $\Delta\lambda_k$, $e_b(\Delta\lambda_k, T_j)$ is the blackbody emissive power in band $\Delta\lambda_k$ corresponding to temperature T_j , $i_b(\Delta\lambda_k, T_j)$ is the blackbody intensity in band $\Delta\lambda_k$ corresponding to temperature T_j , and D_{ijk} is the band-wise spectral radiation distribution factor in band $\Delta\lambda_k$. The net power emitted from surface or volume element i is then

$$Q_i = Q_{i,e} - Q_{i,a}. \quad (1-4)$$

It is emphasized here that the validity of Eqs. (1-2) and (1-3) is independent of the dimensionality of the enclosure; once the distribution factors have been obtained, these equations are equally valid for both two- and three-dimensional enclosures.

Two main approaches are available to generate random numbers. The first method measures some physical phenomenon which is expected to be random and then compensates for possible biases in the measurement process. Example sources include measuring atmospheric noise, thermal noise, and other external electromagnetic and quantum phenomena. The second method uses computational algorithms that can produce long sequences of apparently random results, which are in fact completely determined by an initial value, known as a seed. The entire seemingly random sequence can be reproduced if the seed value is known. This type of random number generator is often called a pseudorandom number generator (PRNG) [23]. MCRT approach is highly dependent on the availability of a fast, efficient random number generator. Only pseudo-random number generators, which use deterministic formulas to produce a sequence of numbers, are used in this dissertation. The details of a good pseudo-random number generator are discussed in detail in Ref [3]. Some authorities prefer quasi-random number generators (QRNG) which produce a sequence not intended to be random but rather intended to be distributed as uniformly as possible. In a study, Farmer et al. [24] presented a novel approach based on a low-discrepancy sequence (LDS) for a Monte Carlo-based radiation solver. They used Sobols sequence, an LDS generated operator, to develop a quasi-Monte Carlo (QMC) solver for thermal radiation. In this dissertation when reference is made to a random number it is understood to mean a pseudo-random number.

Two-dimensional enclosures in the context of the MCRT method for radiation analysis have been widely studied in the literature. Section 1.2 highlights the importance of two-dimensional enclosures in MCRT radiation heat transfer analysis.

1.2. Two-dimensional enclosures in radiation heat transfer

The usual starting point in radiation heat transfer analysis is to define an enclosure whose walls are typically subdivided into surface elements of size depending on the desired spatial resolution. It is sometimes convenient to treat the enclosure as being two-dimensional. This occurs when one of the three dimensions is long compared to the other two, as in the case of ducts, grooves, channels, and certain industrial process lines.

Because of their relative simplicity, two-dimensional enclosures have been widely studied in the radiation heat transfer literature to establish epistemology regarded as independent of dimensionality. For example, Chang et al. [25] have investigated the effect of radiation on combined heat transfer with convection or conduction in a participating medium within a two-dimensional enclosure. Ramankutty et al. [26] demonstrate a modified discrete ordinates solution of radiative transfer in two-dimensional rectangular enclosures. Ismail and Salinas [27] study the application of a multidimensional scheme using the discrete ordinate method in a two-dimensional enclosure with diffusely emitting and reflecting walls. Hayasaka et al. [28] consider the radiative heat-ray method in a two-dimensional model. Jinbo et al. [29] investigate the radiative heat fluxes and temperatures under the assumption of isotropic scattering in a two-dimensional stationary rectangular configuration. Two-dimensional systems have also been investigated for numerical studies of radiation in water droplet systems [30-35].

Many investigators have used two-dimensional enclosures for inverse boundary design in radiation heat transfer. Li [36] considers the inverse problem of an unknown source term in a two-dimensional rectangular medium with transparent boundaries. Sarvari et al. [37, 38] present an inverse analysis for finding the heat source distribution in an irregular enclosure to produce both desired temperature and heat flux profiles over the design surface of an irregular two-dimensional enclosure with participating media. Tito et al. [39] consider inverse radiative

transfer problems in two-dimensional rectangular enclosures containing heterogeneous isotropic scattering or linear anisotropic scattering in participating media. Daun et al. [40, 41], use optimization methods for finding the heater settings that provide spatially uniform transient heating within a two-dimensional radiant enclosure. The variable metric method is utilized by Kowsary et al. [42] to investigate the radiative boundary design problem in a two-dimensional furnace filled with an absorbing, emitting and scattering gas. The conjugate gradient method has been applied to inverse boundary design problems in an irregular two-dimensional enclosure with participating media by Pourshaghaghay et al. [43]. Mehraban et al. [44] present an inverse radiation design problem for finding the transient heater settings that produce transient conditions over products in two-dimensional radiant furnaces. Salinas [45] presents an optimization analysis for temperature field estimation in a two-dimensional gray medium. Bayat et al. [46] use the conjugate gradient method to investigate an optimization procedure to determine the heater powers of a radiant enclosure to achieve a uniform heat flux distribution over a diffuse-spectral temperature-specified design surface in a two-dimensional radiant furnace. Amiri et al. [47] employ an inverse analysis to estimate the required input on the heater surface that produces the desired temperature and heat flux distribution over the design surface of a two-dimensional enclosure.

The inverse boundary design problem for combined radiation and either convection or conduction heat transfer in two-dimensional enclosures has also been studied. An optimization technique has been applied to the design of two-dimensional heat transfer systems in which both conduction and radiation are important [48]. Kim et al. [49] investigate an inverse problem based on the finite volume method for conduction and radiation in a two-dimensional cylindrical enclosure. Mossi et al. [50] report an inverse boundary design problem involving radiation and convection in a two-dimensional cavity. Moghadassian et al. [51] investigate the inverse boundary design problem in combined natural convection

and radiation heat transfer with the presence of a participating medium in a two-dimensional square.

Numerous two-dimensional studies have been based on the Monte Carlo ray-trace method. Oguma and Howell [52] investigate the solution of two-dimensional blackbody inverse radiation problems by the reverse Monte Carlo method. Erturk [53] considers a two-dimensional inverse design approach using a combination of MCRT and regularization methods. Baek et al. [54] consider a combination of the Monte-Carlo and finite-volume methods (CMCFVM) for solving radiative heat transfer in absorbing, emitting, and isotropically scattering medium with an isolated boundary heat source in a two-dimensional irregular geometry. Safavinejad et al. [55] use a micro-genetic algorithm to solve the inverse boundary design problem in two-dimensional radiant enclosures with absorbing–emitting media, making use of the Monte Carlo method (MCM) to solve the equation of radiative transfer. In a second contribution, they use the same method to optimize the number and location of the heaters in two-dimensional radiant enclosures composed of specular and diffuse surfaces [56]. Mosavati et al. [57] apply the MCRT method in a two-dimensional enclosure for calculating distribution factors used in an inverse design problem. By employing the reverse Monte Carlo method for computing the distribution factors, they also solve the boundary inverse design in a step-like two-dimensional enclosure with gray walls and a transparent medium with combined radiation-free convection [58]. In another study, Mulford et al. [59] apply two-dimensional Monte Carlo ray-tracing to calculate the apparent absorptivity of a diffusely-irradiated V-groove and the apparent absorptivity of a fully illuminated cavity subject to collimated irradiation. Yarahmadi et al. [60] use two-dimensional radiant enclosures in an inverse boundary design in radiation heat transfer using a Fourier cosine series. In a recent contribution, Vick et al. [61] investigate two-dimensional enclosures for the numerical modeling of combined radiation and conduction heat transfer using the discrete Green’s function (DGF) method.

In contrast to heat conduction and other boundary value problems, the Monte Carlo ray-trace method does not involve solution of differential equations but rather is based on the rules of statistics and geometrical optics. The rules governing diffuse emission and reflection in a three-dimensional enclosure are well established [2, 3]; however, it seems that the rules governing a two-dimensional ray-trace, while perhaps intuitively obvious and certainly widely used, have yet to be rigorously established in the literature. In Chapter 2 of this dissertation, the frequent use of the two-dimensional approximation for elongated enclosures is critically examined.

1.3. Uncertainty analysis in the MCRT method

A critical portion of any radiation heat transfer analysis involves assessing the accuracy of the results obtained. To this end, formal techniques are required for determining uncertainty of radiative heat flux and identifying the minimum number of rays per surface element required to achieve the desired accuracy [62]. To further enhance the value of MCRT method, contributions are required to establish a statistically meaningful paradigm for estimating the uncertainty, to a stated level of confidence, of predicted heat transfer results. In Chapters 2 and 3, new methods are explored for directly and quantitatively analyzing the accuracy of the MCRT method for representing radiative transfer. The results presented in these two chapters underscore the importance of uncertainty analysis for MCRT method. These two chapters are important not only because of their value in assessing the uncertainty of a MCRT analysis, but also because they enable a radiation experimental design paradigm which is important for minimizing the computational cost associated with ray-tracing.

1.4. An alternative to the MCRT method

A widely lamented disadvantage of the MCRT method is the excessive computational cost associated with achieving high accuracy when fine spatial

resolution is required. The fact that rays are mutually independent entities permits massive parallelization, with a proportionate reduction in processor time; however, associated cost, power, volume, and weight penalties exclude massive parallelization in applications where real-time results are required for data interpretation and decision-making on board autonomous space probes [63] and fire-and-forget weapons [64]. In an MCRT environment, when the number of surface elements n is large and high accuracy is required, an exceedingly large number of rays must be traced. Furthermore, because D_{ij} depends on the emissivity ε_i , computational costs can become excessive for optimization processes in which ε_i is a parameter. This motivates the search for a computationally less intensive approach.

The alternative to a slow or computationally ponderous high-fidelity model (HFM) in such applications would be a reduced-order model (ROM) that provides comparable accuracy and spatial resolution but in real time and with significantly reduced hardware requirements [65]. In Chapter 5, Artificial neural networks (ANNs) are introduced as a potential tool for an alternative approach whose computational cost is greatly inferior to that of the traditional MCRT method. Chapter 6 explores the idea of using the ANNs as a substitute to ray-tracing in radiation heat transfer applications involving diffuse gray enclosures in the absence of a participating medium, and Chapter 7 explores another application of ANNs as a viable means for creating computationally efficient ROMs of complex optical systems from computationally intensive HFMs based on the MCRT method. This latter chapter is an example of the intersection between radiation heat transfer and applied optics and demonstrates the extendibility of MCRT method to practical optical applications. Finally, Chapter 8 explores an example of radiation in a participating medium which uses MCRT method and ANNs in the field of atmospheric science. This chapter presents a methodology for recovering the properties of water clouds.

Chapter 2:

Two-Dimensional Monte Carlo Ray-Trace Methodology

In spite of the frequent appearance in the radiation heat transfer literature of articles describing Monte Carlo ray-trace (MCRT) applications to two-dimensional enclosures, no formal verification may be found of the method commonly used to determine the directional distribution of diffuse emission and reflection when estimating two-dimensional radiation distribution factors. In this chapter, we investigate two candidate methods for determining the direction of diffuse emission and reflection for ray-tracing in a two-dimensional MCRT analysis. To evaluate the legitimacy of the two methods, the results obtained using the two-dimensional analysis are compared with those obtained for an equivalent three-dimensional enclosure in the limit as its long dimension is extended. The contents of this chapter are also available online [66].

2.1. Problem description

Consider the radiation problem, illustrated in Fig. 2.1, involving a two-dimensional industrial oven whose work piece produces a step-like geometry. All surfaces are considered to be gray and diffuse with an emissivity of 0.8, and the interior medium is assumed to be non-participating. This enclosure has been selected because it is a benchmark geometry in the literature [40, 42, 43, 47, 56-58, 60, 61]. The problem is to first calculate the distribution factor matrix for this enclosure using the two-dimensional MCRT method, and then compare the results with those describing the equivalent elongated three-dimensional enclosure that it is intended to represent. The total number of surface elements for this problem is selected to be 40. Figure 2.2 shows the equivalent three-dimensional enclosure. Note that for

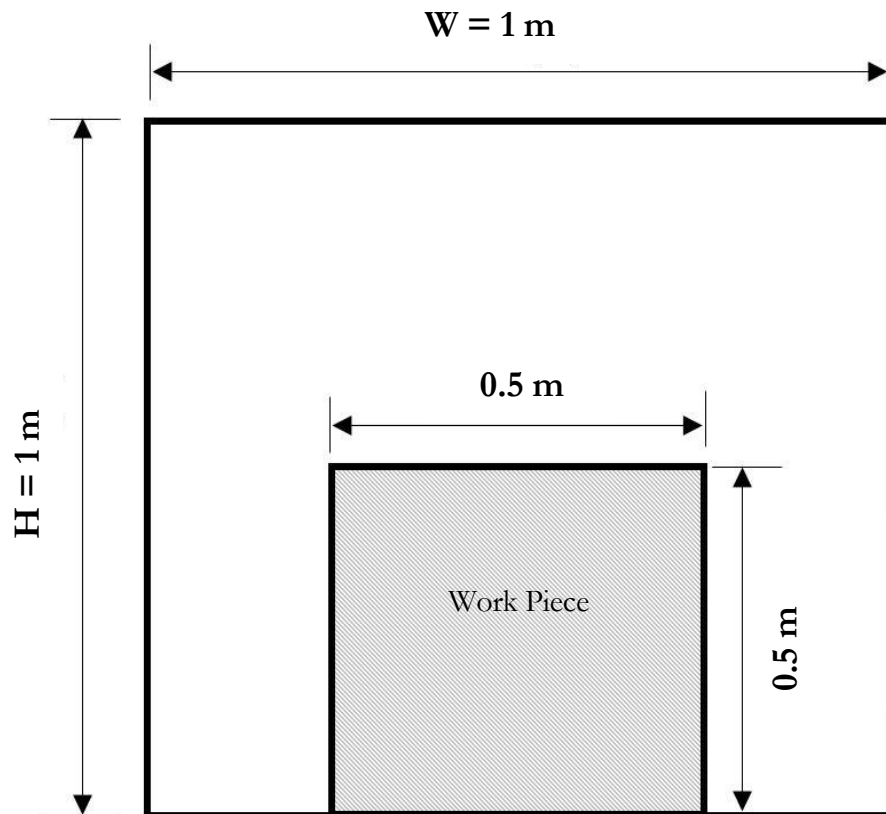


Figure 2.1. Cross-section of the two-dimensional industrial oven.

comparison of the results of two-dimensional and three-dimensional enclosures, the surface elements in three-dimensional enclosures are chosen to be long strips, as indicated by surface elements 19 and 30 in Fig. 2.2.

The radiation distribution factors are most easily determined using the Monte Carlo ray-trace method, as detailed by Mahan [3]. Briefly, the steps for obtaining these factors for a diffuse-gray enclosure are:

- (1) Randomly distributed points from which discrete rays are launched from any given surface element are selected based on the values of two random numbers.
- (2) Directions of diffuse emission are determined by drawing two additional random numbers from which azimuth and zenith angles are calculated.
- (3) The intersection point of the emitted rays with the enclosure interior surface is determined by solving the equations for the surface simultaneously with the three equations for the line representing the ray.

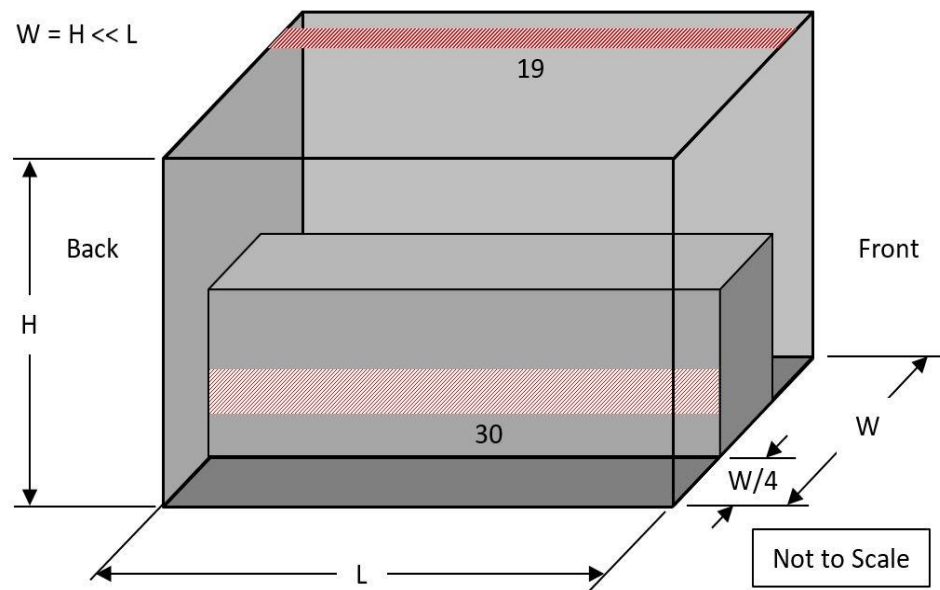


Figure 2.2. Isometric view of the long three-dimensional industrial oven ($W = H = 1$ m).

(4) Whether the ray is reflected or absorbed by the surface intersected by the ray is determined by drawing a fifth random number and comparing its value to the surface absorptivity. If the random number is less than the absorptivity, the ray is absorbed and its history is terminated. In this case the count of the number of rays absorbed by the intersected surface element is incremented.

(5) If the ray is reflected, the diffuse direction is determined by returning to Step 2 and repeating the procedure until the ray is finally absorbed by one of the surfaces of the enclosure. The ratio of the number of rays absorbed by surface j to those emitted from surface i is an estimator of the radiation distribution factor D_{ij} , whose accuracy depends on the number of rays emitted.

The uncertainty of the results obtained using the MCRT method may result from the measuring errors of parameters such as temperature and emissivity. Uncertainty inherent to the MCRT environment is treated in detail in Chapters 3 and 4.

2.2. Finding the minimum length of the three-dimensional industrial oven

A numerical experiment has been carried out using a standard three-dimensional Monte Carlo ray-trace for oven lengths starting from 1 m and increasing in steps of 1 m. Figure 2.3 is a plot of the fraction, D_{ij} , of the energy emitted from two surface elements ($i = 19$ or 30), indicated as strips in Fig. 2.2, that is absorbed on either the front or back surface ($j = \text{front or back}$) of the three-dimensional enclosure. When the length L is 100 m, the fraction of energy emitted by elements 19 and 30 and absorbed by the front or back surfaces is only 0.17 percent and 0.10 percent, respectively. Therefore, it is reasonable to assume that the three-dimensional oven with a length of $L = 100$ m can be considered a two-dimensional enclosure.

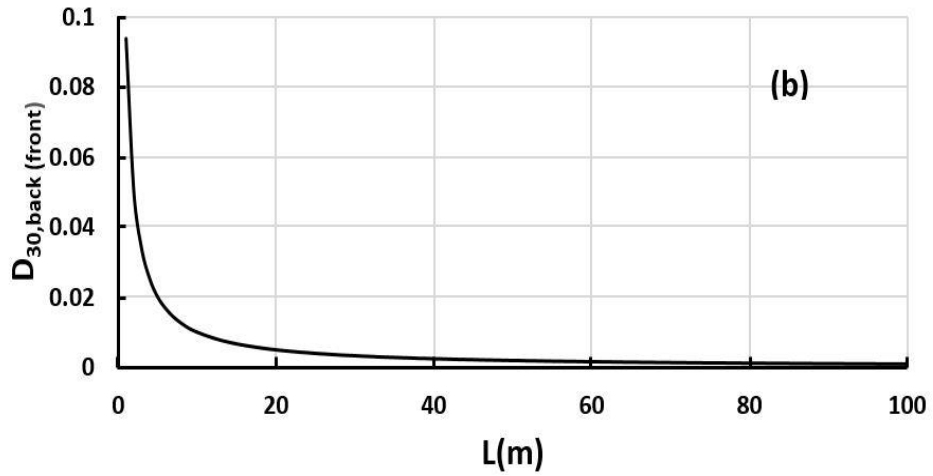
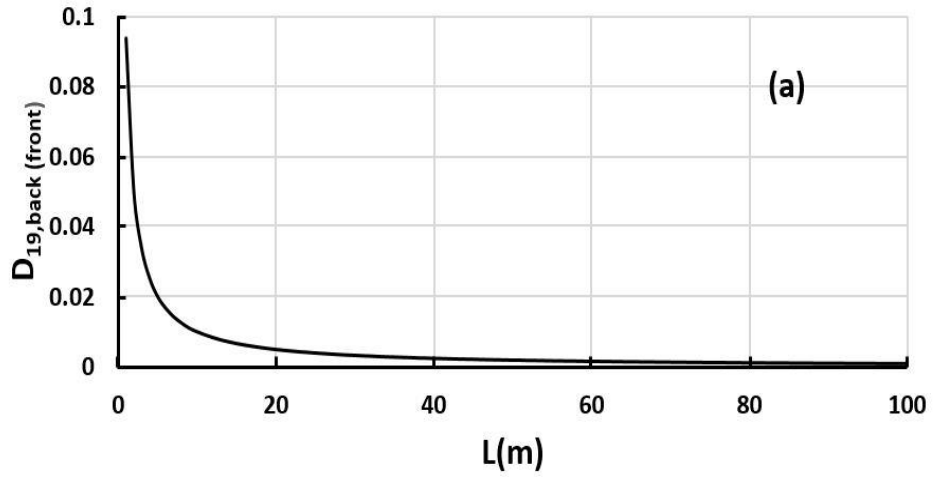


Figure 2.3. Distribution factor value from two selected three-dimensional elements, (a) 19 and (b) 30, to the back (front) surfaces.

2.3. Two-dimensional MCRT method

The only difference between the two-dimensional MCRT method and the three-dimensional method is the algorithm for computing the direction of diffuse emission and reflection. For three-dimensional analysis, the direction cosines L , M , and N are determined as [3]

$$L = n_x \cos\theta + t_{1,x} \sin\theta \cos\phi + t_{2,x} \sin\theta \sin\phi, \quad (2 - 1)$$

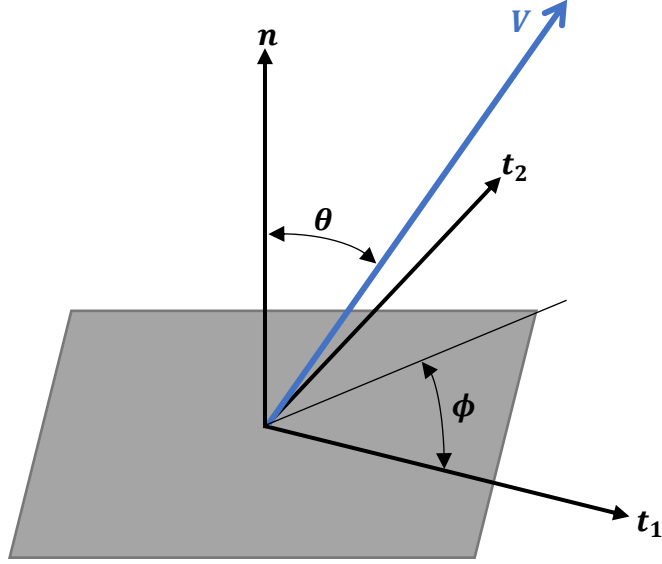


Figure 2.4. Nomenclature for emitted or reflected rays.

$$M = n_y \cos\theta + t_{1,y} \sin\theta \cos\phi + t_{2,y} \sin\theta \sin\phi, \quad (2 - 2)$$

and

$$N = n_z \cos\theta + t_{1,z} \sin\theta \cos\phi + t_{2,z} \sin\theta \sin\phi, \quad (2 - 3)$$

where n , t_1 , and t_2 are the unit normal, first unit tangent, and second unit tangent vectors of each surface element of emission or reflection, and θ and ϕ are zenith and azimuth angles measured with respect to the unit normal and tangent vectors. These two angles are randomly determined by

$$\theta = \sin^{-1}[\sqrt{R_\theta}] \quad \text{and} \quad \phi = 2\pi R_\phi \quad (2 - 4)$$

where R_θ and R_ϕ are random numbers uniformly distributed between zero and unity. Figure 2.4 illustrates the conventions for an emitted or reflected direction.

In three-dimensional geometries we have three direction cosines, while in the two-dimensional analysis we have only two, L and M , with respect to the global x and y axes, respectively. Two methods are investigated for finding the direction cosines of emission in two-dimensional geometries.

First method. This method is based on the same logic as for three-dimensional analysis, and uses two random numbers. Here, the z -axis direction cosine, N , from Eq. (2-3) is forced to be zero, and the values obtained from Eqs. (2-1) and (2-2) are used for the other two direction cosines. Since the emission or reflection vector must be a unit vector, we normalize the values of L and M from Eqs. (2-1) and (2-2), obtaining

$$\mathbf{V} = \left[\frac{L}{\sqrt{L^2 + M^2}}, \frac{M}{\sqrt{L^2 + M^2}} \right]. \quad (2-5)$$

Second method. This method uses only one random number. Here, the angle α with the x -axis is randomly determined as

$$\alpha = 2 \sin^{-1}[\sqrt{R_\alpha}], \quad (2-6)$$

where R_α is again a random number uniformly distributed between zero and unity. Then, for the direction cosines, we have

$$L = n_y \cos\alpha + t_y \sin\alpha \quad (2-7)$$

and

$$M = n_x \cos\alpha + t_x \sin\alpha. \quad (2-8)$$

2.4. Results and discussion

Radiation distribution factors are computed using a windows application written by the author [67] based on the MCRT method to compute the radiation distribution factors among any number of surface elements making up any two-dimensional diffuse gray enclosure. One very effective technique to present the radiation distribution factor values is using histograms. Distribution factor histograms are similar to fingerprints, in that they are apparently unique for any given enclosure. Figure 2.5 shows the distribution factor values obtained using the two two-dimensional methods described above compared with the results for the

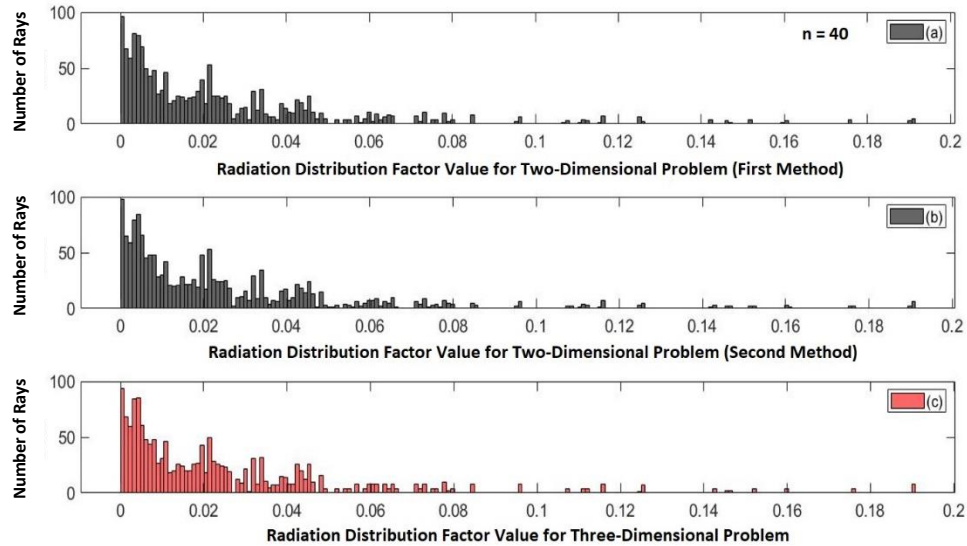


Figure 2.5. Histogram for radiation distribution factors for (a) the two-dimensional problem using Method 1, (b) the two-dimensional problem using Method 2, (c) the three-dimensional problem with $L/H = L/W = 100$. $N = 1$ M rays per surface element is used for ray-tracing.

using Method 2. Method 2 is faster because it only requires a single random number to describe the direction of the emission or reflection; however, both methods yield approximately the same accuracy. The uncertainties of distribution factor estimates are shown to depend on the number of surface elements and the number of rays traced per surface element in Chapter 3. The comparisons made here are based on the same number of surface elements and rays traced, and thus are subject to the same inherent accuracy.

By example, we showed that either of two methods, designated here as Method 1 and Method 2, can be reliably used to compute the radiation distribution factors for a two-dimensional enclosure. Two-dimensional enclosures are widely used in this dissertation as a surrogate for three-dimensional enclosures, and in these cases Method 2 is used for determining the direction cosines of diffuse emission or reflection in a two-dimensional MCRT environment.

Chapter 3:

Uncertainty Analysis in the MCRT Environment – Part 1

Despite the dominant role of the Monte Carlo ray-trace method in modern radiation heat transfer analysis, the contemporary literature remains surprisingly reticent on the uncertainty of results obtained using it. In this chapter, after first identifying the radiation distribution factor as a population proportion, standard statistical procedures are used to estimate its mean uncertainty, to a stated level of confidence, as a function of the number of surface elements making up the enclosure and the number of rays traced per surface element. To evaluate the statistical methodology used here, this *a priori* statistical uncertainty is compared with the observed variability in the distribution factors obtained in an actual MCRT-based analysis. Finally, a formal approach is developed and demonstrated for estimating, to a prescribed level of confidence, the uncertainty in predicted heat

transfer. This approach provides a basis for determining the minimum number of rays per surface element required to obtain a desired accuracy. This chapter is based on a peer-reviewed article by the author published in the **Journal of Heat Transfer** entitled “Uncertainty analysis and experimental design in the Monte Carlo ray-trace environment” [68].

3.1. Radiation distribution factors in the absence of a participating medium

As previously stated in Chapter 1, the *radiation distribution factor* D_{ij} is defined as the fraction of the power *emitted* by surface or volume element i that is *absorbed* by surface or volume element j , due both to direct radiation and to all possible reflection and scattering events [2, 3]. Note that this is not the same entity as the purely geometrical *configuration factor* F_{ij} , defined as the fraction of diffusely distributed power *leaving* (emitted plus reflected) surface i and *arriving at* (but not necessarily absorbed by) surface j by direct radiation only. The configuration factor is central to the *net-exchange*, or *radiosity-irradiance*, method, while the distribution factor lies at the heart of the *Monte Carlo ray-trace (MCRT)* method.

In the MCRT method, the radiation distribution factor D_{ij} can be interpreted as the probability that a ray emitted by surface or volume element i will be absorbed by surface or volume element j . Then in the case of surface-to-surface radiation, which is the topic for this chapter, the direction of emission of a ray from surface element i is determined by treating the directional emissivity as the probability that the ray will be emitted in a specified direction, and the directional absorptivity of surface element j is treated as the probability that a ray incident there from a given direction will be absorbed. Furthermore, if the ray is not absorbed, the direction of reflection is determined by relating the bidirectional reflectivity to the probability that the ray will be reflected in a specified direction. A similar analogy governs radiation in the presence of a participating medium.

The use of distribution factors in the absence of a participating medium implies that the enclosure has been subdivided into a sufficiently large number n of surface elements to achieve the desired spatial resolution of results obtained. The distribution factor matrix for a diffuse gray enclosure, D_{ij} , is populated by tracing a large number of rays as they navigate within an enclosure subject to the rules of geometrical optics and probability. Upon completion of the ray-trace, the ratio of the number of rays N_{ij} emitted from element i and absorbed in element j to the number of rays N_i emitted from element i is taken as the estimate of the distribution factor D_{ij} . In other words, for the enclosure whose walls are gray and diffuse, Eq. (1-1) reduces to

$$D_{ij} \approx \frac{N_{ij}}{N_i}, \quad 1 \leq i \leq n, \quad 1 \leq j \leq n. \quad (3-1)$$

The accuracy of the estimate increases with the number N_i of rays traced. The details of the MCRT method are widely available elsewhere [2, 3].

For the diffuse gray enclosures considered here, and in the absence of a participating medium, if the surface temperature distribution T_j is specified across the surfaces of a diffuse gray enclosure, Eqs. (1-2) through (1-4) reduce to

$$q_i = \varepsilon_i \sum_{j=1}^n \sigma T_j^4 (\delta_{ij} - D_{ij}), \quad 1 \leq i \leq n, \quad (3-2)$$

where

$$\delta_{ij} \equiv \begin{cases} 1, & i = j \\ 0, & i \neq j \end{cases}. \quad (3-3)$$

In Eq. (3-2), ε_i is the emissivity of surface element i . Equation (3-2) may be thought of as an approximation because Eq. (3-1) produces an estimate of D_{ij} , the accuracy of which increases with the number of rays traced for a given number of surface elements n . Concerns expressed elsewhere [18] about the perceived need to

“smooth” the exchange or distribution factor matrix are unwarranted when its elements are estimated using the MCRT method. The use of Eq. (3-1) to compute D_{ij} ensures that both conservation of energy and reciprocity are satisfied to a high degree of accuracy.

In contrast to the net-exchange method, if the surface temperature distribution is known, the surface net heat flux distribution can be computed directly from the distribution factors. When the surface net heat fluxes q_i are specified and the surface temperatures T_i are unknown, a rearranged version of Eq. (3-2) is invoked [3]. Similarly, a version of Eq. (3-2) is also available for the case where the net heat fluxes are specified for some of the surface elements and the temperatures are specified for the remaining elements. In this chapter we consider only the case of specified surface temperatures. However, we indicate at the appropriate juncture in the theoretical development how these alternative situations can be accommodated.

3.2. Importance of establishing the accuracy of the MCRT method

The uncertainties associated with the heat transfer results obtained using the MCRT method depend in some way on the uncertainties in the specified temperatures, the surface models for absorptivity, emissivity and reflectivity, and the distribution factors. The goal of this chapter is to establish a statistically rigorous formalism for quantifying the uncertainty in heat transfer results associated with these component uncertainties.

The seminal contribution dealing with uncertainties in thermal radiative analysis was evidently by J. R. Howell in 1973 [69]. Howell solved the same 18-node combined conduction-radiation model 50 times, each time using a different set of emissivities, thermal conductivities, and geometries perturbed about their nominal values. While Howell’s radiant exchange model was based on the net-exchange formulation (i.e., using view, or configuration, factors) rather than on the MCRT

method, he did use Monte Carlo principles to randomly distribute the dimensions and material properties about their mean (nominal) values with a specified standard deviation.

Nearly two decades passed before investigators began turning their attention to uncertainty in ray-trace-based methods of thermal radiative modeling. In a transitional 1993 paper, Planas Almazan [70] quantified the statistical errors inherent to a hybrid net-exchange formulation in which the (purely geometrical) configuration factors were estimated using a Monte Carlo ray-trace. Whereas Howell considered contributions to overall model uncertainty attributable to uncertainty in emissivity, thermal conductivity, and geometry, Planas Almazan considered only the contribution to overall model uncertainty due to uncertainty in the configuration factors.

In two closely related papers published in 1993 [71] and 1995 [72], Taylor et al. consider the uncertainty propagated in the net-exchange (“radiosity-irradiance”) formulation due to uncertainties in the view factors, emissivities, surface areas, and boundary conditions. Whereas Howell assesses the *a posteriori* propagated uncertainty of heat transfer results based on repeated solutions of normally perturbed versions of the same problem, Taylor et al. derive explicit relationships, ultimately based on the formalism of Kline and McClintock [73], for assigning the expected uncertainty in heat transfer results based on the known uncertainties in the view factors, emissivities, surface areas, and boundary conditions. In contrast to Planas Almazan [70], whose estimates of uncertainty for the view factors are based on the statistical principles governing Monte Carlo ray-tracing, Taylor et al. simply assign uncertainties to the view factors.

A 1997 paper by Planas Almazan [74] seems to be the first to consider uncertainty in the MCRT method as used elsewhere in this dissertation. The main contribution of this example-based paper is its early demonstration of the now well-appreciated convergence of the distribution factors with the number of rays traced.

Several significant contributions to the understanding of uncertainty in the MCRT method may be found in a series of papers [75-77] and a textbook chapter [2] stemming from M. C. Sanchez's 2002 doctoral research effort [78]. In a 1999 paper, Sanchez et al. [75] introduce the now widely accepted interpretation of the radiation distribution factor as a population proportion whose uncertainty ω_D , to a stated level of confidence, is related to its estimated value D_{ij}^e and to the number of rays traced per surface element N_i according to

$$\omega_{D_{ij}} = \pm W_c \sqrt{\frac{D_{ij}^e(1 - D_{ij}^e)}{N_i}}, \quad (3 - 4)$$

where W_c is the critical value of a tabulated statistic whose value depends on the level of confidence. For example, for a 95-percent confidence interval, $W_c = 1.960$. In another paper, Sanchez et al. [78] extend the result given in Eq. (3-4) to allow prediction of the mean relative uncertainty, averaged over all of the distribution factors, for an enclosure consisting of n surfaces,

$$\left\langle \left\langle \frac{\omega_{D_{ij}^e}}{D_{ij}^e} \right\rangle_j \right\rangle_i \equiv \frac{\omega_D}{D} \approx \pm W_c \sqrt{\frac{n - 1}{N}}. \quad (3 - 5)$$

The right-hand element of Eq. (3-5) has been obtained by replacing D_{ij}^e in Eq. (3-4) with its mean value, $\langle\langle D_{ij}^e \rangle\rangle = 1/n$. The significance of this result is that, to within the accuracy of the approximation implied by the right-hand side of Eq. (3-5), it can be used as a predictor of the global mean relative uncertainty of the distribution factors without actually performing a ray-trace. In other words, within certain limits established here, it holds for all n -surface enclosures regardless of dimensionality and their actual geometry. A useful table based on this expression for the case of a 95-percent confidence interval may be found elsewhere [2, 3, 77].

Finally, in yet another contribution by Sanchez et al. [76] results from four numerical experiments are reported, each using a different random number sequence, which demonstrate that Eq. (3-5) with $W_c = 1.960$ represents an upper bound on the mean relative uncertainty of the distribution factors for a specific nine-surface diffuse-specular enclosure. Furthermore, the results suggest that the actual uncertainties approach the values predicted by Eq. (3-5) as the number of rays traced is increased.

An important goal and major accomplishment of the current effort is establishment of the accuracy and limits of applicability of Eq. (3-5) and, ultimately, its replacement with a more accurate expression. Two problems representing demonstrably different types of enclosure—one with and one without an internal obstruction—are solved 50 times each with surface temperatures and emissivities randomly (normally) perturbed about mean values. The observed uncertainties in distribution factors and net heat fluxes are then compared with values predicted from the theory developed here. This approach leads to an improved version of Eq. (3-5) and to validation of a new expression for the uncertainty in net heat flux.

3.3. Uncertainty formulation

3.3.1. Uncertainty in the distribution factors

If a population is randomly sampled for proportion and the sample size is sufficiently large, the statistical distribution of the sample proportion p will be normal even though the underlying distribution is binomial [2, 3]. This means that hypothesis testing for proportion can be accomplished using essentially the same statistical tools as used in the case of the population mean. The only difference is that now our estimate of the sample standard deviation is based on the standard deviation of a binomial distribution; that is,

$$s = \frac{\sigma}{N}, \tag{3 - 6}$$

where s is the estimate of the sample standard deviation, σ is the standard deviation of a binomial distribution and N is the number of observations. The standard deviation for a binomial distribution may be approximated by

$$\sigma \equiv \sqrt{N\pi(1-\pi)} \approx \sqrt{Np(1-p)}, \quad (3-7)$$

where π is the true population proportion and p is its estimate. Consequently,

$$s \approx \sqrt{\frac{p(1-p)}{N}}. \quad (3-8)$$

The equivalent of the Student's t statistic in establishing population proportion confidence intervals is the W statistic,

$$W \equiv \frac{p - \pi}{\sqrt{p(1-p)/N}}, \quad (3-9)$$

where the probability distribution of W is approximately normal. Then, the confidence interval for the population proportion π is

$$p - W_c \sqrt{\frac{p(1-p)}{N}} \leq \pi \leq p + W_c \sqrt{\frac{p(1-p)}{N}}, \quad (3-10)$$

where the critical value of W , W_c , as a function of confidence interval is tabulated in standard texts as a function of N and the desired confidence interval.

The true value of the distribution factor D_{ij}^t is a population proportion π and $p = D_{ij}^e$ is its estimate [2, 3]. Therefore, we can write

$$1 - W_c \sqrt{\frac{1 - D_{ij}^e}{ND_{ij}^e}} \leq \frac{D_{ij}^t}{D_{ij}^e} \leq 1 + W_c \sqrt{\frac{1 - D_{ij}^e}{ND_{ij}^e}}, \quad (3-11)$$

where the MCRT-based estimate D_{ij}^e is obtained by tracing N energy bundles. From Eq. (3-11), we recognize that the uncertainty in the distribution factors is related to their estimated values and to the related confidence interval according to

$$\frac{\omega_{D_{ij}}}{D_{ij}} = \pm W_c \sqrt{\frac{1 - D_{ij}^e}{ND_{ij}^e}}. \quad (3 - 12)$$

Note that Eq. (3-12) is simply a rearrangement of Eq. (3-4). In a practical ray-trace, it is possible that D_{ij}^e will be zero to within the accuracy of the processor being used, resulting in an indefinite value for its relative uncertainty. This issue arises during the solution of Example Problem 2 in Section 3-3, where we avoid using values of D_{ij}^e less than 5×10^{-5} . This issue also appears in Chapter 6, Fig. 6.4, where we see that relative errors associated with the prediction of the very small values of the radiation distribution factors are relatively high.

Equation (3-12), which applies for a particular distribution factor between two specified surface elements i and j , leads directly to the approximation embodied in Eq. (3-5) when the left-hand side is averaged over i and j and D_{ij}^e is replaced with the mean value of all distribution factors, $\langle\langle D_{ij} \rangle\rangle = 1/n$. Note that this general result is independent of any specific enclosure geometry including its dimensionality. The degree of approximation implied by Eq. (3-5) is investigated in Section 3-3.

3.3.2. Uncertainty in heat transfer results

Consider the case in which surface temperatures are specified with stated uncertainties. Then the net surface radiative heat fluxes are

$$q_i = q_{i,e} - q_{i,a}, \quad 1 \leq i \leq n, \quad (3 - 13)$$

where

$$q_{i,e} = \varepsilon_i \sigma T_i^4 \quad (3 - 14)$$

and

$$q_{i,a} = \varepsilon_i \sum_{j=1}^n \sigma T_j^4 D_{ij}. \quad (3-15)$$

Note that Eqs. (3-13) through (3-15) taken together are equivalent to Eqs. (3-2) and (3-3).

Following the widely accepted formalism of Kline and McClintock [73],

$$\omega_{q_i} = \pm \sqrt{\left(\frac{\partial q_i}{\partial q_{i,e}} \omega_{q_{i,e}}\right)^2 + \left(\frac{\partial q_i}{\partial q_{i,a}} \omega_{q_{i,a}}\right)^2}, \quad (3-16)$$

where

$$\omega_{q_{i,e}} = \pm \sqrt{\left(\frac{\partial q_{i,e}}{\partial \varepsilon_i} \omega_{\varepsilon_i}\right)^2 + \left(\frac{\partial q_{i,e}}{\partial T_i} \omega_{T_i}\right)^2} \quad (3-17)$$

and

$$\omega_{q_{i,a}} = \pm \sqrt{\left(\frac{\partial q_{i,a}}{\partial \varepsilon_i} \omega_{\varepsilon_i}\right)^2 + \left(\frac{\partial q_{i,a}}{\partial T_j} \omega_{T_j}\right)^2 + \left(\frac{\partial q_{i,a}}{\partial D_{ij}} \omega_{D_{ij}}\right)^2}. \quad (3-18)$$

Introducing the appropriate expressions for the sensitivities, we obtain

$$\omega_{q_i} = \pm \left\{ \begin{array}{l} \left((\sigma T_i^4 \omega_{\varepsilon_i})^2 + (4\varepsilon_i \sigma T_i^3 \omega_{T_i})^2 + \left(\omega_{\varepsilon_i} \sum_{j=1}^n \sigma T_j^4 D_{ij} \right)^2 \right)^{\frac{1}{2}} \\ + \left(4\varepsilon_i \sum_{j=1}^n \sigma T_j^3 \omega_{T_j} D_{ij} \right)^2 + \left(\varepsilon_i \sum_{j=1}^n \sigma T_j^4 \omega_{D_{ij}} \right)^2 \end{array} \right\}, \quad 1 \leq i \leq n. \quad (3-19)$$

Note that if the surface net heat fluxes are specified rather than the surface temperatures, Eq. (3-19) can be solved directly for the uncertainty in the unknown

surface temperatures. In this case appropriate changes would have to be made in the following development, but they are straightforward and obvious. Less obvious but still possible would be application of this material to the case where temperatures are specified for some surface elements and net heat fluxes are specified for the remaining surface elements.

Dividing Eq. (3-19) through by the heat flux emitted by surface element i yields

$$\frac{\omega_{q_i}}{\varepsilon_i \sigma T_i^4} = \pm \left\{ \left(\frac{\omega_{\varepsilon_i}}{\varepsilon_i} \right)^2 + \left(4 \frac{\omega_{T_i}}{T_i} \right)^2 + \left[\frac{\omega_{\varepsilon_i}}{\varepsilon_i} \sum_{j=1}^n \left(\frac{T_j}{T_i} \right)^4 D_{ij} \right]^2 \right\}^{\frac{1}{2}} \\ + \left[4 \sum_{j=1}^n \left(\frac{T_j}{T_i} \right)^4 \frac{\omega_{T_j}}{T_j} D_{ij} \right]^2 + \left[\sum_{j=1}^n \left(\frac{T_j}{T_i} \right)^4 \omega_{D_{ij}} \right]^2 \quad (3-20)$$

$1 \leq i \leq n.$

Equation (3-20) expresses the uncertainty in the net heat flux from surface element i as a fraction of the known flux emitted by that surface element. Up to this point no assumptions have been made that limit the applicability of this result; that is, it holds for any n -surface diffuse gray enclosure regardless of its dimensionality.¹

We now seek an expression for the global mean of the relative net heat flux; that is, the mean averaged over all n of the surface elements. The first step in this direction is to replace the local fractional uncertainties in emissivity, temperature,

¹ Strictly speaking, since D_{ij} depends on ε_i through the ray-trace, Eq. (3-18) violates the Kline and McClintock formalism. This formalism requires that the parameters determining the results must be independent of each other. If not true, then an analytical expression for the interdependence must be available. However, no such expression exists for $D_{ij} = f(\varepsilon_i)$. Treatment of D_{ij} and ε_i as independent parameters is then an expediency that limits the validity of Eq. (3-19) in an unknown manner. The effects of this limit and the usability of Eq. (3-19) is discussed later in this chapter.

and distribution factor in Eq. (3-20) with appropriate global mean values. Recognizing that in a typical situation the emissivities and temperatures for all of the surfaces will presumably have been evaluated using the same instruments and procedures, the global mean values are those associated with the accuracy of these measurements; i.e.,

$$\frac{\omega_{\varepsilon_i}}{\varepsilon_i} = \frac{\omega_{\varepsilon}}{\varepsilon}, \quad (3-21)$$

and

$$\frac{\omega_{T_i}}{T_i} = \frac{\omega_T}{T}. \quad (3-22)$$

The local fractional uncertainty in the distribution factors is replaced with the global mean value obtained using Eq. (3-5); i.e.,

$$\frac{\omega_{D_{ij}}}{D_{ij}} = \frac{\omega_D}{D}. \quad (3-23)$$

Equation (3-20) then becomes

$$\begin{aligned} & \frac{\omega_{q_i}}{\varepsilon_i \sigma T_i^4} \\ &= \pm \sqrt{\left[\left(\frac{\omega_{\varepsilon}}{\varepsilon} \right)^2 + \left(4 \frac{\omega_T}{T} \right)^2 \right] \left[1 + \left(\sum_{j=1}^n \left(\frac{T_j}{T_i} \right)^4 D_{ij} \right)^2 \right] + \left(\frac{\omega_D}{D} \right)^2 \left[\sum_{j=1}^n \left(\frac{T_j}{T_i} \right)^4 D_{ij} \right]^2}, \\ & 1 \leq i \leq n. \end{aligned} \quad (3-24)$$

Two approximations are now invoked whose impact on accuracy is eventually evaluated and justified by numerical experiments carried out in Section 3.3: (1) we replace D_{ij} with its mean value, $1/n$; and (2) we replace $\sum_{j=1}^n \left(\frac{T_j}{T_i} \right)^4 D_{ij}$ with the

mean value over j of $\left(\frac{T_j}{T_i}\right)^4$, $\left\langle\left(\frac{T_j}{T_i}\right)^4\right\rangle_j$. This is justified because $\sum_{j=1}^n D_{ij} = 1/n$.

There results

$$\frac{\omega_{q_i}}{\varepsilon_i \sigma T_i^4} \approx \pm \sqrt{\left[\left(\frac{\omega_\varepsilon}{\varepsilon}\right)^2 + \left(4\frac{\omega_T}{T}\right)^2\right] \left[1 + \left(\left\langle\left(\frac{T_j}{T_i}\right)^4\right\rangle_j\right)^2\right] + \left(\frac{\omega_D}{D}\right)^2 \left(\left\langle\left(\frac{T_j}{T_i}\right)^4\right\rangle_j\right)^2}$$

$$1 \leq i \leq n, \quad (3-25)$$

Finally, a further approximation is invoked by replacing $\frac{\omega_{q_i}}{\varepsilon_i \sigma T_i^4}$ and $\left\langle\left(\frac{T_j}{T_i}\right)^4\right\rangle_j$ by their mean values over i , thereby obtaining

$$\left\langle\frac{\omega_{q_i}}{\varepsilon_i \sigma T_i^4}\right\rangle$$

$$\approx \pm \sqrt{\left[\left(\frac{\omega_\varepsilon}{\varepsilon}\right)^2 + \left(4\frac{\omega_T}{T}\right)^2\right] \left[1 + \left(\left\langle\left\langle\left(\frac{T_j}{T_i}\right)^4\right\rangle_j\right\rangle\right)^2\right] + \left(\frac{\omega_D}{D}\right)^2 \left(\left\langle\left\langle\left(\frac{T_j}{T_i}\right)^4\right\rangle_j\right\rangle\right)^2},$$

$$(3-26)$$

where $\left\langle\left\langle\left(\frac{T_j}{T_i}\right)^4\right\rangle_j\right\rangle$ is the mean fourth-power temperature spread,

$$\left\langle\left\langle\left(\frac{T_j}{T_i}\right)^4\right\rangle_j\right\rangle = \left\langle\left\langle\left(\frac{T_j}{T_i}\right)^4\right\rangle_j\right\rangle_i \equiv \frac{1}{n^2} \sum_{i=1}^n \sum_{j=1}^n \left(\frac{T_j}{T_i}\right)^4. \quad (3-27)$$

Note that Eq. (3-24) is exact while Eq. (3-26) is an approximation whose accuracy remains to be established. We explore the degree of this approximation through examples in Section 3.3. The advantage of Eq. (3-26) over Eq. (3-24) is that Eq. (3-26) allows prediction of the mean relative uncertainty in net heat flux based on the

surface temperature distribution, independent of the enclosure geometry and without first computing the distribution factors.

3.4. Validation of the uncertainty formulation

We validate the foregoing formulation for the relative uncertainties in distribution factor and net heat flux through numerical experiments. In both example problems one million rays are traced per surface element.

3.4.1. Example Problem 1

In Example Problem 1, we consider the net heat flux distribution from each surface of a cubic enclosure consisting of three surfaces having a uniform temperature of 300 K and three surfaces having a uniform temperature of 500 K. Figure 3.1 shows the geometry of the problem. The cubic enclosure is subdivided into 384 equal-area surface elements, and 1 million rays are traced from each surface element. The surfaces are considered to be diffuse and gray, with a nominal emissivity of 0.55.

The contributions to overall uncertainty due to the uncertainties in temperature and surface emissivity are sampled by executing the numerical experiment $M = 50$ times with random perturbations applied to temperature and surface emissivity in each case. Two successive normally distributed perturbed values of any quantity δ ($= \varepsilon$ or T here) are related to the sample mean value m and the sample standard deviation s by [79]

$$\delta = m + s\sqrt{2 \ln(1/R_1)} \cos(2\pi R_2) \quad (3 - 28)$$

and

$$\delta = m + s\sqrt{2 \ln(1/R_1)} \sin(2\pi R_2). \quad (3 - 29)$$

In Eqs. (3-28) and (3-29), R_1 and R_2 are two random numbers whose values are uniformly distributed between zero and unity. According to the definition of the t

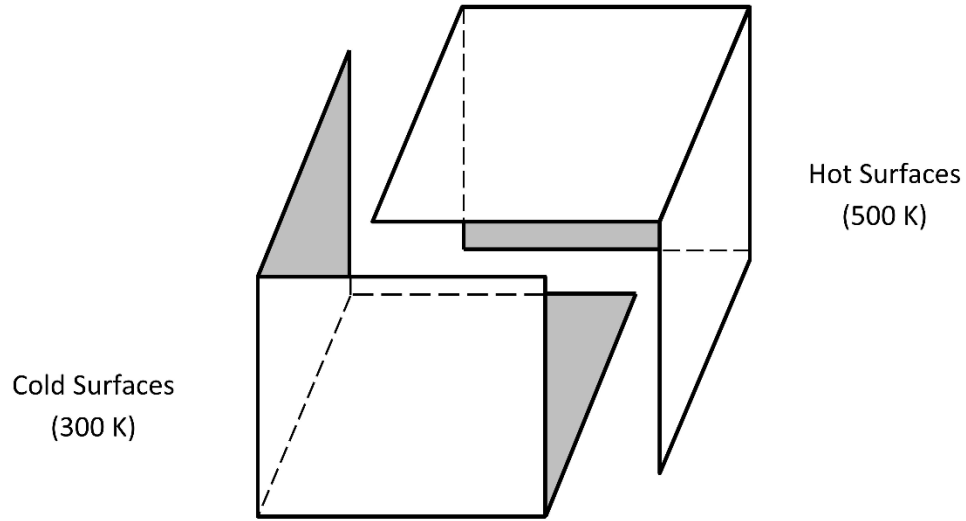


Figure 3.1. Exploded view of the cubic enclosure for Example Problem 1. The three interior surfaces comprising the upper-right section are maintained at 500 K (hot surfaces), and the three interior surfaces comprising the lower-left section are maintained at 300 K.

statistic, the sample standard deviation s is related to the uncertainty $\omega = \pm|m - \mu|$ by

$$s = \frac{\omega}{t/\sqrt{M}}, \quad (3 - 30)$$

where μ is the (unknown) true mean value of δ and M is the number of numerical experiments. For the purposes of this study a relative uncertainty ω_δ/δ of one percent is assumed for both emissivity and temperature. Figure 3.2 shows the heat flux distribution for the cold and hot surfaces when averaged over 50 experiments and, because of symmetry, further averaged over the three surfaces in each case. The number of surface elements used, 384, represents a compromise between, on the one hand, achieving adequate spatial resolution and, on the other hand, limiting the computer resources required to compute the $384^2 = 147,456$ distribution factors.

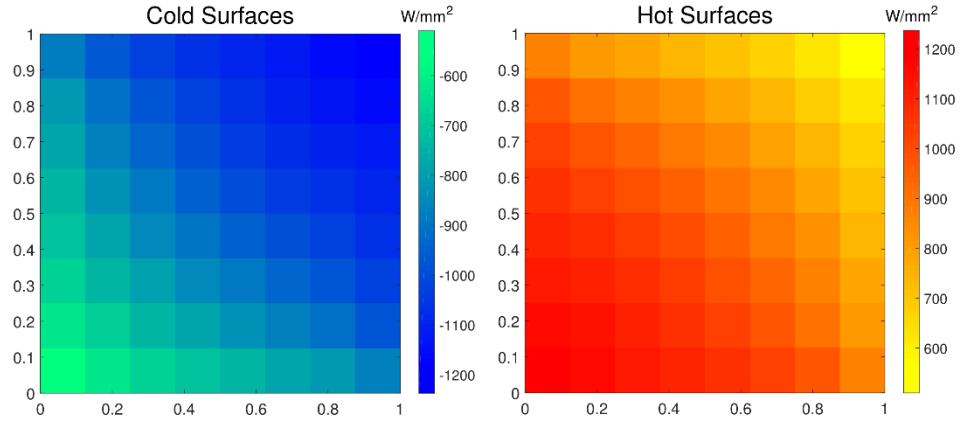


Figure 3.2. Average net heat flux distribution for the cold and hot surfaces for Example Problem 1.

3.4.1.1. Validation of the distribution factor mean uncertainty relation for Example Problem 1

Figure 3.3 compares, for each of the 50 experiments, the observed values of the mean relative uncertainty, obtained by averaging Eq. (3-12) over i and j (solid symbols), with the value of mean relative uncertainty in the distribution factors predicted by Eq. (3-5) (continuous line). When the observed values of the mean relative uncertainty are averaged over the 50 experiments and expressed as a percentage, a value of 4.48 is obtained, while Eq. (3-5) predicts 3.83 percent for this same value.

An alternative view of uncertainty of the distribution factors is the *relative error* in the distribution factor estimate suggested by Sanchez [78],

$$RE_{ij} \equiv \frac{|D_{ij}^e - D_{ij}^t|}{D_{ij}^t}. \quad (3 - 31)$$

In Eq. (3-31), D_{ij}^e is the value of the radiation distribution factor from i to j as estimated using the MCRT method, and D_{ij}^t is its unknown true value. This latter quantity may be approximated as the mean value of the distribution factors obtained from the M experiments, assuming M is sufficiently large; i.e.,

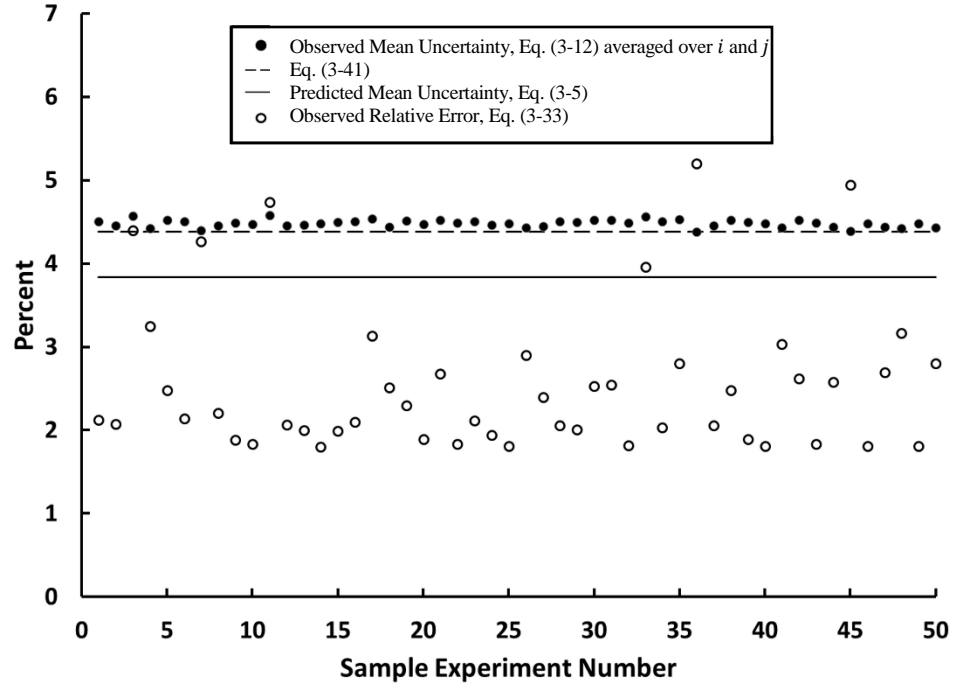


Figure 3.3. Comparison for each of the 50 experiments of the observed mean uncertainty (filled symbols) and the observed relative error (open symbols) with the predicted mean uncertainty in the distribution factors (continuous line) for Example Problem 1.

$$D_{ij}^t \approx \frac{1}{M} \sum_{p=1}^M D_{ij}^e. \quad (3 - 32)$$

The mean relative error in the distribution factors for a given experiment may then be defined

$$\langle\langle RE \rangle\rangle \equiv \left\langle \left\langle \frac{|D_{ij}^e - D_{ij}^t|}{D_{ij}^t} \right\rangle_j \right\rangle_i = \frac{1}{n^2} \sum_{i=1}^n \sum_{j=1}^n \frac{|D_{ij}^e - D_{ij}^t|}{D_{ij}^t}. \quad (3 - 33)$$

The observed values of the mean relative error, Eq. (3-33), plotted as open symbols in Fig. 3.3, are also in good agreement with and are generally bounded by the Eq. (3-5) prediction.

Even though agreement among the quantities plotted in Fig. 3.3 is adequate for the stated goal of using Eq. (3-5) as an *a priori* estimate of expected relative uncertainty of the distribution factors, it is still appropriate to consider sources for the differences in these three quantities. First, note that D_{ij}^e appears in the denominator of the right-hand side of the expression for $\omega_{D_{ij}}/D_{ij}$, Eq. (3-12), while D_{ij}^t appears in denominator of the expression for the relative error, Eq. (3-31). This suggests that better agreement between the relative uncertainty and the relative error might be obtained by replacing D_{ij}^t with D_{ij}^e in the denominator of Eq. (3-31). However, in practice this replacement is found to have very little effect due to the small differences between D_{ij}^t and D_{ij}^e . Also, note that Eq. (3-5) is obtained by averaging the left-hand side of Eq. (3-12) over i and j while replacing D_{ij}^e by its mean value $1/n$ on the right-hand side. This is contrary to the procedure used in deriving Eq. (3-33), in which both sides of Eq. (3-31) are formally averaged over i and j . We return to this question after consideration of Example Problem 2.

3.4.1.2. Validation of the net heat flux uncertainty predictor for Example Problem 1

The standard deviation of the net heat flux from surface i , s_i , for M independent experiments is

$$s_i = \sqrt{\frac{1}{M-1} \sum_{p=1}^M (q_i^p - q_i^m)^2}, \quad (3-34)$$

where q_i^p is the net heat flux for a given experiment and q_i^m is the mean value of the M net heat fluxes obtained; i.e.,

$$q_i^m = \frac{1}{M} \sum_{p=1}^M q_i^p. \quad (3-35)$$

Then we can state that the true value of the net heat flux lies in the interval

$$q_i^m - t_c \frac{s_i}{\sqrt{M}} \leq q_i^t \leq q_i^m + t_c \frac{s_i}{\sqrt{M}}, \quad (3 - 36)$$

where t_c is the critical value of student's t statistic as a function of M and the confidence interval. Therefore, we obtain for the uncertainty in net heat flux

$$\omega_{q_i} = \pm t_c s_i / \sqrt{M}, \quad (3 - 37)$$

and for the mean value of uncertainty of net heat flux we have

$$\langle \omega_{q_i} \rangle = t_c \langle s_i / \sqrt{M} \rangle. \quad (3 - 38)$$

An expression for the observed mean relative net heat flux can be obtained by dividing Eq. (3-37) by $\varepsilon_i \sigma T_i^4$ before averaging over the n surfaces of this enclosure. When this is done and the result applied to the case of $M = 50$ experiments, an observed mean relative net heat flux uncertainty of 16.95 percent is obtained with a confidence interval of 95 percent ($t_c = 1.960$). Alternatively, an observed mean relative uncertainty of 15.7 percent may be obtained for this case by averaging Eq. (3-24) over the $n = 384$ surface elements and the $M = 50$ experiments, with Eq. (3-5) used to estimate the relative uncertainty of the distribution factors and with $\frac{\omega_\varepsilon}{\varepsilon} = \frac{\omega_T}{T} = 0.01$. These two observed values compare favorably with each other and with the value, 14.46, predicted using Eq. (3-26) with a mean fourth-power temperature spread of 2.4614 and using Eq. (3-5) to estimate the relative mean uncertainty in the distribution factors. We conclude that, for Example Problem 1, the overall uncertainty in mean relative net heat flux predicted before running the ray-trace (14.46 percent) is in acceptable agreement with the observed overall uncertainties of 16.95 percent and 15.7 percent obtained after running the ray-trace. Equation (3-26) is recommended for affixing error bars to net heat flux results computed for individual surface elements.

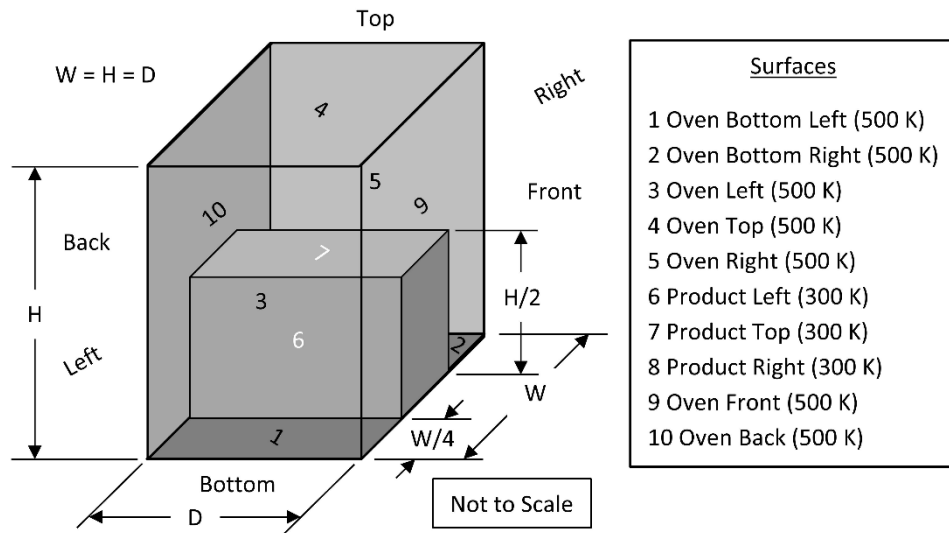


Figure 3.4. Isometric view of oven in Example Problem 2.

3.4.2. Example Problem 2

Example Problem 2 considers an evacuated cubic oven, already considered in Chapter 2, intended for heating a rectangular solid product positioned on its floor, as shown in Fig. 3.4. Example Problem 2 is more stringent than Example Problem 1 for validating the proposed method for predicting uncertainty in the distribution factors and the net heat flux distribution, because radiant exchange between some of the surfaces is indirect, i.e., is due to reflection only. This results in greater variability in both the distribution factors and net heat fluxes. The Example Problem 2 enclosure is subdivided into 416 equal-area surface elements, and 1 million rays are traced from each surface element. All surfaces are once again diffuse and gray with a nominal emissivity of 0.55. As in the case of Example Problem 1, 50 numerical experiments were executed with randomly perturbed uncertainties in temperature and surface emissivity based on Eqs. (3-28) and (3-

29). Figure 3.5 shows the heat flux distribution when averaged over 50 experiments.

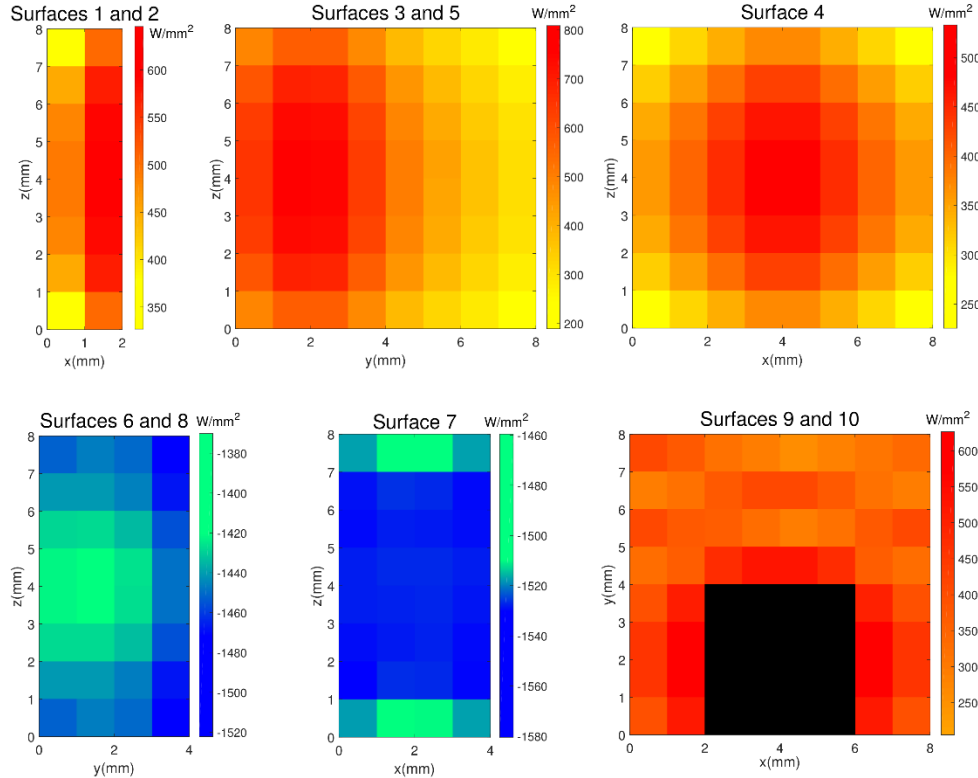


Figure 3.5. Net heat flux distributions for the oven and product surfaces for Example Problem 2.

3.4.2.1. Validation of the distribution factor mean uncertainty relation for Example Problem 2

Figure 3.6 compares, for each of the 50 experiments, the observed values of the mean relative uncertainty, obtained by averaging Eq. (3-12) over i and j (solid symbols), the observed values of the mean relative error, Eq. (3-33) (open symbols), and the value of mean relative uncertainty in the distribution factors predicted by Eq. (3-5) (continuous line). When the observed values of the mean relative uncertainty (solid symbols) are averaged over the 50 experiments and expressed as a percentage, a value of 5.746 is obtained, while Eq. (3-5) predicts 3.99 percent for this same value. Comparison of Figs. 3.3 and 3.6 suggests that the mean

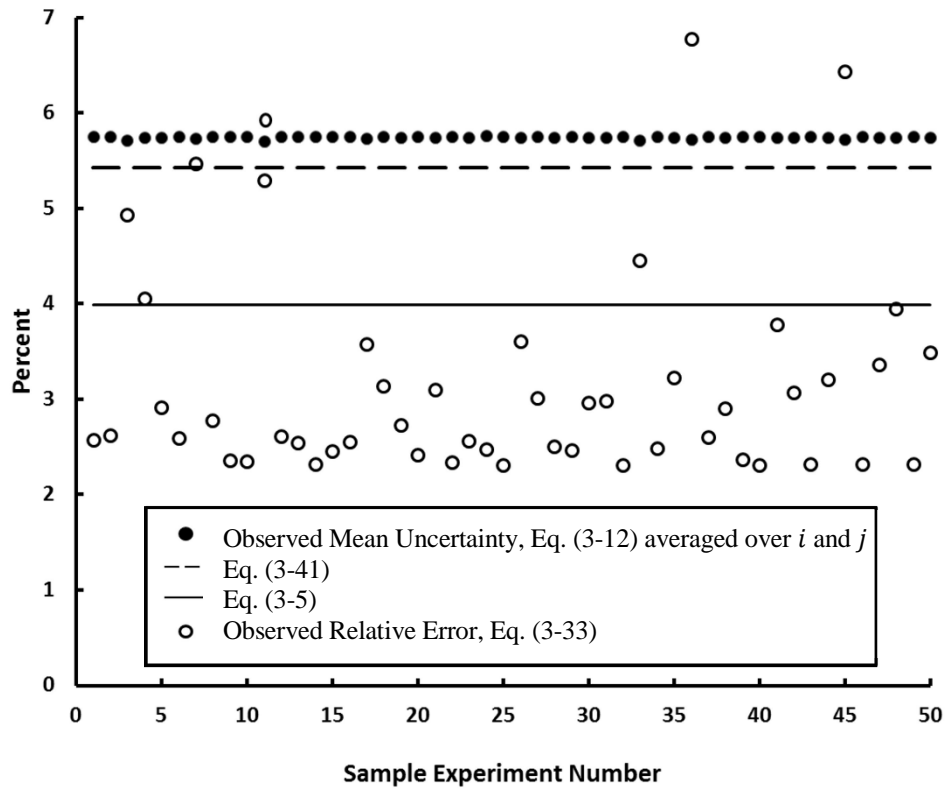


Figure 3.6. Comparison for each of the 50 experiments of the observed mean uncertainty (filled symbols) and the observed relative error (open symbols) with the predicted mean uncertainty in the distribution factors (continuous line) for Example Problem 2.

distribution factor uncertainty predicted using Eq. (3-5) and the observed average of Eq. (3-12) over i and j agree less well for Example Problem 2 than for Example Problem 1.

3.4.2.2. Validation of the net heat flux uncertainty predictor for Example Problem 2

As in the case of Example Problem 1, an expression for the observed mean relative net heat flux can be obtained by dividing Eq. (3-37) by $\epsilon_i \sigma T_i^4$ before averaging over the n surfaces of the enclosure. When this is done and the result used to compute the observed mean relative net heat flux uncertainty, a value of 13.47

percent is obtained. When this same uncertainty is computed by averaging Eq. (3-24) over the $n = 416$ surface elements and the $M = 50$ experiments, with Eq. (3-5) used to estimate the relative uncertainty of the distribution factors, a nearly identical value of 13.75 percent is obtained. The observed value of mean uncertainty in the relative net heat flux agrees well with the value—12.40 percent—predicted using Eq. (3-26) with Eq. (3-5) and a mean fourth-power temperature spread of 2.0377. Thus, Example Problem 2 reinforces the conclusions that the overall uncertainty in mean relative net heat flux predicted by Eq. (3-26) before running the ray-trace is in acceptable agreement with the observed overall uncertainty obtained after running the ray-trace. Furthermore, Example Problem 2 confirms the conclusion, based on Example Problem 1, that Eq. (3-26) is appropriate for affixing error bars to net heat flux results computed for individual surface elements.

3.4.3. Discussion of the distribution factor mean uncertainty results

The difference between the observed and predicted values of the mean relative uncertainty in the distribution factors can be best understood with reference to the histogram of the radiation distribution factors themselves, shown in Fig. 3.7. Even though some distribution factors exceed a value of 0.01 in both example problems, the horizontal axes in Fig. 3.7 have been truncated at this value to better reveal the shape of the histogram, near the mean. It is clear that the distribution factor histograms are radically different in the two problems. For example, The histogram, corresponding to Example Problem 1, shown in Fig. 3.7(a), exhibits no near-zero values while the histogram corresponding to Example Problem 2, shown in Fig. 3.7(b), exhibits many. The reason for this, of course, is that in Example Problem 1 every surface element has a direct view of every other surface element, whereas this is far from true in Example Problem 2, where many surfaces exchange heat only by reflection.

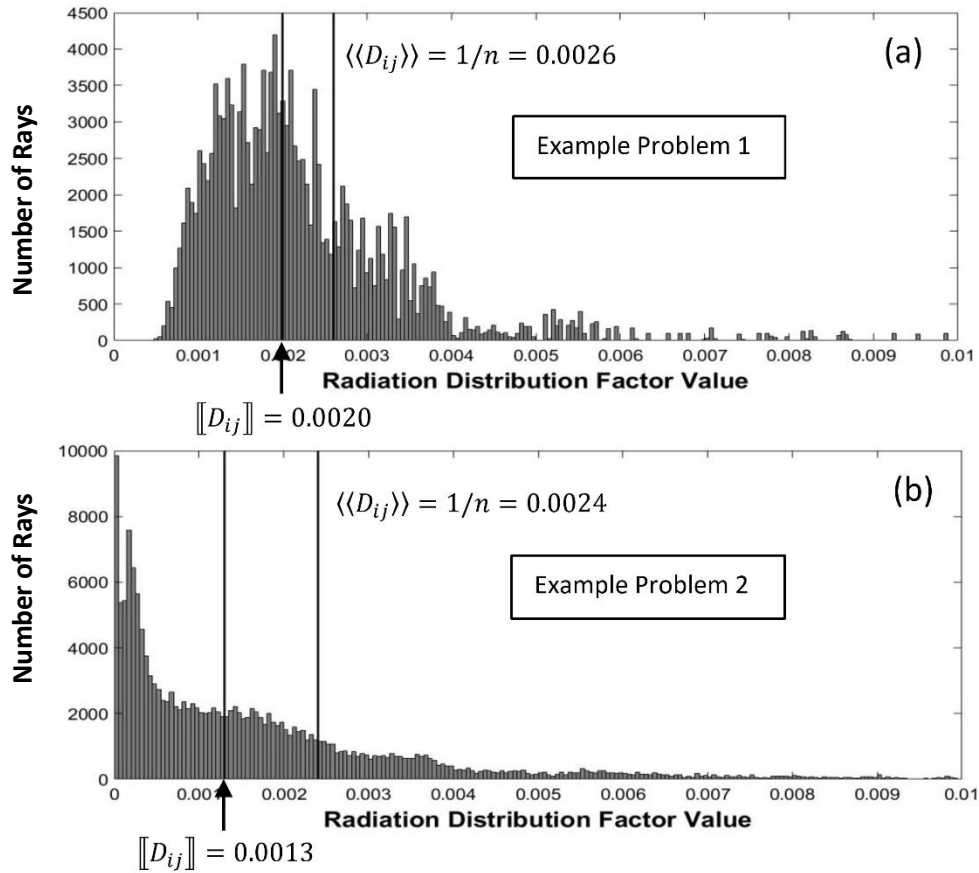


Figure 3.7. Histograms for radiation distribution factors in (a) Example Problem 1 and (b) Example Problem 2.

We note that the histograms for both example problems are biased in favor of smaller values of the distribution factors; that is, a disproportionate number of distribution factors have values less than the mean value $1/n$. The role of n in Eq. (3-5) is based on the assumption of equal influence on overall uncertainty by distribution factors lying above and below the mean. However, this is generally not the case for two reasons: (1) the majority of the distribution factors have values less than the mean, and (2) Eq. (3-12) clearly shows that the relative uncertainty in the value of a particular distribution factor increases as the value itself decreases for a given number of rays traced. These two factors lead us to expect that the observed mean relative uncertainty of the distribution factors will generally exceed the value

predicted by Eq. (3-5). This expectation is realized in Figs. 3.3 and 3.6, which show that Eq. (3-5) (continuous line) indeed underestimates the observed values of the mean relative uncertainty (solid symbols).

In principle the role of Eq. (3-5) as a predictor of the mean relative uncertainty of the distribution factors could be improved by replacing the global mean value of the distribution factors $\langle\langle D_{ij}^e \rangle\rangle = 1/n$ with a suitably weighted mean of the distribution factors $\llbracket D_{ij}^e \rrbracket$ that takes into account both the greater number of distribution factors whose values are less than $1/n$ and the larger uncertainty associated with smaller distribution factors. We can address the imbalance of the number of distribution factors lying above and below the mean value by equating $\llbracket D_{ij}^e \rrbracket$ to the value of D_{ij}^e for which the *cumulative distribution factor* (CDF) is equal to one-half; i.e.,

$$CDF(\llbracket D_{ij}^e \rrbracket) \equiv \int_0^{\llbracket D_{ij}^e \rrbracket} PDF(D_{ij}^e) dD_{ij}^e / \int_0^1 PDF(D_{ij}^e) dD_{ij}^e = \frac{1}{2}. \quad (3-39)$$

That is, after ranking the n^2 distribution factors from smallest to largest, the resulting histogram is then integrated up to the value of D_{ij}^e corresponding to one-half of the value corresponding to $CDF(\llbracket D_{ij}^e \rrbracket) = 1$. The value of $\llbracket D_{ij}^e \rrbracket$ defined by Eq. (3-39) is referred to as the *median* of the histogram. Eq. (3-39) can be well approximated by,

$$CDF(\llbracket D_{ij}^e \rrbracket) \cong \frac{1}{n^2} \sum_0^{\llbracket D_{ij}^e \rrbracket} PDF(\overline{D}_{ij}^e), \quad (3-40)$$

where the summation is over the count of distribution factors in the bars in Fig. 3.7, \overline{D}_{ij}^e is the mean value of the distribution factors in a given bar, and n is the number of surfaces making up the enclosure. Equation (3-40) is implicit in $\llbracket D_{ij}^e \rrbracket$ and therefore must be summed until a value of $1/2$ is obtained. When this is done

for Example Problem 1, $\llbracket D_{ij}^e \rrbracket_1 = 0.0020$, while for Example Problem 2, $\llbracket D_{ij}^e \rrbracket_2 = 0.0013$. These values are indicated in Fig. 3.7. When D_{ij}^e is replaced with $\llbracket D_{ij}^e \rrbracket$ in Eq. (3-12) we have

$$\frac{\omega_D}{D} \approx \pm W_c \sqrt{\frac{1 - \llbracket D_{ij}^e \rrbracket}{N \llbracket D_{ij}^e \rrbracket}}. \quad (3 - 41)$$

(When evaluating the mean fractional uncertainty in the distribution factors for Example Problem 2 using Eq. (3-41), the values of $\llbracket D_{ij}^e \rrbracket$ in the first bin of the histogram, in Fig. 3.7(b), are excluded because their values are approximately zero.) Then for Example Problems 1 and 2, Eq. (3-41) gives $(\omega_D/D)_1 = 0.0438$ and $(\omega_D/D)_2 = 0.0543$, which are in excellent agreement with the observed mean relative uncertainty results (solid symbols) in Figs. 3.3 and 3.6. Note that the definition of $\llbracket D_{ij}^e \rrbracket$ does not account for the fact that the uncertainty in a distribution factor increases as its value decreases, which explains why Eq. (3-41) still slightly under-predicts the observed uncertainty in the distribution factors.

While the agreement between Eq. (3-12) averaged over i and j and Eq. (3-41) is gratifying, Eq. (3-41) by itself cannot be used to predict the mean relative uncertainty corresponding to a specified number of surface element and rays traced per surface element. What is needed to establish Eq. (3-41) as a useful tool for predicting the global mean relative uncertainty of the distribution factors is a catalog of relationships between $\llbracket D_{ij}^e \rrbracket$ and $\langle\langle D_{ij}^e \rangle\rangle = \frac{1}{n}$ of the form $\llbracket D_{ij}^e \rrbracket n = f(\varepsilon, geometry)$ for the various generic enclosure types. Such a catalog is the subject of Chapter 4.

3.5. Experimental design of MCRT algorithms

We can now apply the statistical principles developed here to the design of MCRT algorithms. That is, for a specified number of surface elements, we seek the number

of energy bundles N that must be traced per surface element to attain, to a stated level of confidence, a specified uncertainty in the surface net heat flux results. We continue to consider that the temperature is specified on all of the surface elements of a gray diffuse-specular enclosure. Furthermore, we assume that the relative uncertainties in surface temperature and surface emissivity, as well as the desired uncertainty in surface net heat flux relative to the local emitted flux, have been specified in advance, all to the same level of confidence. Then experimental design of the MCRT model may be divided into two steps: (1) determine the relative uncertainty in the distribution factors consistent with obtaining the desired uncertainty in the surface net heat flux, and (2) determine the minimum number of energy bundles that must be traced per surface element to achieve the required uncertainty in the distribution factors.

Step 1. Determine the mean value of the relative uncertainty in the distribution factors, ω_D/D . Rearranging Eq. (3-26), we obtain

$$\frac{\omega_D}{D} = \frac{\left\{ \left(\left\langle \left\langle \frac{\omega_{q_i}}{\varepsilon_i \sigma T_i^4} \right\rangle \right\rangle \right)^2 - \left[\left(\frac{\omega_\varepsilon}{\varepsilon} \right)^2 + \left(4 \frac{\omega_T}{T} \right)^2 \right] \left[1 + \left(\left\langle \left\langle \left(\frac{T_j}{T_i} \right)^4 \right\rangle \right\rangle \right)^2 \right] \right\}^{\frac{1}{2}}}{\left(\left\langle \left\langle \left(\frac{T_j}{T_i} \right)^4 \right\rangle \right\rangle \right)}.$$

(3 – 42)

Step 2. Determine the minimum number of rays that must be traced per surface element. Knowing the desired mean relative uncertainty in the distribution factors, we rearrange Eq. (3-5) to obtain

$$N = (n - 1) \left(\frac{W_c}{\omega_D/D} \right)^2.$$

(3 – 43)

Note that the accuracy of this procedure could be significantly improved by replacing n in Eq. (3-43) with $1/\llbracket D_{ij}^e \rrbracket$. However, this would require *a priori* knowledge of the median of the distribution factor histogram. This goal is achieved in Section 4.3; indeed Chapter 4 is dedicated to predicting the median for a given enclosure.

3.6. Conclusions and recommendations

We have developed and demonstrated a formalism, based on well-established principles of statistical inference, for defining the uncertainty in the estimation of radiation distribution factors and in the heat transfer results obtained using them, at least for the important special case of specified surface temperatures. Furthermore, we have extended this formalism to permit prediction of uncertainty in radiation distribution factors and radiation heat transfer results as a function of the number of surface elements and the number of rays traced per surface element. Finally, we have indicated how this formalism can be used in the design of MCRT experiments; specifically, how it can be used to determine the *a priori* number of rays that must be traced in order to obtain the desired accuracy of radiation heat transfer results. While the results presented here are demonstrated only for the case of diffuse gray enclosures, no step in the analysis leading to Eqs. (3-5) and (3-26) depends essentially on this assumption for its validity; i.e., the derivation does not depend on the values of the distribution factors just as it does not depend on the enclosure geometry.

While Eq. (3-5) is convenient for use in estimating the mean uncertainty in the distribution factors and in the corresponding heat transfer results for a given combination of number of surface elements and number of rays traced per surface element, a better estimate is available if Eq. (3-5) can be replaced by Eq. (3-41). Chapter 4 investigates the suitability of a correlation of the form $\llbracket D_{ij}^e \rrbracket n = f(\varepsilon, geometry)$ that would make this possible.

The development elaborated here is based on diffuse gray enclosures filled with transparent media. However, once the distribution factors have been obtained, nothing in the theory excludes its extension to the case of bidirectional spectral enclosures. The development beginning with Eq. (3-13) and leading to the equivalent of Eq. (3-26) would be straightforward, while Eqs. (3-5), (3-12), and (3-41) would remain unchanged. Finally, the major complications associated with extension of the formulation to enclosures containing a participating medium would be those associated with the inherently greater complexity of computing the distribution factors. In addition, new versions of Eqs. (3-13) through (3-26) would need to be derived, but their derivation would follow the same logic as presented here.

Chapter 4:

Uncertainty Analysis in the MCRT Environment – Part 2

In Chapter 3, it is established that the uncertainty in heat transfer results obtained using the Monte Carlo ray-trace method is related to the median $[[D_{ij}^e]]$ of the radiation distribution factor histogram. The value of this discovery would be significantly enhanced if the median could be known *a priori* without first computing the distribution factors. This would allow the user to determine the number of rays required to achieve the desired accuracy of a subsequent heat transfer analysis. Presented is a correlation for the median of the distribution factor histogram as a function of emissivity and the number of surface elements defining an enclosure. This chapter is based on a peer-reviewed article by the author published in the **Journal of Heat Transfer** entitled “Estimation and use of the

radiation distribution factor median for predicting uncertainty in the Monte Carlo ray-trace method” [80].

4.1. Median of the distribution factor histogram and its importance

In Chapter 3, we postulate that the histogram of the elements of the radiation distribution factor matrix is a unique characteristic for each enclosure, and that its median is a key parameter for predicting the uncertainty of results obtained using the MCRT method. In the current chapter, we identify a new dimensionless parameter whose value can be used, along with the emissivity and number of surface elements into which the enclosure is divided, to predict the median without actually carrying out a costly Monte Carlo ray-trace.

In the absence of a participating medium, if the surface temperature distribution T_j is specified within a diffuse gray enclosure, the corresponding surface net heat flux distribution is related to the distribution factor matrix by Eqs. (3-2) and (3-3). In Eq. (3-2), recall that ε_i is the emissivity of surface i and n is the number of surface elements making up the enclosure. Chapter 3 describes an approach for assessing the uncertainty in the heat transfer results obtained using the MCRT method based on the known uncertainties in the distribution factors, the temperature distribution, and the surface emissivities. An expression for estimating the *mean relative uncertainty* in the heat transfer result,

$$\begin{aligned} & \left\langle \frac{\omega_{q_i}}{\varepsilon_i \sigma T_i^4} \right\rangle_i \\ & \approx \pm \sqrt{\left[\left(\frac{\omega_\varepsilon}{\varepsilon} \right)^2 + \left(4 \frac{\omega_T}{T} \right)^2 \right] \left[1 + \left(\left\langle \left\langle \left(\frac{T_j}{T_i} \right)^4 \right\rangle \right\rangle \right)^2 \right] + \left(\frac{\omega_D}{D} \right)^2 \left(\left\langle \left\langle \left(\frac{T_j}{T_i} \right)^4 \right\rangle \right\rangle \right)^2}, \end{aligned} \quad (3-26)$$

is derived, and confirmed through a series of examples. In Eq. (3-26) $\left\langle\left\langle\left(\frac{T_j}{T_i}\right)^4\right\rangle\right\rangle$ is the *mean fourth-power temperature spread*,

$$\left\langle\left\langle\left(\frac{T_j}{T_i}\right)^4\right\rangle\right\rangle = \left\langle\left\langle\left(\frac{T_j}{T_i}\right)^4\right\rangle_j\right\rangle_i \equiv \frac{1}{n^2} \sum_{i=1}^n \sum_{j=1}^n \left(\frac{T_j}{T_i}\right)^4. \quad (3-27)$$

Recall that ω represents the uncertainty in the quantity indicated by the subscript and the symbol $\langle x \rangle$ indicates the mean of the enclosed quantity x with respect to the relevant index, i or j . Equation (3-26) is formally derived as an approximation; however, in Chapter 3 the difference between heat flux uncertainty predicted using it and observed heat flux variability is typically within about one percent.

The mean relative uncertainties in emissivity $\omega_\varepsilon/\varepsilon$ and temperature ω_T/T in Eq. (3-26) are assumed to be known with the same level of confidence and the fractional uncertainty in the distribution factors ω_D/D is now known to be well estimated by

$$\frac{\omega_D}{D} \approx \pm W_c \sqrt{\frac{1-\nu}{N\nu}}. \quad (4-1)$$

In Eq. (4-1) the symbol for the median $\llbracket D_{ij}^e \rrbracket$ has been replaced by ν for notational simplicity. The critical value of the W statistic W_c in Eq. (4-1) is tabulated in standard texts as a function of the level of confidence. For example, if ω_D/D is to be estimated with a 95-percent level of confidence, then $W_c = 1.960$. The symbol N in Eq. (4-1) represents the number of rays traced per surface element when computing the distribution factors using the MCRT method, and ν represents the *median* of the histogram of the distribution factors. In the current chapter, we demonstrate that the median ν is a property of the enclosure related to its shape, nominal emissivity, and the number of surface elements into which it is divided.

Equations (3-26), (3-27) and (4-1) clearly establish the critical role played by the median ν of the distribution factor histogram in placing error bars on heat transfer results predicted using the MCRT method. Once known for a given enclosure, the median can be used with Eq. (4-1) to compute the relative uncertainty in the distribution factors, after which Eqs. (3-26) and (3-27) can be used to bound the uncertainty in the heat transfer results. In principle, the median of the distribution factor histogram is computed from the distribution factors themselves, as described in Section 4.2. However, the utility of Eqs. (3-26), (3-27) and (4-1) would be significantly enhanced if they could somehow be used to determine the minimum number N of rays that must be traced to ensure the desired accuracy of the heat transfer results. The goal of this chapter then is to establish a methodology for obtaining ν without first performing a costly and time-consuming ray-trace.

4.2. Statistical properties of the distribution factor matrix

The histogram of the elements of any matrix may be obtained using a function available in recent versions of both Excel and Matlab. As an example, we consider the histogram, illustrated in Fig. 4.1(a), of the distribution factor matrix for a cubical enclosure whose walls have been subdivided into $n = 384$ equal-area surface elements, each having an emissivity of 0.55. The corresponding D_{ij} matrix will have n^2 elements. The mean value of the distribution factors, $\mu = 1/n$, is indicated in the figure. Also indicated is the median of the histogram, $\nu = \bar{D}_K$, where K is the value of k for which

$$CFD(K) \equiv \sum_{k=1}^K \bar{D}_k \Delta D_k = \frac{n^2}{2}. \quad (4-2)$$

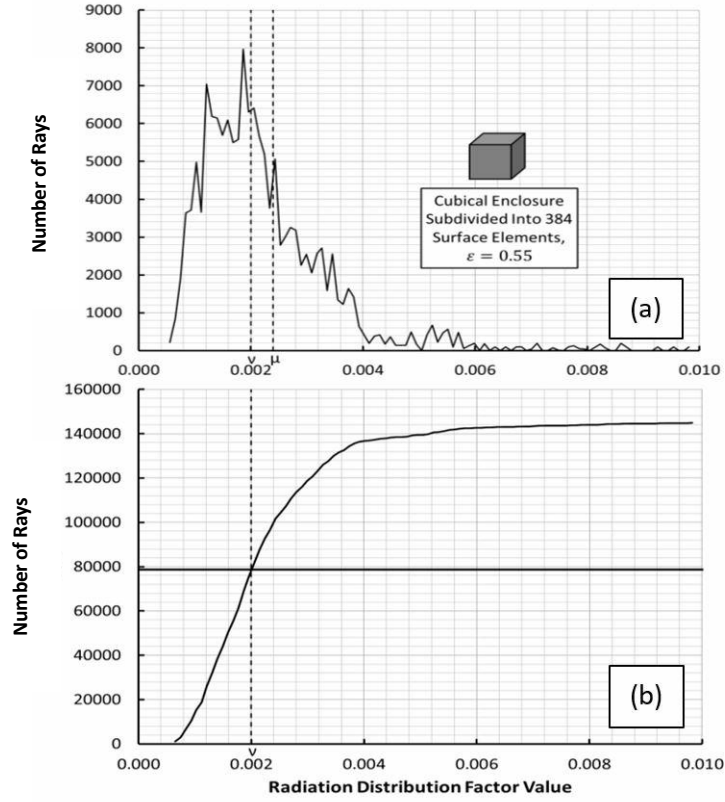


Figure 4.1. (a) Histogram and (b) Cumulative Density Function (CDF) for the radiation distribution factor matrix of a cubic enclosure.

In Eq. (4-2), \bar{D}_k is the mean value of the distribution factors included in bin k , whose width is ΔD_k , and $CDF(k)$ is the corresponding cumulative density function shown in Fig. 4.1(b). The median is the value of \bar{D}_k for which $CDF(K)$ attains one-half of its maximum value, which means that the number of distribution factors binned to the left of v is equal to the number binned to the right. In the figure, the abscissa has been truncated at $D_{ij} = 0.010$ in order to emphasize the behavior of the histogram and CDF in the vicinity of the mean and median values.

The “skew” of the histogram describes its tendency to “lean” to the left or right. For example, the histogram in Fig. 4.1(a) is said to be biased to the left because more distribution factors are binned to the left of the mean μ than to the right; i.e., μ is greater than ν . Several definitions of the skew of a histogram are given in the literature. We find it convenient to define the *relative skew*,

$$S_r \equiv \frac{\mu - \nu}{\mu}, \quad (4 - 3)$$

so that when $S_r > 0$ the histogram is biased to the left and when $S_r < 0$ the histogram is biased to the right. According to this definition, a Gaussian histogram would have a relative skew of zero. Sought is a correlation for the relative skew as a function of the enclosure shape, surface emissivity, and number of surface elements into which it is divided.

4.3. Experimental study of skew for two-dimensional enclosures

We begin by apologizing to those who cling to the belief that the term “experiment” should be applied only to procedures involving physical devices such as lasers and thermographic imagers. In the realm of radiation heat transfer analysis using the MCRT method, the numerical procedure by which the life cycles of rays are determined by applying the rules of geometrical optics and stochastics is commonly referred to as a “numerical experiment.” It is in this sense that we claim to “measure” the thermal-radiative performance of various enclosures. Use of the term is encouraged by the fact that generally different results are obtained when the same simulation is performed multiple times, each time using the same enclosure but a different sequence of pseudo-random numbers. Moreover, the different results tend to be statistically distributed in much the same way as in experiments carried out in a laboratory.

We initially limit our study to so-called two-dimensional enclosures; i.e., to enclosures for which one of the three dimensions greatly exceeds the other two. Long ducts having various cross-sectional shapes are a common example. Specifically, we initially confine the study to long, empty ducts whose cross-sections are any of the family of regular polygons, ranging from triangles to circles. The decision to initially limit the study to two-dimensional enclosures is motivated by the fact that we seek general results in a world populated by an unlimited number of potential enclosure geometries. Clearly, we cannot consider all possibilities in a reasonably limited study; more complex geometries will have to await their turn. However, the study of three-dimensional enclosures in the previous chapter, including one with an internal obstruction, supports the presumption that the method presented here is not limited to regular two-dimensional enclosures.

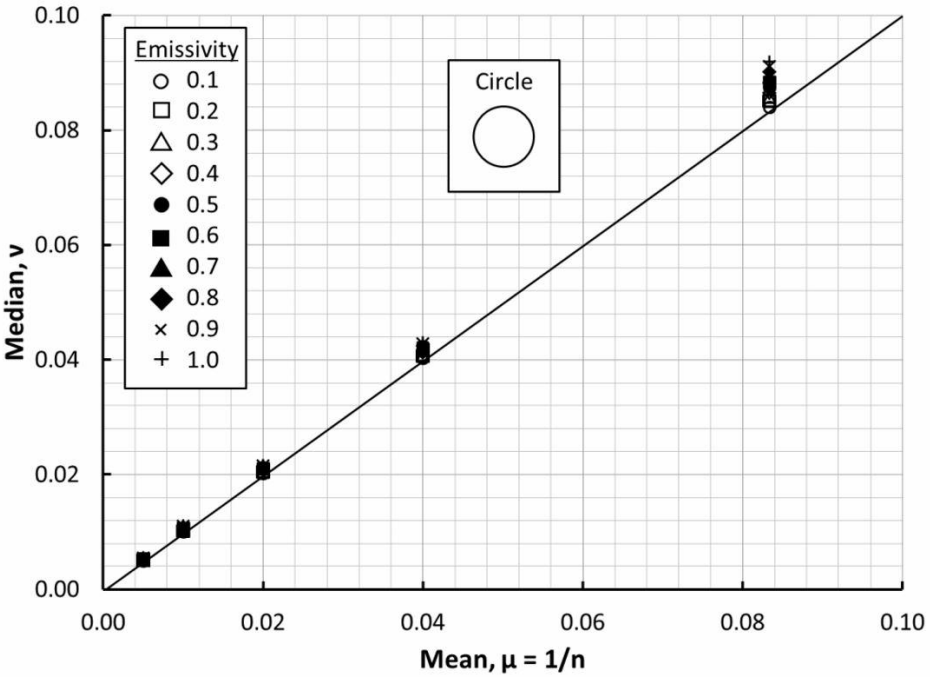


Figure 4.2. The median v of the distribution factor histogram, exceeds the mean $\mu = 1/n$ for all combinations of the number n of surface elements and emissivity ε for a long circular duct.

The author has created a convenient windows application [67] that uses the MCRT method to compute the radiation distribution factors among any number of surface elements making up any two-dimensional diffuse gray enclosure. We have used the application to compute the distribution factors for enclosures whose cross-sections are regular triangles, squares, pentagons, hexagons, heptagons, octagons, and circles. We have also used it to study acute and obtuse isosceles triangular cross-sections and a cross-section consisting of a circle concentric with a square. The Monte Carlo ray-trace method for two-dimensional geometries is verified and explained in Chapter 2.

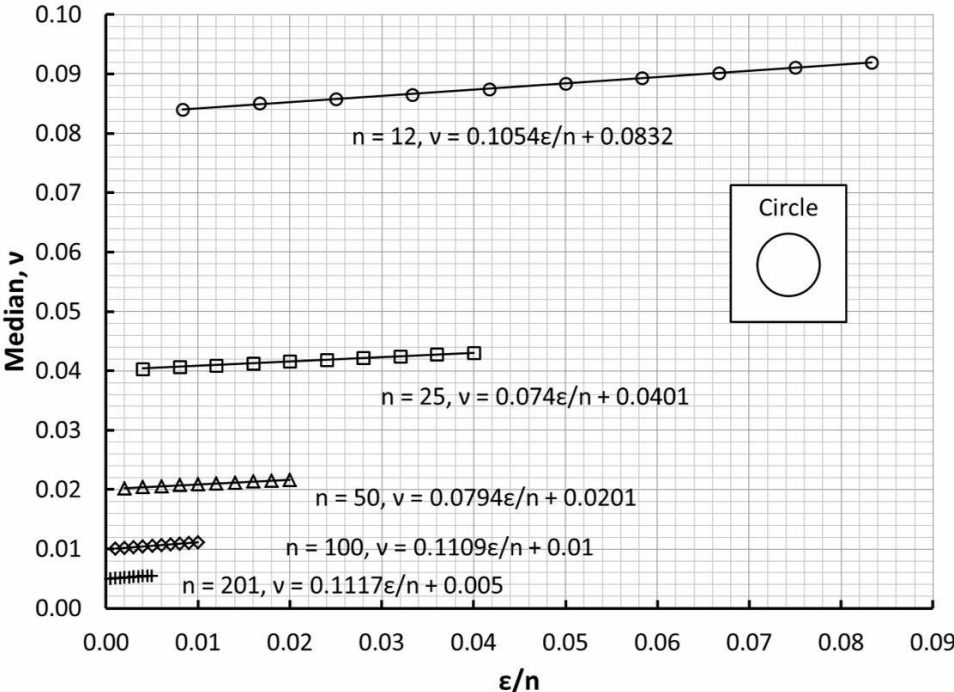


Figure 4.3. Initial attempt at correlating the median with emissivity and the number of surface elements.

We begin by using the two-dimensional MCRT engine to compute the distribution factor matrices for a long circular duct subdivided into $n = 12, 25, 50, 100,$ and 201 surface elements whose emissivities are $\epsilon = 0.1, 0.2, 0.3, 0.4, 0.5, 0.6, 0.7, 0.8, 0.9,$

and 1.0. For each combination of n and ε we trace two million rays per surface element to obtain the corresponding distribution factor matrices, D_{ij} , where $1 \leq i \leq n$ and $1 \leq j \leq n$. The results are summarized in Fig. 4.2, which is a plot of the median of the distribution factor histogram as a function of the mean for all values of emissivity. We see that in each of the fifty cases represented the median ν exceeds the mean μ ; that is, the relative skew defined by Eq. (4-3) is always negative. Based on consideration of Fig. 4.2, we hypothesize the existence of a correlation of the form $\nu = f(\varepsilon/n)$. When we put this hypothesis to the test, we obtain Fig. 4.3. The expressions for ν in the figure are linear least-square fits to the data.

Inspection of Fig. 4.3 shows that the initial attempt at a correlation is still a function of the number of surface elements. Figure 4.4 is obtained by computing the mean slope $S = 0.0928$ of the linear expressions in Fig. 4.3, and then applying the correlation

$$\nu = \frac{1 + S\varepsilon}{n}. \quad (4 - 4)$$

Inspection of Fig. 4.4 reveals that the groups of symbols lie along a more-or-less straight line, with each group slightly tilted with respect to the correlation represented by Eq. (4-4). This is because the slopes corresponding to the various fits in Fig. 4.3 are each slightly different from the average slope S . Although Eq. (4-4) has been derived here on the basis of a specific two-dimensional enclosure, we shall see that its general form applies equally well to all two- and three-dimensional enclosures subject to certain limitations. Solving Eq. (4-4) for the slope S yields

$$S = -\frac{1}{\varepsilon} \left(\frac{\mu - \nu}{\mu} \right) = -\frac{S_r}{\varepsilon}. \quad (4 - 5)$$

Equation (4-5) reveals that the slope parameter S is the negative of the relative skew scaled by the inverse of the wall emissivity.

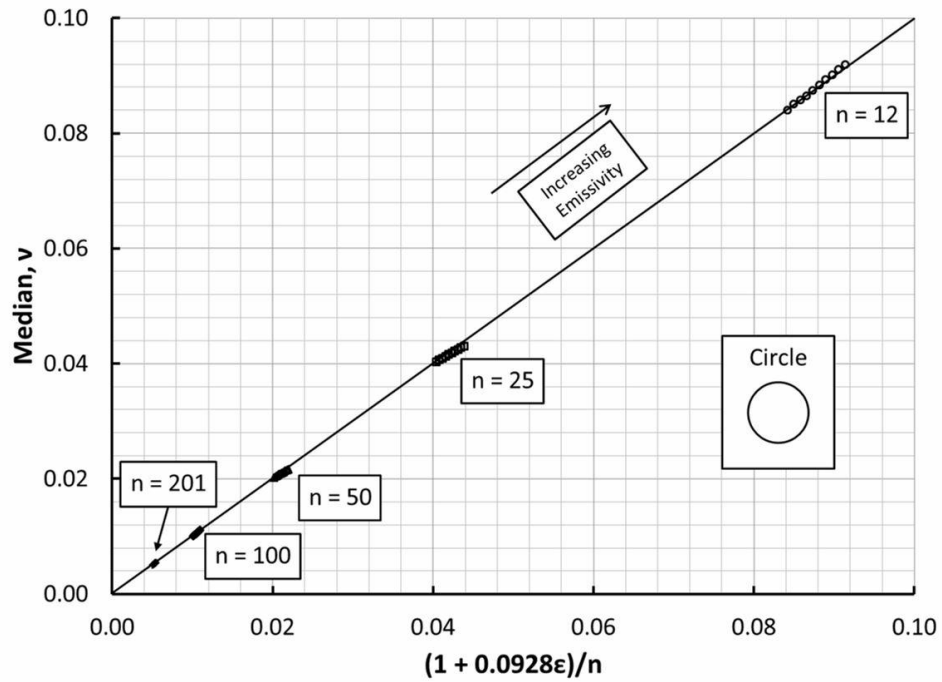


Figure 4.4. The final correlation for the median as a function of emissivity and the number of longitudinal surface elements for a long circular duct.

Results similar to those described above for a long circular duct have been obtained for long regular octagonal, heptagonal, hexagonal, pentagonal, square, and triangular ducts, and are summarized in Figs. 4.5-4.7. In the following discussion, the reader is cautioned to avoid confusing the number of walls, or physical surfaces N making up an enclosure (e.g., $N = 5$ for a pentagon) with the total number of surface elements n into which the walls are subdivided.

Two interesting features of these results should be pointed out. First, note that the sign of the slope parameter S changes from positive to negative between the hexagon, Fig. 4.6(a), and the pentagon, Fig. 4.6(b). For the higher-order regular polygons ($N \geq 6$, including the circle for which $N \rightarrow \infty$) the slope is positive (and so the skew of the distribution factor histogram, is negative), and for the lower-order polygons ($N = 3, 4$ and 5) the slope is negative (and so the skew of the distribution factor histogram is positive).

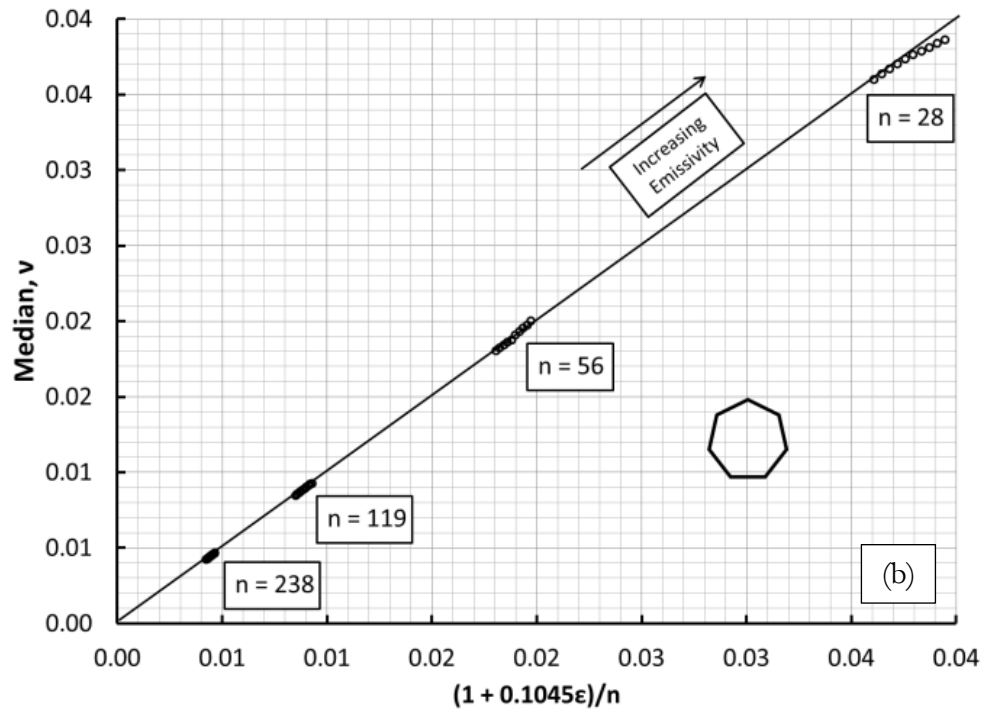
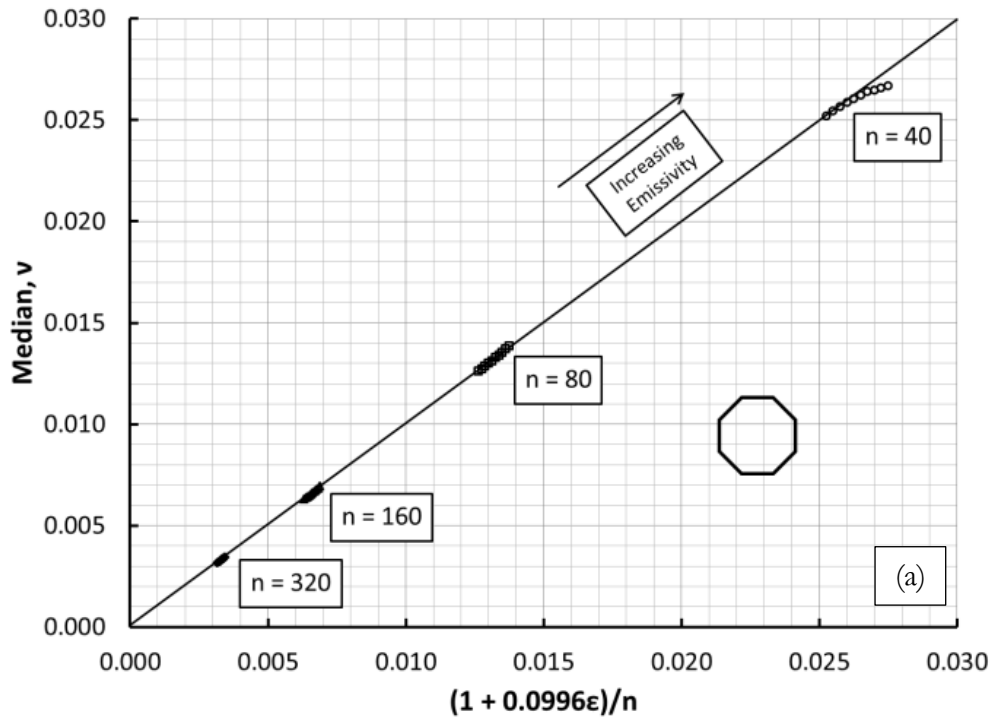


Figure 4.5. Median correlations f or long regular (a) octagonal, (b) heptagonal duct.

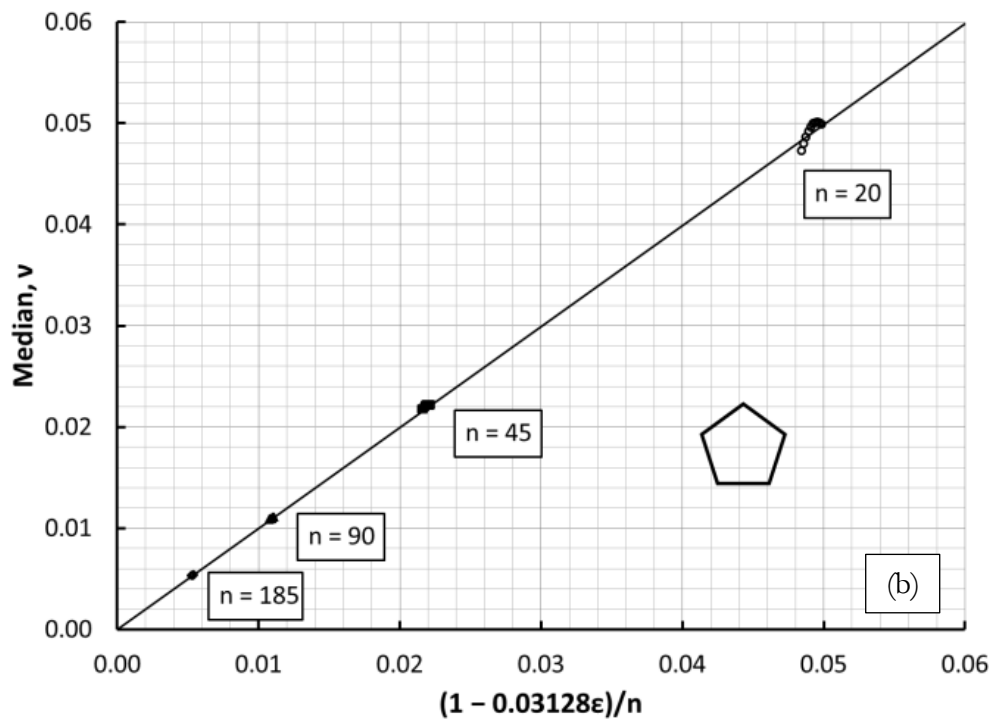
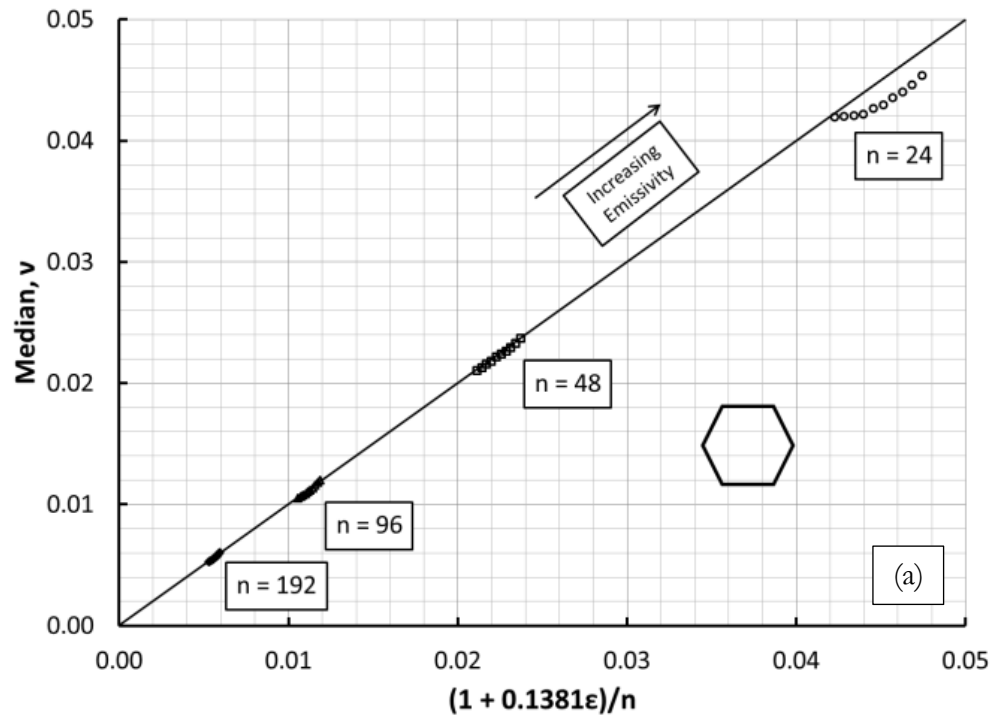


Figure 4.6. Median correlations for long regular (a) hexagonal, (b) pentagonal

duct.

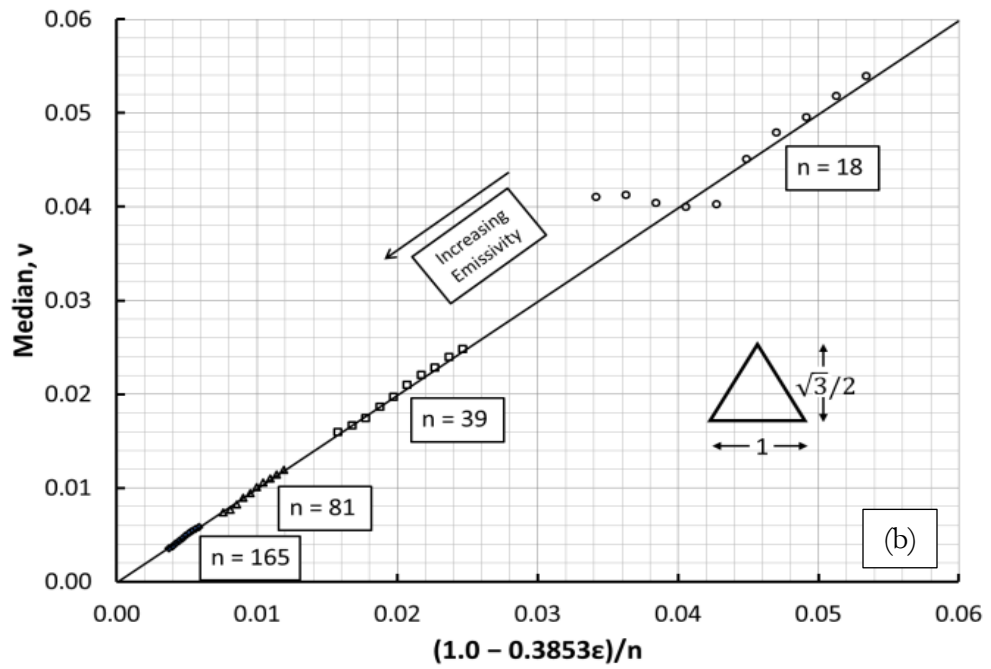
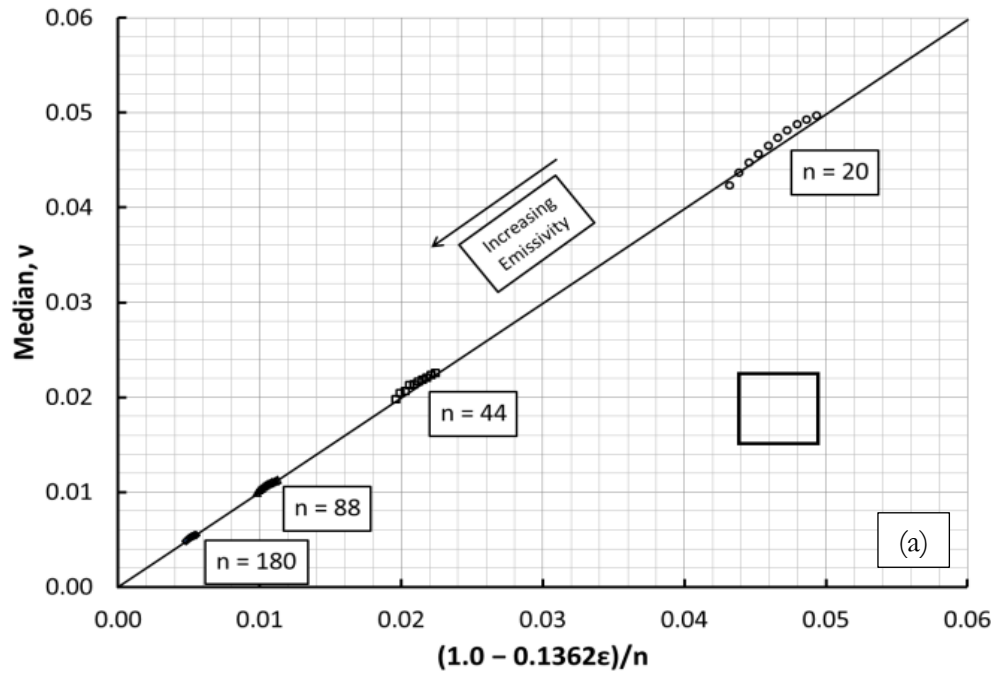


Figure 4.7. Median correlations f or long regular (a) square, (b) triangular duct.

Second, note that for each duct cross-section in Figs. 4.4-4.7, the correlation corresponding to the smallest number of surface elements n (open circles) “tails off”. In each of these cases, the correlation is excellent for small wall emissivity (large reflectivity) but degrades with increasing emissivity (decreasing reflectivity). This trend, which is gradual for the other ducts, is abrupt and spectacular for the triangular duct. Also, the direction of the “tail” rotates clockwise with decreasing polygonal order; pointing to the right for the octagonal, heptagonal, and hexagonal ducts; pointing more or less downward for the pentagonal duct (whose slope parameter S is incidentally near zero); and pointing to the left for square and triangular ducts. In each case the tail points in the direction of increasing wall emissivity. This behavior is evidently dictated by the skew of the distribution factor histogram, which is negative for the lower-order polygons; i.e., biased to the right; and positive for the higher-order pentagons. The skew for the pentagon is near zero. It is noted that all of these cross-sections have in common that they are continuously concave; i.e. no blockage exists among their surfaces.

The degradation of the correlation with decreasing numbers of surface elements and increasing wall emissivity suggests that a minimum number of surface elements are required to adequately model the radiative behavior of an enclosure whose walls have a specified emissivity. In the case of low emissivity (high reflectivity), the radiative behavior of the enclosure can be said to be *reflection dominated*, in which case the number of surface elements is less important. Conversely, in the case of high emissivity (low reflectivity), the radiative behavior of the enclosure can be said to be *geometry dominated*, and so results obtained using the MCRT method are more sensitive to the number of surface elements used.

We have also investigated the radiative behavior of long ducts having isosceles right and acute triangular cross-sections, as well as ducts having internal obstructions. The correlations for the isosceles right and acute triangles are summarized in Fig. 4.8.

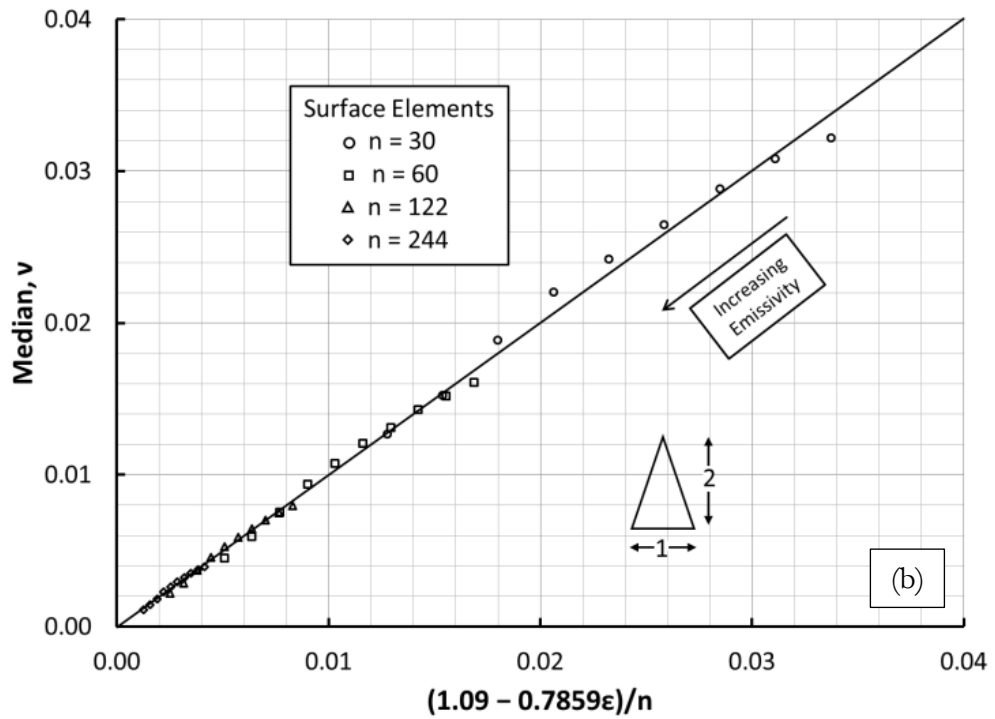
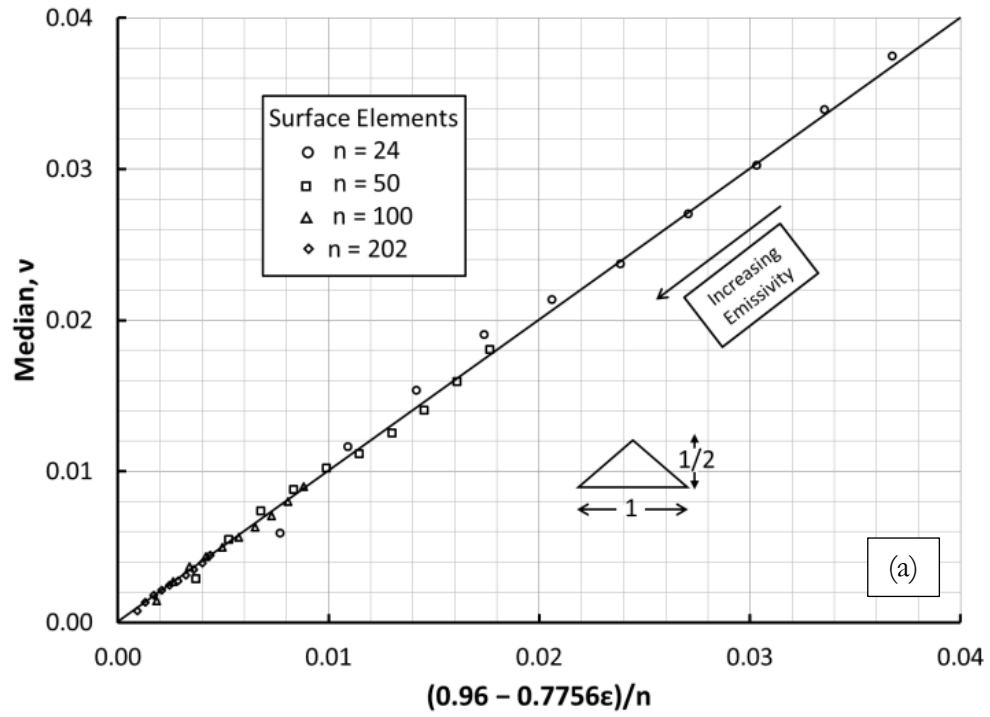


Figure 4.8. Median correlations for long ducts having isosceles (a) right and (b) acute triangular cross-sections.

Inspection of Fig. 4.8 reveals that it has been necessary to account for the departure from the regularity of the isosceles triangles to obtain a good correlation. The lead coefficient, which was unity for the equilateral triangle, has been reduced to 0.96 for the isosceles right triangle in Fig. 4.8(a); and increased to 1.09 for the acute isosceles triangle in Fig. 4.8(b). That is, there seems to be an eccentricity effect.

The distribution factor matrix histogram of all enclosures is characterized by a median and a relative skew, regardless of shape, dimensionality, and surface emissivity. It is therefore natural to speculate that the median will be related to the relative skew as indicated by Eqs. (4-4) and (4-5) regardless of the enclosure geometry. It has already been established in Chapter 3 that Eq. (3-2) is applicable to the case of three-dimensional enclosures, both with and without internal obstructions. Even though Eqs. (4-4) and (4-5) have emerged from consideration of long polygonal cross-section ducts, we fully expect them to apply equally well to three-dimensional enclosures, even those having internal obstructions, at least in the reflection-dominated regime.

Fig. 4.9 shows the result for the long square-cross-section duct containing a cylindrical obstruction, while Fig. 4.10 illustrates a successful attempt to correlate the median of the distribution factor matrix histogram, for the cubical enclosure considered in Fig. 4.1. In the latter figure, the emissivity varies from 0.1 to 1.0 for $n = 96$ and 384. The lead coefficient is once again unity, consistent with the regularity of the geometry.

Figure 4.11 represents a somewhat successful attempt to correlate the median of the distribution factor histogram for the case of a cubical three-dimensional enclosure containing a rectangular obstruction shown in the inset. The correlation works well in the reflection-dominated regime ($\varepsilon < 0.6$ in this case), but less well in the geometry-dominated regime. This is similar to the behavior noted in Fig. 4.9 except that now the departure of the median from the value predicted by the

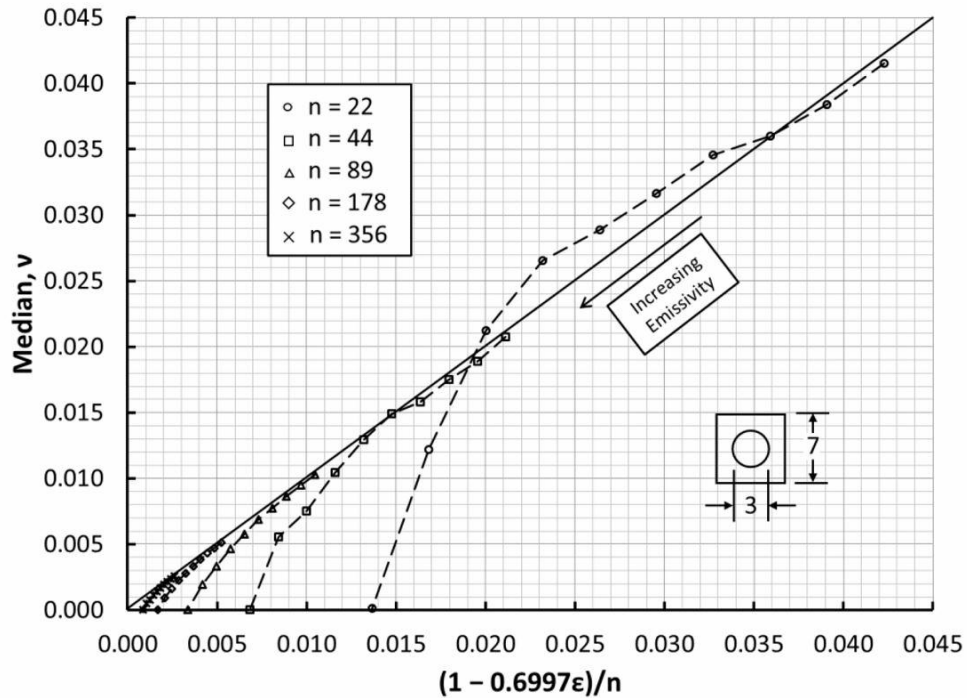


Figure 4.9. Correlation for a long square duct with a concentric circular obstruction.

correlation in the geometry-dominated regime is less severe. This is no doubt because the role played by the obstruction in creating near-zero elements in the distribution factor matrix is less dominant in the geometry of Fig. 4.11 (inset).

Table 4.1 is a summary of the values of the \mathcal{S} -parameters obtained to this point. Also shown in the table are the average angles of the various geometries, where applicable. The average angles are defined as the total of the angles divided by the number of facets. Thus, the definition of a triangle requires that its three included angles sum to 180 deg, and so the average angle will always be 60 deg. Similarly, all polygons are defined by the sum of their included angles and the number of sides, no matter the degree to which they may be distorted. We have seen this rule in action in the case of the three triangular cross-section ducts we have considered. Therefore, if we want to “flatten” an initially regular octagonal duct by increasing

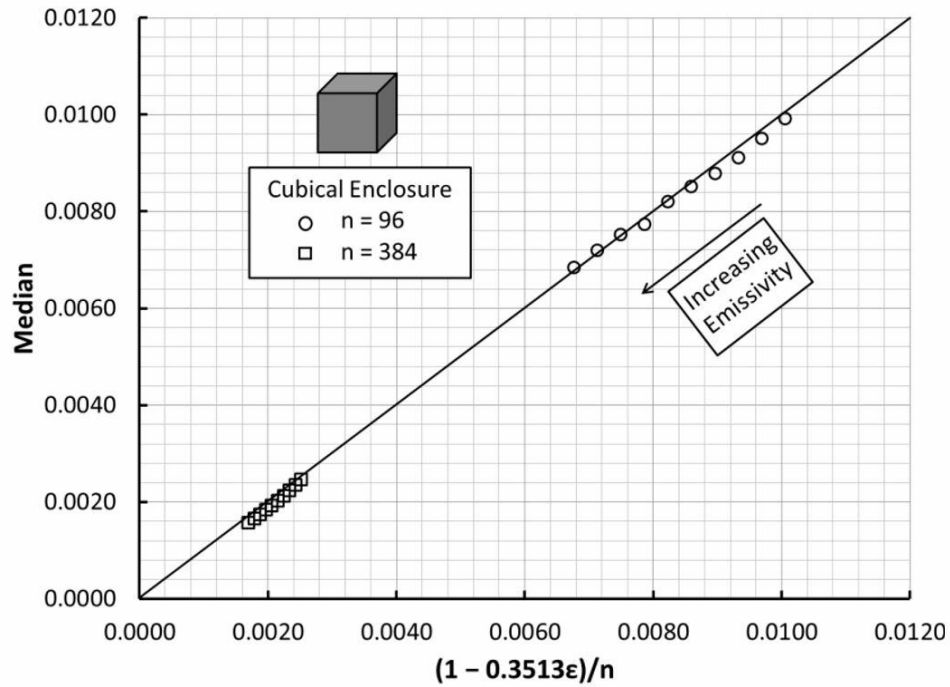


Figure 4.10. Correlation for a long square duct with a concentric circular obstruction.

the two angles at its top and the two at its bottom, we must also decrease the four angles at its flanks (and appropriately adjust the lengths of its eight sides) such that the sum of the angles remains 1080 deg. In this way, for example, we can turn a square into a rhombus, and so forth. Even though, with the exception of the triangle, we have limited the cross-sections of our unobstructed ducts to regular polygons, we might also have considered distorted cross-sections having the same numbers of sides and summations of included angles such that the average angle given in Table 4.1 would remain unchanged. More to the point, it is intuitively pleasing to contemplate the possibility that the S -parameter for a duct having a non-regular polygonal cross-section will be related to that for a duct having a regular polygonal cross-section through an appropriate parameter such as the eccentricity, or aspect ratio, of the cross-section.

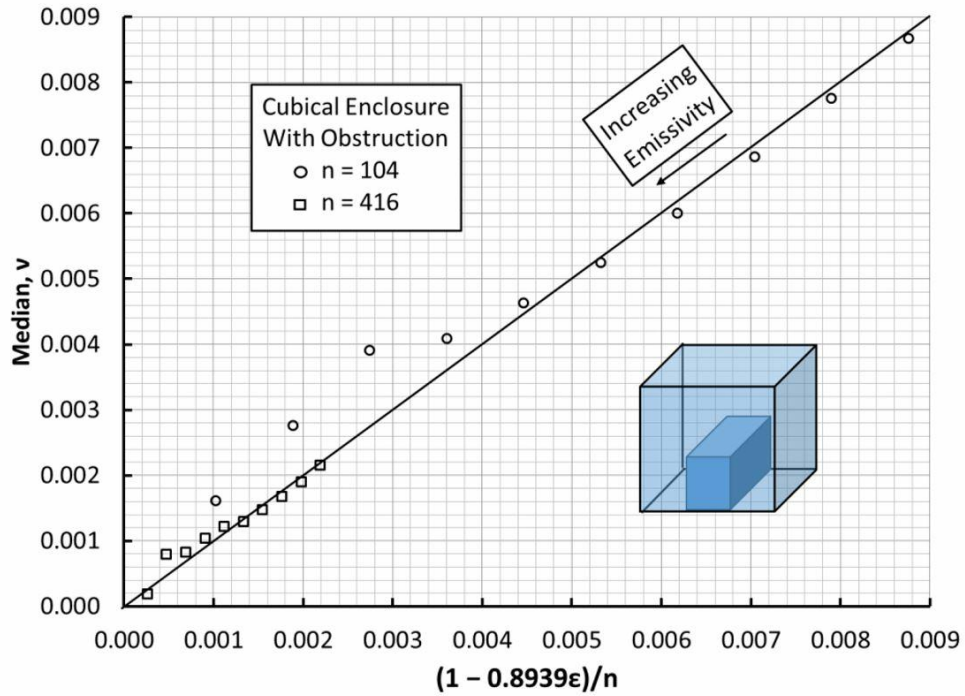


Figure 4.11. Correlation for a cubical enclosure with an internal obstruction.

Figure 4.12 represents the first step toward consolidating the results for the case of all enclosures free of internal obstructions into a grand canonical correlation. It suggests that, to an acceptable approximation, the S -parameter for all of the “open” enclosures considered here can be related to the geometry according to

$$S = A \sin(B - 70), \quad (4 - 6)$$

where A is equal to the negative of the aspect ratio for the case of three-dimensional enclosures and is equal to the negative of one-half of the aspect ratio for the case of two-dimensional (long ducts) enclosures, and B (deg) is the average angle given in Table 4.1. The use of an aspect ratio in the case of a three-dimensional enclosure makes sense only if the enclosure is elongated or shortened in one direction with respect to the other two directions for which the dimensions are approximately the same. Equation (4-6) may be considered valid for values ranging from -0.8 to $+0.0928$, beyond which the latter value should be used.

Table 4.1. Summary of the S -parameter results.

<u>Geometry</u>	<u>Average Angle (deg)</u>	<u>S-Parameter</u>
<u>Two-Dimensional</u>		
No Blockage:		
Circular	N/A	+0.0928
Octagonal	135	+0.0996
Heptagonal	128.57	+0.1045
Hexagonal	120	+0.1381
Hybrid Square Hexagonal	108	+0.00315
Pentagonal	108	-0.0313
Square	90	-0.1362
Equilateral Triangular	60	-0.4175
Isosceles Right Triangular	60	-0.7721
Acute Isosceles Triangular	60	-0.7895
With Blockage:		
Circle-In-Square	N/A	-0.6997
<u>Three-Dimensional</u>		
No Blockage:		
Cubical	90	-0.3513
With Blockage:		
Cubical	N/A	-0.8939

4.4. Discussion and interpretation of results

The slope parameter S central to the correlation presented here is clearly related to, and may even be unique to, enclosure geometry; however, the nature of that relationship remains elusive. One can imagine future conversations involving a particular radiation heat transfer analysis in which meaningful reference is made to a certain “positive- S enclosure,” or to an enclosure having a particular “ S value.” Clearly it would be useful to know the value of the S parameter for an enclosure before embarking on its thermal radiative analysis, because this would permit determination of the number of rays per surface element required to assure a desired level of accuracy of the results.

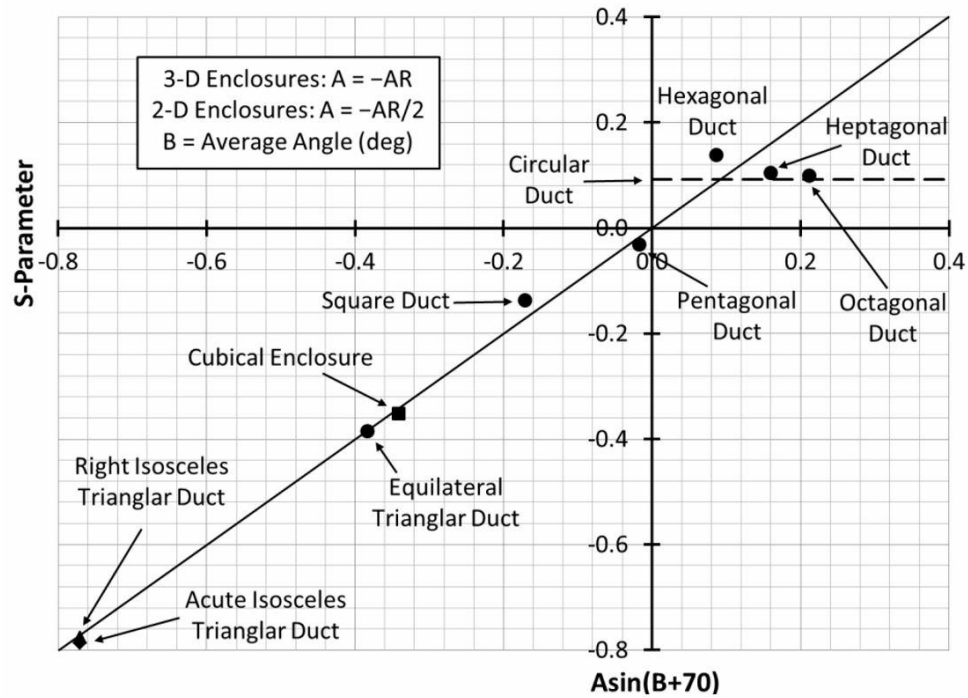


Figure 4.12. An attempt to correlate the S-parameter with enclosure geometry.

Is it possible to find, or at least estimate, the value of the S parameter without first performing a ray-trace to obtain the elements of the distribution factor matrix? For the limited population of enclosures considered in this communication, the answer is now “yes,” because the results summarized in Table 4.1 are available to the community for this purpose. Perhaps one day a web site will be available to which a user can upload enclosure geometry and retrieve the value of the corresponding S parameter. In the meantime, we suggest that it might be possible to estimate the S parameter for an enclosure as the surface-weighted average of the S parameters for two or more enclosures from which it is fabricated. This somewhat whimsical idea has not yet been systematically pursued. However, Fig. 4.13 provides the median correlation for a hybrid two-dimensional duct created by combining a square cross-section with a hexagonal cross-section. The correlation obtained is excellent and the value of the corresponding S parameter, 0.00315, is essentially

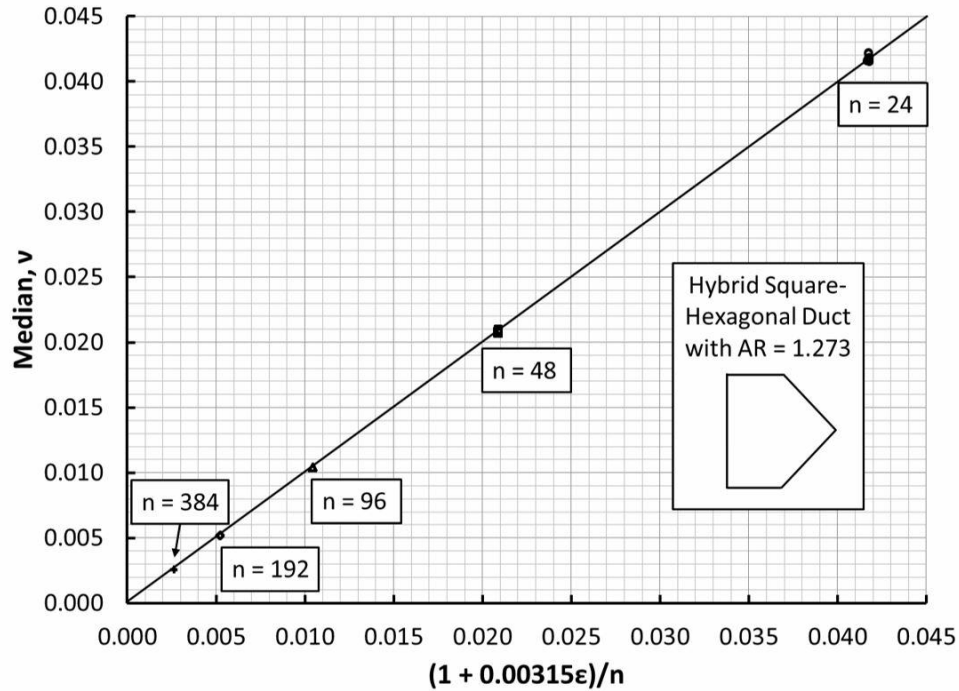


Figure 4.13. Median correlation for a hybrid square-hexagonal duct having an aspect ratio (AR) of 1.273.

zero. We note that, if this point is plotted along the correlation line in Fig. 4.12, it falls midway between the square duct and the hexagonal duct, as might be anticipated.

4.5. Conclusions

Based on the investigation documented in Chapter 3, the median of the radiation distribution factor histogram is known to be a reliable predictor of uncertainty in the MCRT method. A correlation is presented that allows prediction of the median for a given enclosure geometry based on the wall emissivity and the number of surface elements into which the enclosure is divided. We conclude on the basis of results presented in the current chapter that, if an enclosure is continuously concave, is divided into a sufficiently large number of surface elements, is devoid of acute angles, and has no internal obstructions, the correlation is valid for all

values of surface emissivity. Otherwise, the validity of the correlation is found to be dictated by the degree to which radiation is reflection-dominated or geometry-dominated, with performance being relatively high in the reflection-dominated limit and relatively low in the geometry-dominated limit. Geometry-dominated radiation is favored by acute angles and internal obstructions, while reflection-dominated radiation is favored by low emissivity, obtuse angles, and a lack of internal obstructions. In the geometry-dominated limit the enclosure must be divided into a greater number of surface elements for the correlation to be valid, and in the presence of internal obstructions, the correlation degrades and eventually fails as the geometry-dominated limit is approached.

Chapter 5:

Introduction to the Artificial Neural Network (ANN)

The application of the artificial neural network (ANN), which is the basis of AI methodologies, to a variety of real-world problems is an on-going active research area. However, the application of the ANN to thermal science and engineering is still in its infancy and is the subject of ever-increasing attention. This is due to the inherent complexity of thermal science and engineering systems, for which realistic models are often beyond the scope of traditional analysis. Artificial intelligence, or machine learning, is a state-of-the-art technology that is ripe for applications in the field of remote sensing and applied optics. This chapter is a brief introduction to Artificial Neural Networks. Some of the material in this chapter is repeated from Refs. [63, 81], peer-reviewed articles by the author published in the **Journal of Heat Transfer and Remote Sensing**.

5.1. Background

Artificial neural networks (ANNs) are nonlinear mapping systems with structures based on principles inspired by the human biological nervous system. They provide a fundamentally different approach from other numerical solution methods for forecasting the future. Artificial neural networks can accurately model the inherent relationship between sets of input and output data without reference to the underlying physical system, and yet they are able to consider all the parameters affecting the physical system. Various considerations such as nonlinearity, multiplicity of variables and parameters, and noisy and uncertain input and output values are easily dealt with. Artificial neural networks depend on neither prior knowledge of correlations nor recourse to iterative methods, but rather require only a population of input/output samples. These latter are used to train the neural network which, once trained, is able to produce meaningful outputs in response to the introduction of test inputs not used in training. Artificial neural networks consist of a large number of processing units which run in parallel to achieve results whose accuracy is comparable to that obtained using computationally more expensive traditional approaches. They are also able to perform dynamic modeling and adaptive control tasks in the presence of abrupt changes in system parameters and imposed control signals. Complexities not easily treated by traditional approaches to thermal system analysis can be accurately modeled with significantly less computing time using an ANN.

5.2. The ANN in thermal applications

Artificial neural networks have been under development for about four decades. They have been widely used in many engineering applications because of their ability to obtain solutions more easily, frequently with an accuracy comparable to that of higher-order models [82]. In recent years, ANNs have been used in various thermal applications describing heat transfer in solar energy systems, design of steam generating plants, estimation of heating loads of buildings, waste heat

recovery heat exchangers, and related performance prediction and dynamic control applications. Thibault and Grandjean [83] used an ANN for heat transfer data analysis. Parcheco-Vega et al. [84] applied ANNs for modeling the heat transfer phenomena in fin-tube refrigerating heat exchanger systems. An ANN algorithm was used by Bechtler et al. [85] to model the steady-state performance of a vapor-compression liquid heat pump. Lazrak et al. [86] modelled a dynamic absorption chiller using artificial neural networks. An ANN model was developed to predict the convective heat transfer coefficient during condensation of R134 in inclined tubes [87]. Chang et al. [88] predicted heat transfer of supercritical water using ANNs. Ye et al. [89] proposed a novel ANN model for predicting convective heat transfer in sCO_2 . Kaya and Hajimirza designed a two-layer ANN surrogate model to estimate the optical absorptivity of the solar ultra-thin organic cells [90, 91]. Additional investigations of heat transfer using ANNs have also been reported [92, 93].

The cited applications demonstrate that ANNs are often well suited to thermal analysis of engineering systems. This is especially true when performing a parametric study involving repetitive solution of a complex model, in which case it is desirable to accelerate the analysis without comprising the underlying physics.

Although a variety analytical and numerical approaches have been employed in radiation heat transfer analysis, to the author's knowledge ANN methods have yet to be applied in this area. This further motivates the work in this and the following chapters, which demonstrate the applicability of ANNs to the radiation heat transfer analysis.

5.3. Description of the ANN

An artificial neural network is an information processing paradigm consisting of a large number of simple processing elements called neurons, or nodes, organized in layers [39]. The node layers are organized into three groups: the input layer, one or

more hidden layers, and an output layer. Each layer is occupied by a number of nodes, as illustrated in Fig. 5.1. All the nodes of each hidden layer are connected to all nodes of the previous and following layers by means of synaptic connectors. Each connector is characterized by a synaptic weight. The input layer is used to designate the parameters for the problem under consideration, while the output layer corresponds to the unknown variables characterizing the performance of the system. The weights of the connectors determine the relative importance of the signals from all the nodes in the previous layer. At each hidden-layer node, the node input consists of a sum of all the outputs of the nodes in the previous layer, each modified by an individual interconnector weight. At each hidden node, the node output is determined by an activation function, which performs nonlinear input-output transformations. The information treated by the connector and node operations is introduced at the input layer, and this propagates forward toward the output layer [94]. Such ANNs are known as feed-forward networks, which is the type used in the current study. Figure 5.1 is a schematic representation of typical feed-forward architecture. The configuration shown has one input layer, two hidden layers, and one output layer.

The error at each output node can be determined by comparing the calculated feed-forward result with the known outputs obtained from the training data. Training of the network adjusts its weights to minimize the errors between the ANN result and known output. The training procedure for feed-forward networks is known as the supervised back propagation (BP) learning scheme, where the weights and biases are adjusted layer by layer from the output layer toward the input layer [95]. The mathematical basis, the procedures for training and testing the ANNs, and more descriptions of the BP algorithm can be found elsewhere [96].

Overfitting may occur because of an overly complex model with too many parameters. A model that is overfitted is inaccurate because the trend does not reflect the reality present in the data. The presence of overfitting can be revealed if

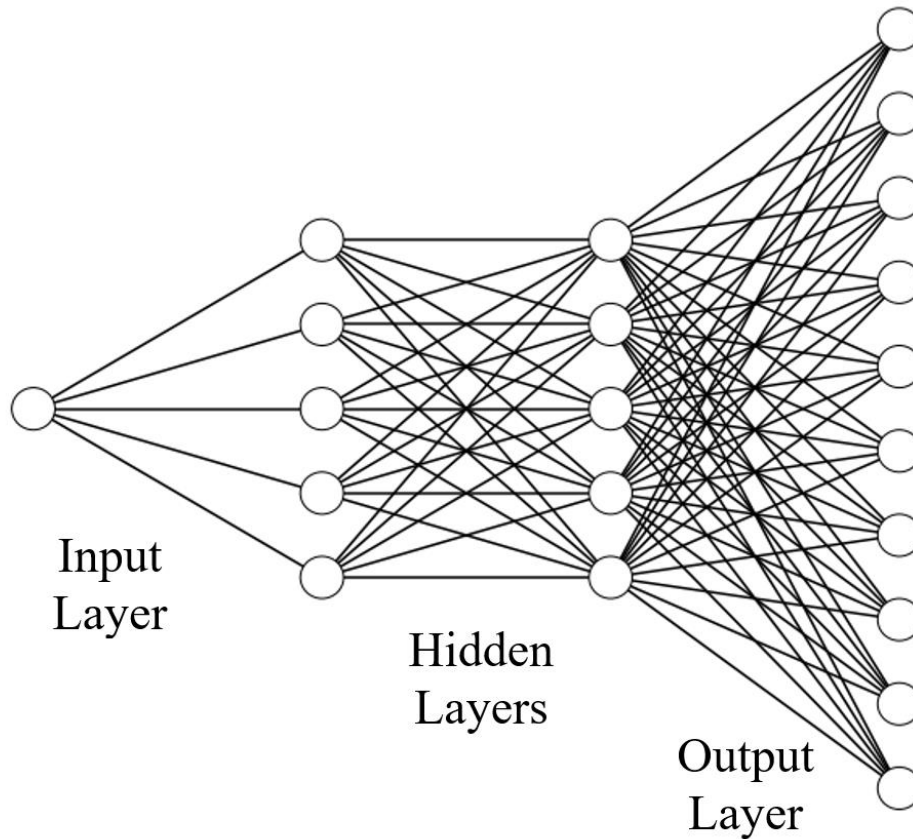


Figure 5.1. Configuration of a 1-5-5-10 artificial neural network.

the model produces good results on the seen data (training set) but performs poorly on the unseen data (test set). This is a very important consideration since we want our model to make predictions based on the data that it has never seen before. Therefore, additional structured test scenes are introduced involving data completely unknown to the ANN training process. Techniques such as early stopping, data augmentation, regularization, and drop-out are available to overcome this problem if detected [96].

Different optimization techniques exist for training a neural network. The Adam optimization algorithm has shown great potential and is used in the efforts considered in this dissertation to converge the ANN output with the target scenes during the training process. This stochastic optimization method is straightforward

to implement, is computationally efficient, has minimal memory requirements, is invariant to diagonal rescaling of the gradients, and is well suited for problems that are large in terms of data. Further details about Adam optimization can be found in Ref. [97].

Mean-squared error (MSE) is used as the objective loss function for the ANN optimization in this dissertation. An inherent weakness of the BP algorithm is that it can converge to a local minimum. One way to avoid this tendency is to change the learning rate during the network training process. “Learning rate” refers to the rate of change of the neural network weights during optimization. Training of the neural network is terminated when a predetermined maximum number of training cycles have been completed. Selection of the maximum number is a trial-and-error process in which the number may be changed if the performance of the neural network during initial training falls short of expectations.

An *a priori* selection of ANN hyperparameters such as network topology, training algorithm, and network size is usually made based on experience. After training, the final sets of weights and biases trained by the network can be used for prediction purposes, and the corresponding ANN becomes a model of the input/output relation of the given problem. Because the ANN is to be trained to interpret the relationship between input and output data, the data used for training must be sufficient to capture the dynamics of the process being modeled. Section 5.2.1 discusses a simple example of classification using ANN.

5.3.1. An example of ANN application

Artificial neural networks form the base of deep learning, a subfield of machine learning where the algorithms are inspired by the structure of the human brain. Neural networks take in data, train themselves to recognize the patterns in the data, and then predict the output for a new set of similar unknown data. The following example briefly illustrates the process of training a simple ANN.

This example shows the process for constructing an ANN that differentiates between a square, circle and triangle. This is a common classroom example that will be familiar to readers who have studied machine learning. Figure 5.2 shows the process of building this network. Neural networks are made up of layers of neurons. These neurons are the core processing units of the network. Three kinds of layers form the structure of the network. The input layer, the output layer, and some number of hidden layers in which most of the computations required by the network are performed. The blue disk in the left-hand side of Fig. 5.2 is an input dataset composed of $28\text{-by-}28 = 784$ pixels. A different pixel is fed as an input to each neuron of the first layer. Neurons of one layer are connected to neurons of the next layer through channels. Each of these channels is assigned a numerical value known as a weight. The inputs are multiplied by the corresponding weights and their sum is sent as an input to the neurons in the first hidden layer. Each of these neurons is associated with a numerical value called the *bias*, which is added to the input sum. This sum is then passed through a function called the *activation function*. The activation function is used to introduce nonlinearity into the network. Then, the neurons in the first hidden layer transmit data to the neurons of the next layer over the channels in a similar manner. In this way the data are propagated through the network. This is called forward propagation. In the output layer the neurons with the highest value determine the output. The values are basically a probability. For example, in Fig. 5.2 the neuron associated with “square” has the highest probability. Hence, that is the output predicted by the neural network. Of course, it is obvious that the neural network has made a wrong prediction. But how does the network figure this out? Note that the network is yet to be trained. During the training process, along with the input, the network also has the output of the training data fed to it. The predicted output is compared with the target output to realize the error in prediction. The magnitude of the error indicates the degree of the error of the network and the sign indicates if the predicted values are higher or lower than expected. The arrows on the right-hand side of Fig. 5.2 give an indication of the

direction and magnitude of change to reduce the error. This information is then transferred backward through the network. This is known as *back propagation*. Based on this information the weights are adjusted using an optimization method. For example, the gradient descent method is a process that occurs in back propagation where the values of weights are updated using a *learning rate*. This cycle of forward propagation and back propagation is iteratively performed with multiple inputs. This process continues until the weights are assigned such that the network can predict the input shapes correctly in most of the cases. This brings the training process of the ANN to an end.

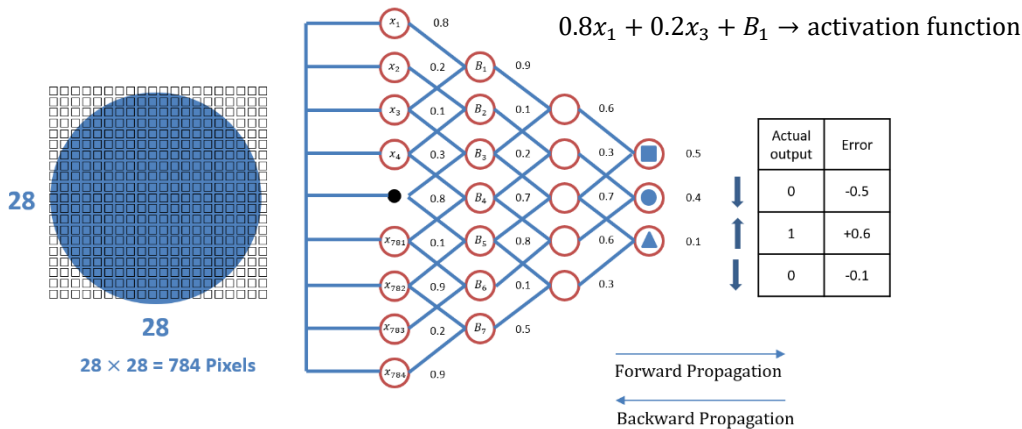


Figure 5.2. Training process of a classification problem.

The final two chapters of this dissertation describe original applications by the author of ANNs to problems in radiation heat transfer and applied optics.

Chapter 6:

Artificial Neural Networks in Radiation Heat Transfer Analysis

As developed elsewhere in this dissertation, in the Monte Carlo ray-trace (MCRT) method millions of rays are emitted and traced throughout an enclosure following the laws of geometrical optics. Each ray represents the path of a discrete quantum of energy emitted from surface element i and eventually absorbed by surface element j . The distribution of rays absorbed by the n surface elements making up the enclosure is interpreted in terms of a radiation distribution factor matrix whose elements represent the probability that energy emitted by element i will be absorbed by element j . Once obtained, the distribution factor matrix may be used to compute the net heat flux distribution on the walls of an enclosure corresponding to a specified surface temperature distribution. As already noted in previous chapters, it is computationally very expensive to obtain high accuracy in the heat transfer

calculation when high spatial resolution is required. This is especially true if a manifold of emissivities is to be considered in a parametric study in which each value of surface emissivity requires a new ray-trace to determine the corresponding distribution factor matrix. Artificial neural networks (ANNs) offer an alternative approach whose computational cost is greatly inferior to that of the traditional MCRT method. Significant computational efficiency is realized by eliminating the need to perform a new ray-trace for each value of emissivity. This chapter introduces and demonstrates through case studies estimation of radiation distribution factor matrices using ANNs and their subsequent use in radiation heat transfer calculations. This chapter is based on a peer-reviewed article by the author published in the **Journal of Heat Transfer** entitled “Artificial neural networks in radiation heat transfer analysis” [81].

6.1. Motivation

A widely lamented disadvantage of the MCRT method is the excessive computational cost associated with achieving high accuracy when fine spatial resolution is required. The fact that rays are mutually independent entities permits massive parallelization, with a proportionate reduction in processor time; however, associated cost, power, volume, and weight penalties exclude massive parallelization in applications where real-time results are required for data interpretation and decision-making on board autonomous space probes [63] and fire-and-forget weapons [64]. The alternative to a slow or computationally ponderous high-fidelity model (HFM) in such applications would be a reduced-order model (ROM) that provides comparable accuracy and spatial resolution but in real time and with significantly reduced hardware requirements [65]. This chapter describes such an alternative.

As previously stated, in the MCRT method, when the number of surface elements n is large and high accuracy is required, an exceedingly large number of rays must be traced. Furthermore, because D_{ij} depends on the emissivity ε_i , computational

costs can become excessive for optimization studies in which ε_i is a parameter. This motivates the search for a computationally less intensive approach. In this chapter, the computationally intensive Monte Carlo ray-trace (MCRT) method is used to compute the radiation distribution factors among the surface elements of a two-dimensional diffuse gray enclosure for a range of surface emissivity. Then a back-propagation algorithm is used to train an ANN based on these limited results. The ability of the much faster artificial neural network to accurately predict the distribution factor matrices corresponding to values of emissivity not used in the training cases is then evaluated. Various network configurations are investigated in a search for the optimal network. Once introduced, the method is then extended to increasingly complex problems.

6.2. The ANN as the alternative approach

As a demonstration of the approach advanced here, we consider three case studies of increasing complexity. All three cases involve radiant exchange within an enclosure consisting of gray diffuse surfaces in the absence of a participating medium; that is, radiant exchange is governed by Eqs. (3-1) through (3-3). However, once the distribution factors have been computed using the MCRT method, the ANN approach advanced here is expected to work equally well in the presence of a participating medium and with directional spectral surface models. The Monte Carlo ray-trace method described before is used to generate the training and test data needed to create and validate the ANN.

6.2.1. Case Study 1: A long box channel with uniform emissivity.

Figure 6.1 represents a long square-cross-section box channel having uniform wall emissivity and prescribed wall temperatures. The walls have been subdivided into 40 equal-area segments in anticipation of an MCRT analysis. The corresponding ANN will have a single input node representing the emissivity ε , and 1600 output

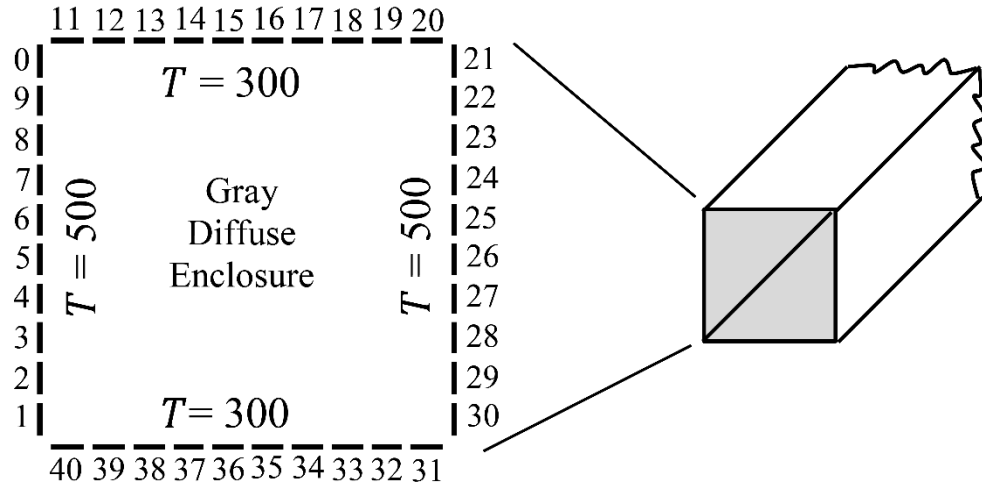


Figure 6.1. The long square-cross-section duct having gray diffuse walls considered in Case Studies 1 and 2 (dashes represent individually numbered wall surface elements shown separated by non-existent gaps for clarity).

nodes representing the 1600 elements of the 40-by-40 radiation distribution factor matrix.

In the current effort, we have used the application described in [67] to compute the distribution factors for the long square-cross-section duct illustrated in Fig. 6.1. The duct walls are maintained at uniform temperatures of 300 and 500 K as shown in the figure, and the corresponding net heat flux distribution on the walls is sought. The duct has been subdivided into $n = 40$ longitudinal surface elements, and one hundred numerical experiments were carried out covering the emissivity range $0.01 \leq \varepsilon \leq 1$. For each value of emissivity, two million rays were traced per surface element to obtain estimates of the corresponding distribution factor matrices D_{ij} , where $1 \leq i \leq 40$ and $1 \leq j \leq 40$. The resulting dataset was then randomly divided into training and test datasets. The training dataset used to regulate the weights on the ANN contained only 10 percent of the available data. The test dataset, consisting of the remaining 90 percent of the data, was used to evaluate the predictive ability of the ANN. While it is generally recognized that it is more common to use the majority of the available data for training and a minority

for testing, the ratio used here was found to give excellent results across the test data.

An Adam optimization algorithm is used. Mean-Squared Error (MSE) is used as the objective loss function for the ANN optimization. The learning rate was set to 0.0002. The maximum number of training iterations was set to 25000. The relative error of every predicted output is defined by

$$RE_{ij} = \frac{|D_{ij}^{True} - D_{ij}^{Pred}|}{D_{ij}^{True}}, \quad (6 - 1)$$

where D_{ij}^{Pred} is the predicted result (that is, the output of the ANN) and D_{ij}^{True} is the result from the Monte Carlo ray-trace (that is, the target output). During the neural network training process, performance was evaluated by calculating the mean value of the relative error,

$$MRE = \frac{1}{n^2} \sum_{i=1}^n \sum_{j=1}^n RE_{ij}. \quad (6 - 2)$$

Reciprocity and conservation of energy are two important restrictions imposed on the radiation distribution factor [3]. To ensure that these two restrictions are reflected in the predicted result, values of mean reciprocity and mean summation, defined

$$MR = \frac{1}{n^2} \sum_{i=1}^n \sum_{j=1}^n (\varepsilon_i A_i D_{ij}^{Pred} - \varepsilon_j A_j D_{ji}^{Pred}) \quad (6 - 3)$$

and

$$MS = \frac{1}{n^2} \sum_{i=1}^n \sum_{j=1}^n D_{ij}^{Pred}, \quad (6 - 4)$$

are computed. For a good prediction, MR should be near zero and MS should be near unity. The relative difference between the calculated net heat flux recovered from the predicted and true radiation distribution factor matrix,

$$MFD = \frac{1}{n} \sum_{i=1}^n \frac{q_i^{True} - q_i^{Pred}}{q_i^{True}}, \quad (6 - 5)$$

is also evaluated.

Generalization is a term used to describe the ability of an ANN to provide accurate output results when input data that have not been used for training are introduced into the trained network. Generalization is an essential property of any ANN. The network topology and size, as determined by the number of hidden layers and the number of hidden nodes, will affect the predicted performance. The performance of the trained network is evaluated by comparing its predicted results with data set aside for testing. In the current study, in order to facilitate the search for a configuration producing relatively good prediction, the ten different ANN configurations listed in Table 6.1 were considered.

Table. 6.1. Comparison of errors associated with various ANN configurations for Case Study 1.

ANN Configuration	Train Error				Test Error			
	Mean MRE (%)	Mean MR	Mean MS	Mean MFD (%)	Mean MRE (%)	Mean MR	Mean MS	Mean MFD (%)
1-5-1600	2.498	9.3e-5	1.0000	0.1921	5.399	7.3e-5	0.9999	0.1923
1-10-1600	2.531	8.3e-5	1.0000	0.1826	15.405	5.6e-4	1.0011	0.4651
1-20-1600	1.944	4.0e-5	1.0000	0.1369	4.716	4.0e-5	1.0000	0.1738
1-50-1600	0.375	6.6e-5	1.0000	0.0487	9.035	4.3e-4	1.0003	0.3110
1-5-5-1600	2.524	1.0e-5	1.0000	0.1752	5.445	1.0e-5	1.0000	0.1809
1-5-10-1600	2.526	1.5e-6	1.0000	0.1749	9.484	2.4e-4	0.9991	0.3634
1-10-20-1600	0.508	5.5e-5	1.0000	0.0763	2.863	7.6e-5	1.0000	0.1196
1-20-20-1600	0.707	5.3e-5	1.0000	0.0693	1.831	5.8e-5	0.9999	0.0951
1-50-50-1600	0.0264	1.2e-5	1.0000	0.0481	4.628	1.3e-4	1.0008	0.1631

Note that in Table 6.1, mean MR and mean MS are averaged over all the 10 training datasets and 90 test datasets, with different random weight initialization for each input. Both quantities are important for an assessment of the relative success of the

ANN analysis. We can see from inspection of the table that almost any configuration produces adequate results; however, some of them result in poor generalization. For example, the 1-10-1600 configuration produces a mean *MRE* error of about 15 percent for the test data despite the low error of 2.5 percent for the training data. All of the configurations yield the required reciprocity and conservation of energy properties of radiation distribution factors. For the three-layer ANN, when the number of hidden nodes is increased from 5 to 10, improvements in mean *MRE* and mean *MFD* are insignificant, indicating that increasing the number of nodes does not necessarily lead to better performance. For selecting the best configuration, the mean *MFD* for the test data in conjunction with the mean *MRE* for the training and test data are both taken into consideration, leading to selection of the 1-20-20-1600 configuration in the current example.

$$i = 1, 2, 3, \dots$$

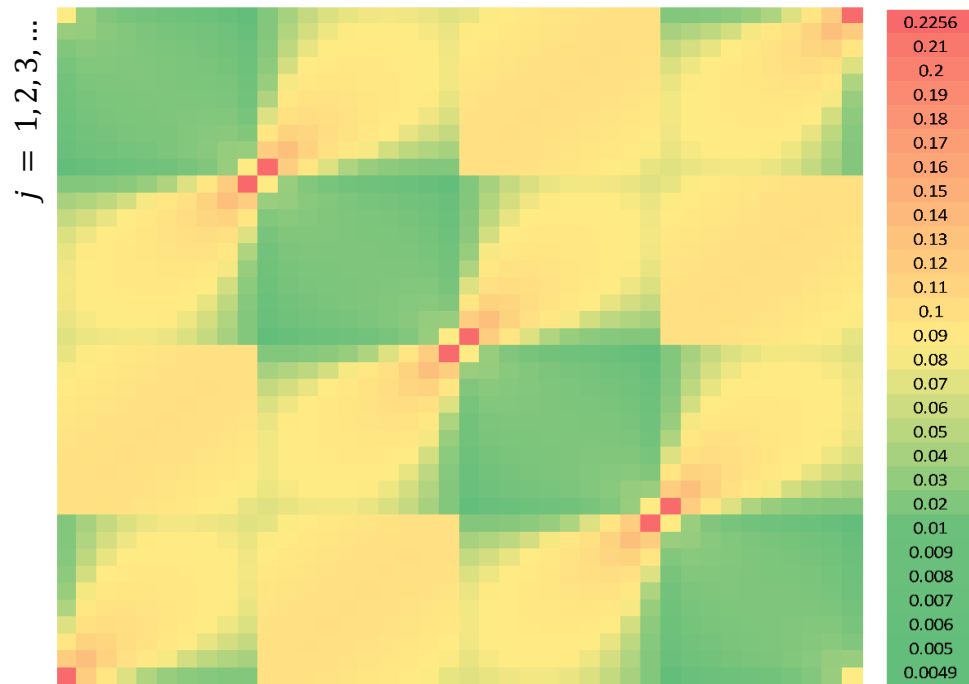


Figure 6.2. Radiation distribution factor matrix produced by the ANN approach for a sample of the test data corresponding to $\varepsilon = 0.75$ (Case Study 1).

The predicted radiation distribution factor matrix for a sample of the test data corresponding to $\varepsilon = 0.75$ is represented in Fig. 6.2. The printed values of D_{ij} are too small to read in the image, but the color shading, for which bright red indicates

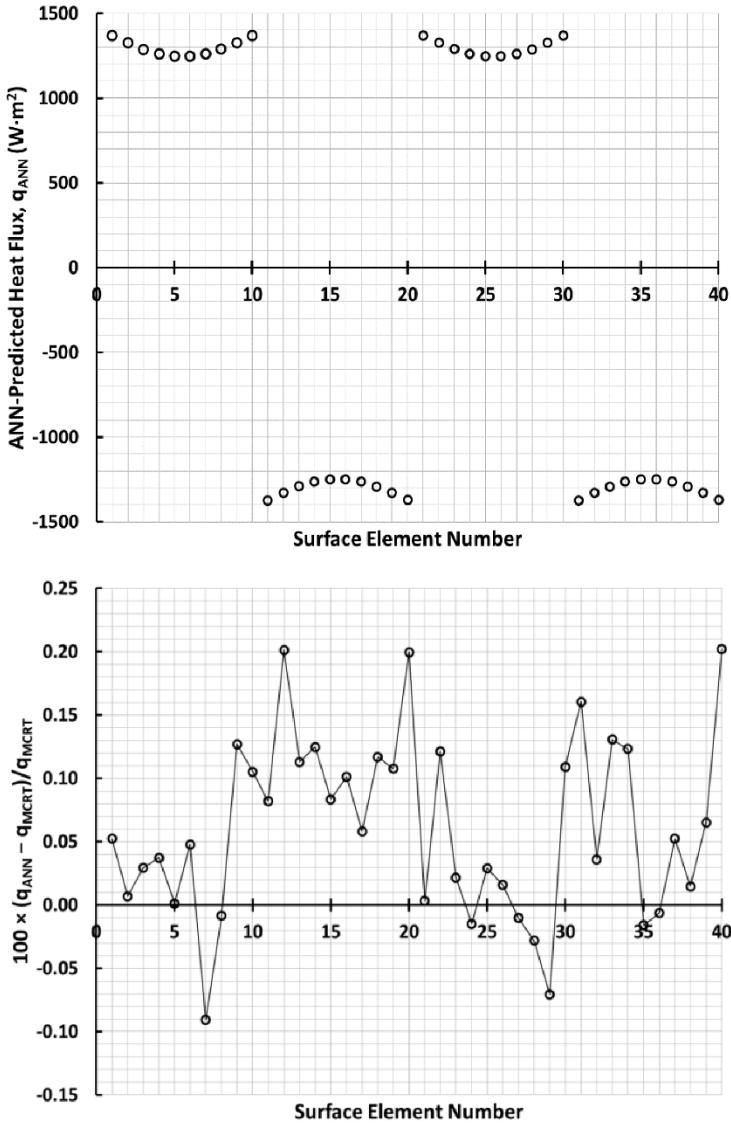


Figure 6.3. Comparison of the MCRT-based and ANN-based heat flux predictions (Case Study 1). The upper graph verifies the expected symmetry and the lower graph shows the percentage error between ANN and MCRT.

the maximum value ($D_{1,40} = D_{40,1} = D_{10,11} = D_{11,10} = D_{20,21} = D_{21,20} = D_{30,31} = D_{31,30} \approx 0.2256$) and dark green represents the minimum value ($D_{1,10} = D_{10,1} = D_{11,20} = D_{20,11} = D_{21,30} = D_{30,21} = D_{31,40} = D_{40,31} \approx 0.0049$), very clearly reveals the expected symmetry in the matrix.

Finally, Fig. 6.3 compares the MCRT-based and ANN-based net heat flux distributions on the four surfaces of the enclosure depicted in Fig. 6.1 corresponding to the same ANN test case whose distribution factor matrix is shown in Fig. 6.2. The expected symmetry in the net heat flux distribution is evident, and excellent agreement is exhibited between the two approaches, with the relative difference between them typically on the order of 0.1 percent. It is clear that the ANN approach is a potentially powerful alternative to costly ray-tracing in radiation heat transfer analysis when a parametric study of surface emissivity is involved. For example, once the investment in creating and training the ANN model has been made, the time required to create the data in Fig. 6.2 is measured in seconds as opposed to hours on a typical desktop computer using the MCRT method.

6.2.2. Case Study 2: A long box channel with non-uniform emissivity.

In many radiation heat transfer applications of practical interest, surface emissivities vary with both position and instance due to the strong heterogeneity of surface properties associated with topography, surface chemistry, contamination, and aging. Here “instance” refers both to changes that take place over time for a given enclosure, and to differences from one enclosure to the next associated with manufacturing tolerances. In practice it is unlikely that the surfaces comprising any two enclosures will have exactly the same emissivities. Methods for monitoring the temporal variations of emissivity are discussed elsewhere [98, 99]. Here, as a practical demonstration, we allow the surface emissivity of the four walls of the enclosure geometry shown in Fig. 6.1 to vary from one instance to the next. It is assumed for each instance that each wall has a different but uniform emissivity.

Therefore, the emissivity of the enclosure for any instance is represented as a vector whose four elements are the emissivities of the four walls. In order to use the ANN to predict the evolution of the radiation distribution factor matrix either with time or from one enclosure to the next, training data are produced using the MCRT method with a 5-percent random perturbation of the emissivity of each wall about a mean value. In other words, in each instance the emissivities of the four walls are randomly perturbed according to

$$\varepsilon_i = \varepsilon_d(1 \pm 0.05 \times rand), \quad i = 1,2,3,4, \quad (6 - 6)$$

where ε_d is the design wall emissivity and *rand* is a uniformly distributed random number between zero and unity. In this case, four ANN input nodes are used corresponding to the four emissivities ε_i , while the 1600 output nodes still correspond to the 1600 elements of the 40-by-40 radiation distribution factor matrix. Again, one hundred numerical experiments were carried out to produce data. Twenty percent of the data was used to train the neural network. The remaining 80 percent of the data was used as the test data to validate the predictive power of the network.

Table 6.2. Errors associated with 4-100-100-1600 ANN configuration for Case Study 2.

Train Error				Test Error			
Mean MRE (%)	Mean MR	Mean MS	Mean MFD (%)	Mean MRE (%)	Mean MR	Mean MS	Mean MFD (%)
1.119	1.5e-4	1.0004	0.5493	34.867	3.2e-4	1.0006	0.7489

Table 6.2 shows the ANN results for the 4-100-100-1600 configuration selected for the case under consideration. The results are not as satisfactory as in the case with only one emissivity as the input feature. We can see that the mean test error associated with predicting the radiation distribution factors is quite high; however, they still allow accurate prediction of the net heat fluxes. This is partially because

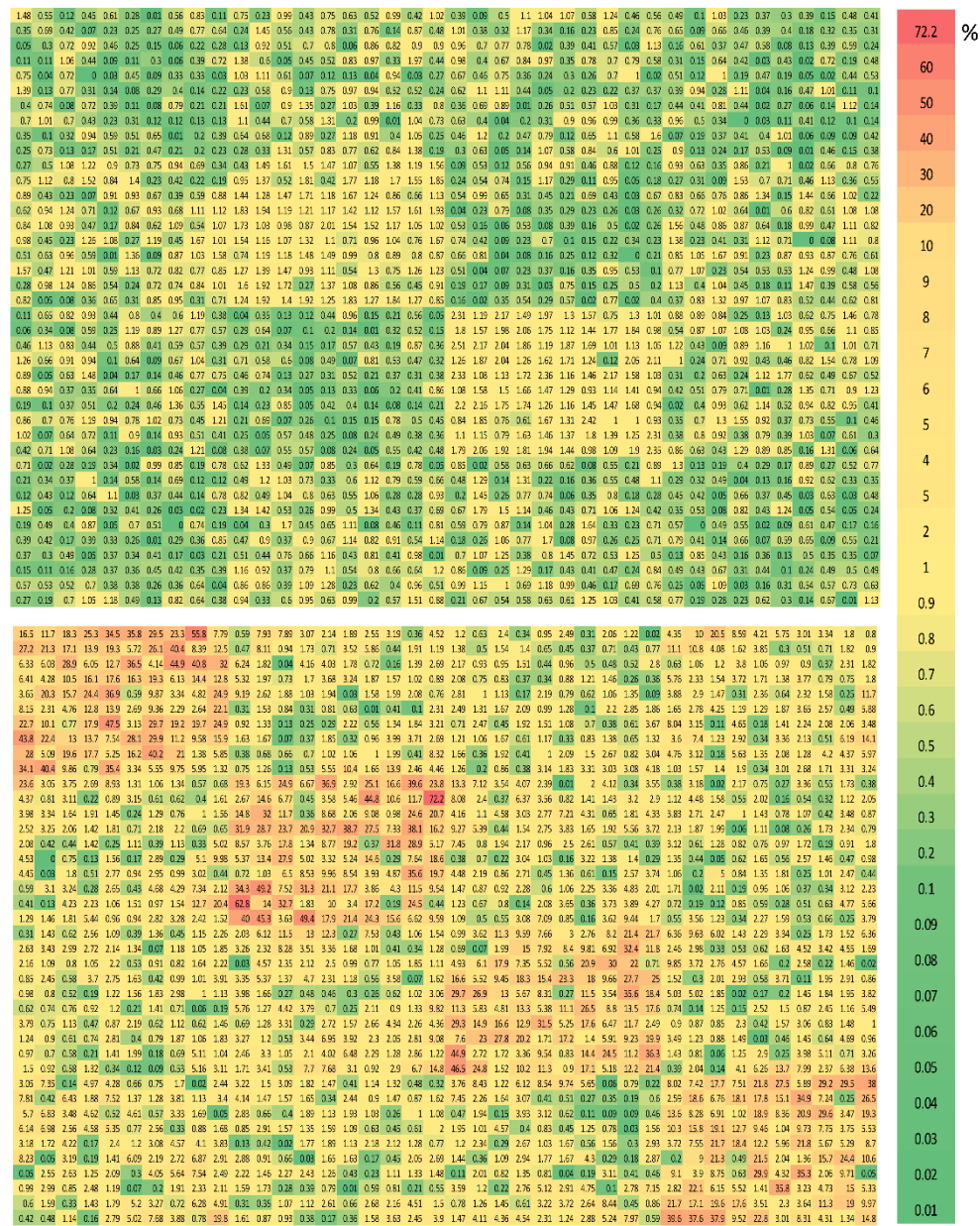


Figure 6.4. Comparison of the percent absolute relative error in the radiation distribution factors between a relatively “good” (top) and a relatively “bad” (bottom) distribution factor matrix predicted using the ANN (Case Study 2).

solution of radiation problems is mathematically an integration process, as opposed to the solution of conduction problems using differential equations. Integration

tends to smooth out errors, whereas differentiation tends to amplify them. Also, a mean MR of $3.2e-4$ and a mean MS of 1.0006 shows that the model is yielding the required reciprocity and conservation of energy. The relatively high mean MRE error in the test data is due to a small number of high errors in relatively few pixels for a small number of samples, as foreshadowed on page 30 in the discussion of Eq. (3-12).

Figure 6.4 compares the percent absolute relative error in the radiation distribution factors, defined

$$\frac{|D_{ij}^{MCRT} - D_{ij}^{ANN}|}{D_{ij}^{MCRT}} \times 100\%,$$

for relatively “good” and relatively “bad” distribution factor matrix predictions using the ANN. Both results are drawn from the test dataset used in constructing Table 6.2. The red-tinted cells in the bottom (bad) matrix of Fig. 6.4, which correspond to errors exceeding two percent, reveal that some elements of the radiation distribution factor matrix are predicted with relatively poor accuracy including one element for which the error is 72 percent. However, these large relative errors correspond to small values of D_{ij} as is made clear by comparison with Fig. 6.2. This means that the relative errors are disproportionately amplified due to division by small numbers (see p. 30). Although this produces a large value of Mean MRE for the test dataset error in Table 6.2, the small values of these distribution factors themselves minimize their effect on the heat flux analysis, thereby yielding a small value of Mean MFD.

Figure 6.5(a) reveals excellent agreement between the net heat fluxes predicted using the ANN-based and MCRT-based distribution factor matrices corresponding to the upper panel of Fig. 6.4, and Fig. 6.5(b) confirms that the local net heat flux errors are generally less than 1.5 percent in this case. Figure 6.6(a) also reveals good agreement between the ANN-based and MCRT-based net heat flux distributions

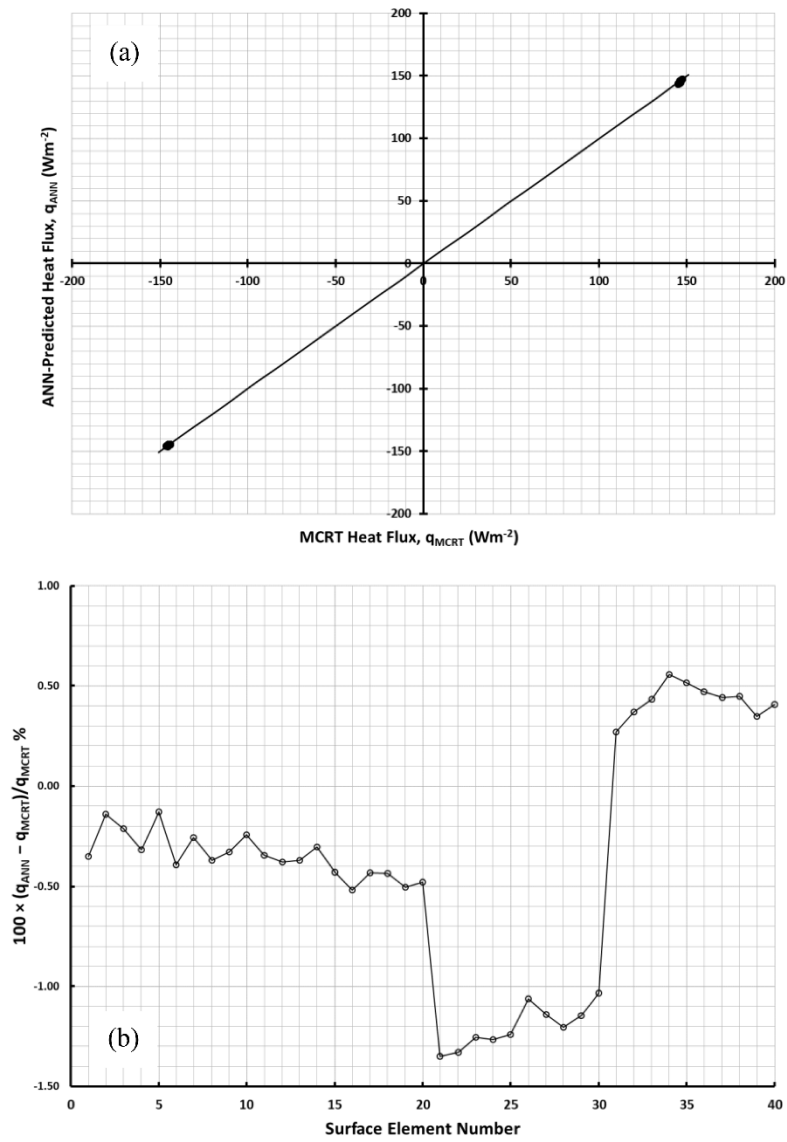


Figure 6.5. (a) The ANN-based net heat flux distribution plotted against the MCRT-based distribution, and (b) the local percentage differences between the two distributions corresponding to the “good” test dataset result of Case Study 2.

even though the distribution factor matrix prediction is relatively bad, and the local net heat flux errors shown in Fig. 6.6(b), though somewhat larger than those in Fig. 6.5(b), are generally well under two percent in this case. We may conclude that the

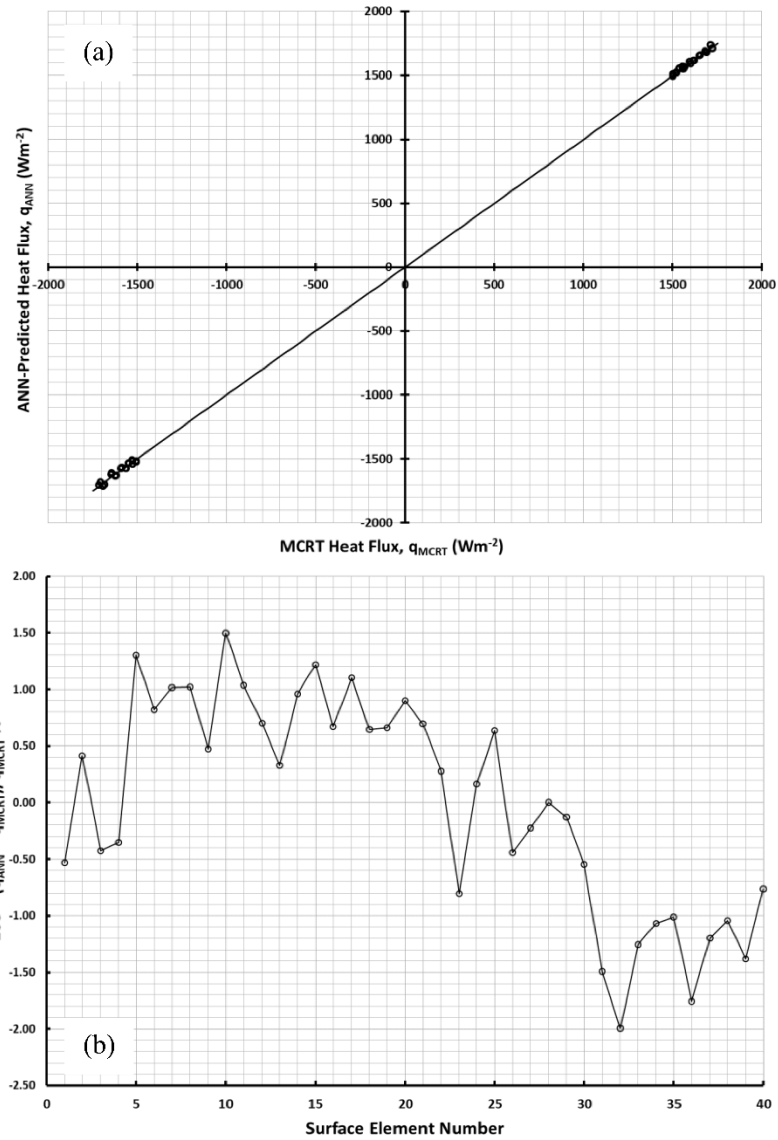


Figure 6.6. (a) The ANN-based net heat flux distribution plotted against the MCRT-based distribution, and (b) the local percentage differences between the two distributions corresponding to the “bad” test dataset result of Case Study 2.

ANN approach works well for the case of a non-uniform emissivity distribution. Furthermore, while minimizing Mean MRE is a valid strategy for defining the ANN

hyperparameters, its value should not be interpreted as a measure of the ability of the ANN-produced distribution factor matrix to predict local net heat flux.

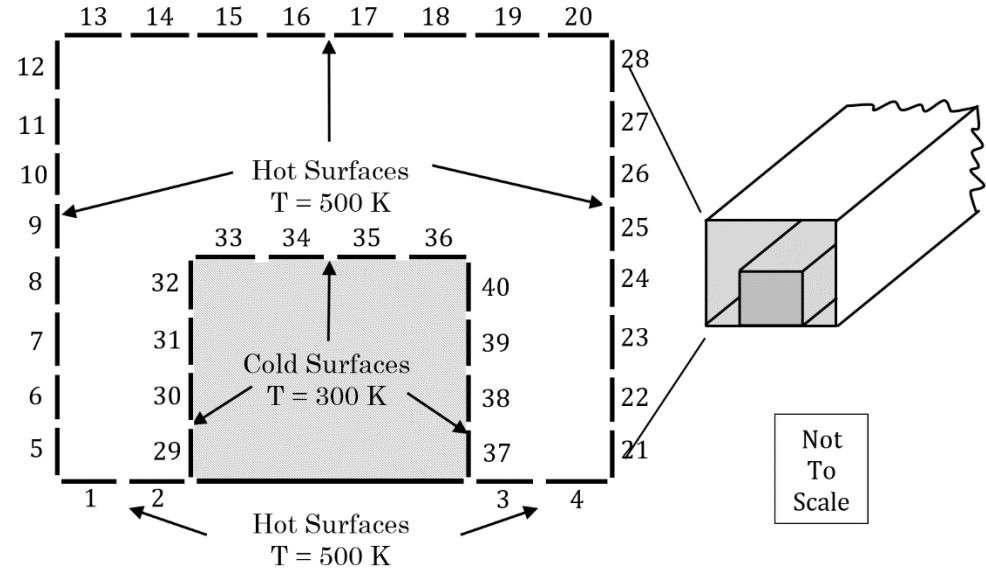


Figure 6.7. The long two-dimensional industrial oven having gray diffuse walls (dashes represent individually numbered wall surface elements shown separated by non-existent gaps for clarity) and an interior obstruction considered in Case Study 3.

6.2.3. Case Study 3: A long box channel with an interior obstruction.

In Cases 1 and 2 we considered a geometry in which all wall segments have a direct view of all other wall segments. We now return to the consideration of the more complex geometry involving an interior obstruction which partially blocks the direct view of some surfaces from other surfaces. In such cases the MCRT method is the only practical approach for analyzing the radiation heat transfer. Howell was among the first to predict the emerging dominance of the Monte Carlo method for treating radiative heat transfer [1] in such cases. Figure 6.7 represents a benchmark two-dimensional enclosure that has been used in previous radiation heat transfer studies [40, 42, 43, 47, 56-58, 60, 61]. In the current study we have divided it into 40 equal-area longitudinal surface elements.

The flexibility of the Monte Carlo method to accommodate complex geometries comes at a significant computational cost when the code must be executed many times in the context of a parametric study; e.g., when searching for an optimum value of emissivity for a given application. This cost can be significantly reduced by replacing the high-fidelity MCRT model with a reduced-order ANN model of comparable accuracy in the search algorithm.

Once again assuming that the emissivity is uniform across all the walls of the enclosure, the ANN has only a single input node, corresponding to the emissivity, while 1600 output nodes are required to represent the 1600 elements of the radiation distribution factor matrix. One hundred numerical experiments were carried out to produce training and test datasets and, as before, ten percent of the data were used to train the neural network, with the remaining 90 percent used as the test data to validate the predictive power and generality of the ANN.

Table 6.3 shows the ANN results for the 1-100-100-1600 configuration selected for this case study. We again see that the MRE error for the test dataset, about 16.6 percent in this case, is a poor measure of the ability of the distribution factors to predict the net heat flux distribution. The ANN model yields the required reciprocity and obeys conservation of energy to a high degree of accuracy.

Table 6.3. Errors associated with 1-100-100-1600 ANN configuration for Case Study 3.

Train Error				Test Error			
Mean MRE (%)	Mean MR	Mean MS	Mean MFD (%)	Mean MRE (%)	Mean MR	Mean MS	Mean MFD (%)
1.784	6.0e-4	1.0000	0.0969	16.627	2.4e-4	1.0004	0.3284

Figure 6.8(a) compares the MCRT-based and ANN-based net heat flux distributions on the surfaces of the enclosure depicted in Fig. 6.7 for a uniform emissivity of 0.75, and Fig. 6.8(b) shows the relative difference between the values calculated for the net heat fluxes by the two methods. The accuracy—generally better than one percent—is quite acceptable.

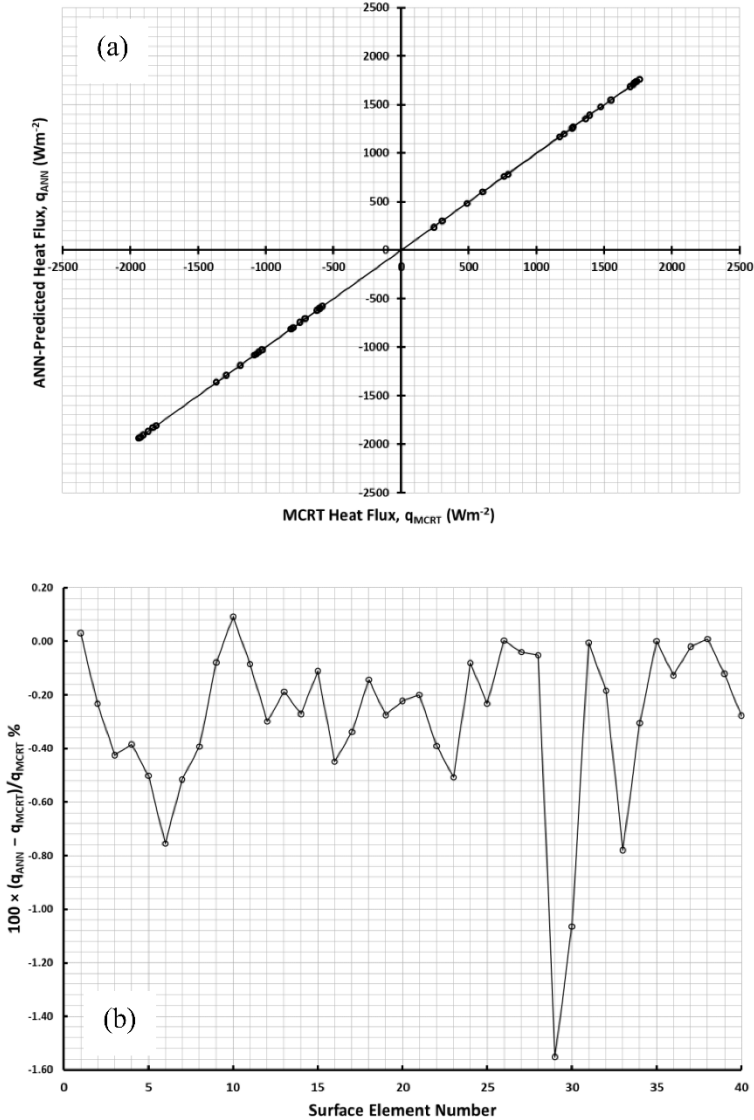


Figure 6.8. (a) The ANN-based net heat flux distribution plotted against the MCRT-based distribution, and (b) the local percentage differences between the two distributions (Case Study 3, $\varepsilon = 0.75$).

6.3. Conclusions and recommendations

Artificial neural networks (ANNs) are investigated as an alternative to ray-tracing in radiation heat transfer applications involving diffuse gray enclosures in the absence of a participating medium. Specifically, they are used to predict the radiation distribution factor matrix and corresponding net heat flux distribution on the walls of long box structures. In each case a feed-forward back-propagation algorithm is used to train and test the ANN. Net heat flux results obtained using the ANN approach are shown to agree well with those obtained using the standard Monte Carlo ray-trace method for the three cases studied: (1) uniform emissivities on all walls of a square-cross-section duct, (2) differing emissivities from wall to wall perturbed about a design value for the same unobstructed duct, and (3) a rectangular duct containing a rectangular obstruction with uniform emissivity on all walls. The author recommends the approach introduced here when a parametric study is required to determine the optimum value of emissivity for a given application. For example, the results for Case Study 2, obtained with much less computational effort than would have been required using the MCRT method alone, could be used in a quality-control scheme to determine the variability in the net wall heat flux corresponding to a five-percent manufacturing tolerance in wall emissivity. The ANN approach would be the same for the case of a non-diffuse, non-gray enclosure filled with a participating medium as for the case of a diffuse gray enclosure in the absence of a participating medium demonstrated in the current effort. This encourages the idea that the approach advanced here would be equally applicable—and even more useful—in these far more complex situations.

Chapter 7:

Numerical Focusing

Using an Artificial

Neural Network

Narrow field-of-view scanning thermistor bolometer radiometers have traditionally been used to monitor the earth's radiant energy budget from low Earth orbit (LEO). Such instruments use a combination of cross-path scanning and along-path spacecraft motion to obtain a patchwork of punctual observations which are ultimately assembled into a mosaic. Monitoring has also been achieved using non-scanning instruments operating in a push-broom mode in LOE and imagers operating in geostationary orbit [100]. The current contribution considers a fourth possibility, that of an imager operating in LEO. The system under consideration consists of a Ritchey-Chrétien telescope illuminating a plane two-dimensional microbolometer array. At large field angles, the focal length of the candidate instrument is field-angle dependent, resulting in a blurred image in the

readout plane. Presented in this chapter is a full-field focusing algorithm based on an artificial neural network (ANN). Absorbed power distributions on the microbolometer array produced by discretized scenes are simulated using a high-fidelity Monte Carlo ray-trace (MCRT) model of the imager. The resulting readout array/scene pairs are then used to train an ANN. We demonstrate that a properly trained ANN can be used to convert the readout power distribution into an accurate image of the corresponding discretized scene. This opens the possibility of using an ANN based on a high-fidelity imager model for numerical focusing of an actual imager. The emergence of the MCRT method has blurred the line between radiation heat transfer and applied optics. This chapter which is based on a peer-reviewed article by the author published in **Remote Sensing** entitled “Numerical focusing of a wide-field demonstrates the flexibility of the MCRT method”. [63], demonstrates the flexibility of the MCRT method.

7.1. Introduction

Traditional earth radiation budget (ERB) instruments such as those deployed on the Earth Radiation Budget Experiment (ERBE) [101] and on Clouds and the Earth’s Radiant Energy System (CERES) [102] and proposed for the ultimately deselected Radiation Budget Instrument (RBI) [103] consist of downward-looking telescopes in low Earth orbit (LOE) which scan back and forth across the orbital path, as illustrated in Fig. 7.1. While proven effective, such systems incur significant weight and power penalties and may be susceptible to eventual mechanical failure. Another approach to accomplishing the ERB mission is the Geostationary Earth Radiation Budget (GERB) instrument, which consists of a three-mirror imager illuminating a microbolometer focal-plane array (FPA) [104]. The ERB mission will also be assured by EarthCARE (Earth, Clouds, Aerosols, and Radiation Explorer), which includes a Broadband Radiometer (BBR) suite consisting of three sets of two-dimensional paraboloid single-mirror optics, each illuminating a

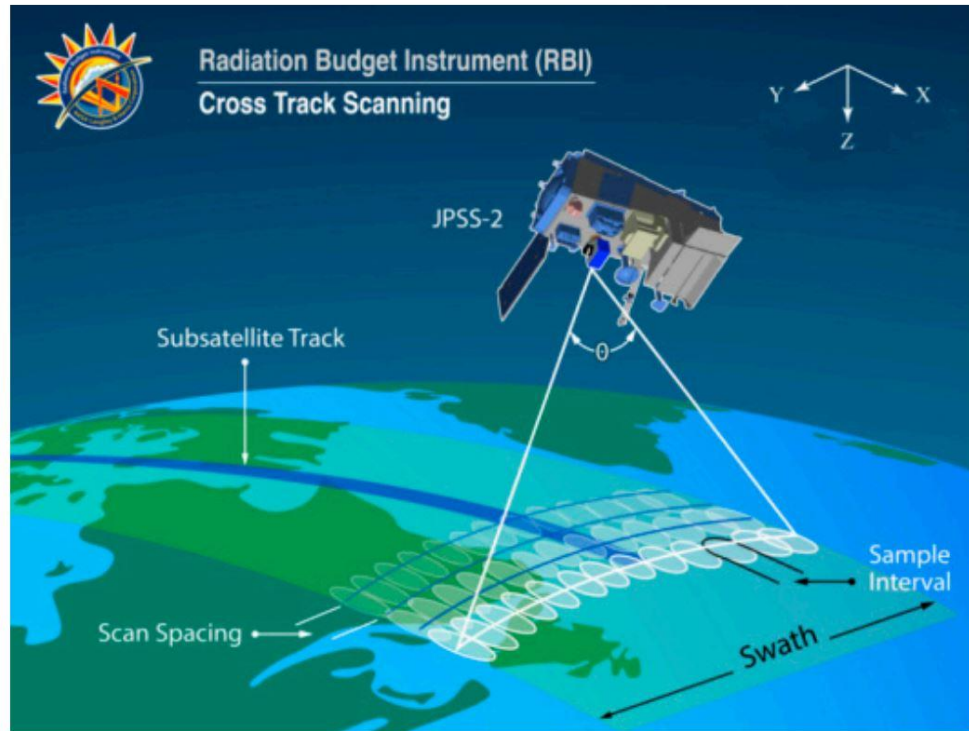


Figure 7.1. Radiation budget instrument (RBI) [100] scan pattern.

microbolometer linear array [100]. Both GERB and BBR rely on optical approaches to avoid scanning. In the case of GERB the field angle is limited by the extreme altitude of the instrument, which is parked in geostationary orbit. The narrow field angle significantly simplifies the optical design, and scanning is then achieved by the rotation of the Earth. The BBR suite on EarthCARE achieves optical simplification by push-broom operation and the use of a linear array; as in the case of scanning instruments, light gathering is limited to the width of a single pixel. Here we consider a novel approach in which a wide-field-angle imager is placed in LOE and the resulting astigmatism is corrected algorithmically.

Figure 7.2 is a CERES science product showing the monthly average global outgoing longwave radiation for May 2001 [105]. The CERES longwave channel is filtered to be sensitive only to Earth-emitted radiation. The false-color map of monthly average band-limited flux (Wm^{-2}) is relatively free of sharp edges and

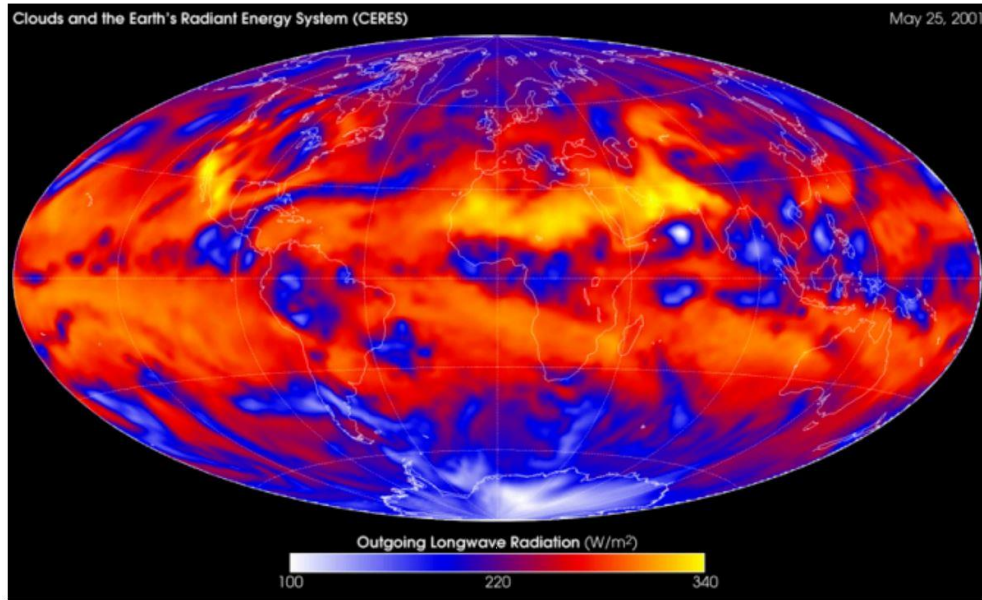


Figure 7.2. Global outgoing longwave radiation as mapped using data from the Clouds and the Earth's Radiant Energy System (CERES) instrument (May, 2001 [105]).

finely resolved features. This is equally true of the CERES shortwave channel, which is filtered to be sensitive only to Earth-reflected solar radiation. The fact that broadband scenes are effectively monochromatic and vary gradually within a given swath significantly limits their spatial frequency content. A requirement of any next-generation staring imager is that it produces data products capable of mimicking those obtained from legacy scanners. In other words, images obtained must be relatable to the scanner footprints shown in Fig. 7.1. Consequently, it is appropriate to represent Earth scenes as consisting of a relatively modest number of directional beams.

Figure 7.3 represents a generic wide-field-angle ERB imager consisting of an entrance aperture, baffled imaging optics, and a plane two-dimensional readout array. Two beams of radiation emanating from point sources at infinity are shown flooding the entrance aperture. Corresponding point-spread functions (PSFs) in

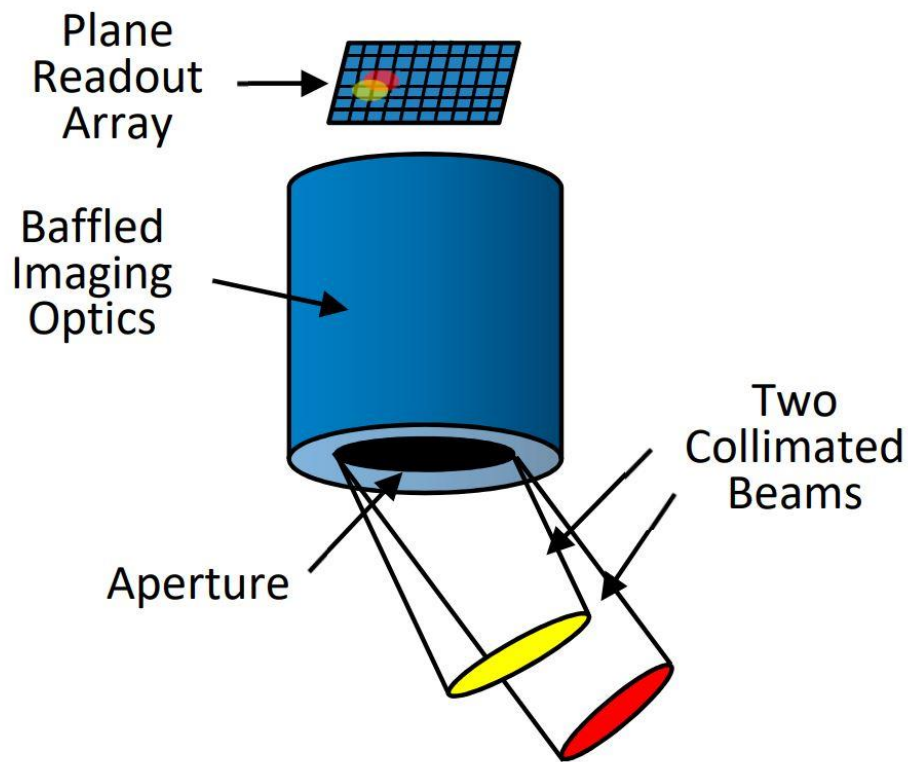


Figure 7.3. Schematic representation of a generic wide-field-angle earth radiation budget staring imager.

the readout plane indicate the distribution of the beam energy there. Depending on the design of the optical train, focus will generally be achieved on a curved rather than on a plane surface. This is especially true when two-mirror optical systems of the Cassegrain or Ritchey-Chrétien type are pushed to their wide-field-angle limits. While deemed achievable, technology permitting non-planar microbolometer readout arrays has not yet been demonstrated. Therefore, we limit our consideration here to plane readout arrays, in which case blurring is expected to vary with field angle across the array. The challenge then is to create an accurate and computationally efficient algorithm for recovering the original discretized scene from the blurred illumination pattern on the readout array.

7.2. Image deblurring

Following the formality of Pratt [106] the deblurring problem can be posed as

$$\begin{aligned} H f(x, y) &\equiv \int \int h(x - u, y - v) f(u, v) du dv = g_e(x, y) + n(x, y) \\ &\equiv g(x, y), \end{aligned} \quad (7 - 1)$$

where $f(x, y)$ is the deblurred image, $g_e(x, y)$ is the blurred image that would have been recorded in the absence of noise $n(x, y)$, $g(x, y)$ is the actual recorded image, h is a point-spread function (PSF), and H is an unknown matrix defined by the expression. In the discrete version of Eq. (7-1) the double integral is replaced by a double sum over a discretized two-dimensional space. Then elements of the matrix H_{ij} are sought such that

$$f_i = H_{-1}^{ij} g_j, \quad (7 - 2)$$

where the indices i and j represent ordered pixel numbers in a two-dimensional array. Then f_i is the deblurred intensity of pixel i and g_j is the recorded intensity of pixel j . It should be emphasized that in discretized two-dimensional space both the deblurred image f_i and the recorded image g_j are defined by the same number of pixels; that is, H_{ij} is a square matrix. The symbol H_{-1}^{ij} represents the inverse of the unknown matrix. While posed here as a problem in the space domain, practical implementation typically occurs in the frequency domain, in which case the Fourier transform dual of the PSF is the optical transfer function (OTF). Heuristically, deblurring involves deconvolution of either Eq. (7-1), or its frequency-domain dual. In the case of non-blind deblurring, when the PSF (or OTF) is uniform and known across the image, the Lucy-Richardson algorithm [107, 108] can be used to solve Eq. (7-1). When the PSF is unknown it can often be reasonably modeled, for example as a Gaussian distribution having an unknown mean and variance. In this case the problem is ill-posed but can still be solved if an independent criterion for “good focus” is available against which the success of the solution can be evaluated.

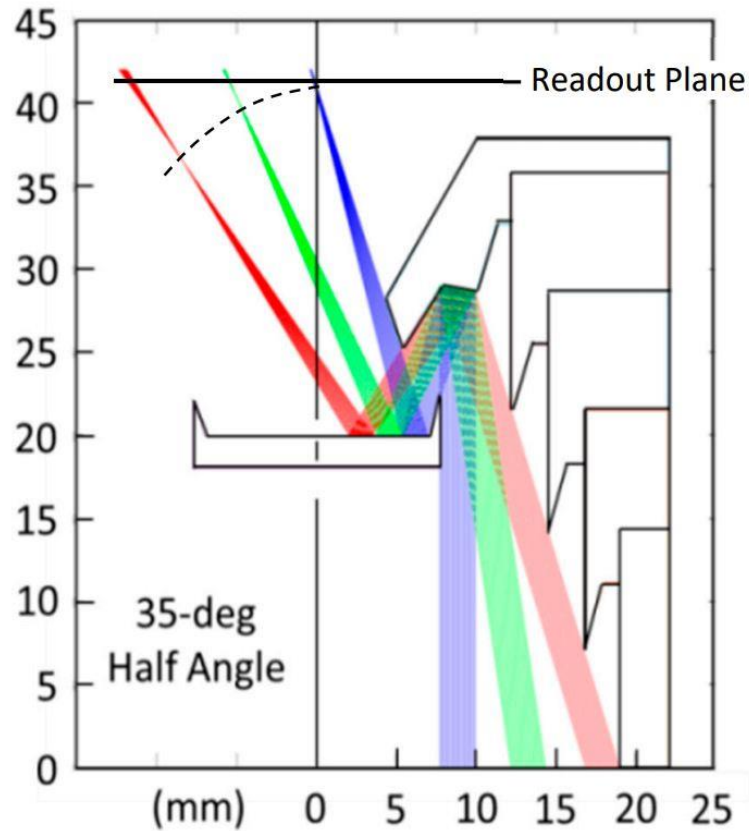


Figure 7.4. Cross-section of the wide-field-angle Ritchey-Chrétien telescope (RCT) which is the basis of the current investigation.

In such so-called blind deconvolution schemes a systemic search based on, for example, a genetic algorithm (GA) [109], can be conducted to identify the combination of deblurred images and uniform PSFs that best reproduces the recorded blurred image. Solutions obtained in this way are generally not unique but may still be useful. A viable alternative which assures stability and uniqueness is regularization [110]. Machine learning (ML) approaches to image deblurring have inevitably emerged, mostly in the context of improving PSF estimates [111-115].

Figure 7.4 is a scale drawing of a cross-section of a wide-field-angle Ritchey-Chrétien telescope (RCT) consisting of a field-limiting forward baffle, a baffled

hyperbolic primary mirror, a baffled hyperbolic secondary mirror, and a plane readout array. A high-fidelity Monte Carlo ray-trace (MCRT) model of this instrument forms the basis for the current investigation. Ashraf et al. [116] have previously reported a novel approach to scene recovery by this instrument. In their previous approach a mean scene direction was computed for the rays absorbed on a given pixel of the readout array during simulated observation of a blackbody calibration source. A pixel-by-pixel calibration curve was then established by computing the corresponding absorbed power distribution on the readout array. This approach was shown to work well for the limited amount of testing to which it has been subjected.

The technique presented in the current contribution is similar to one described in Ref. [117], with the important difference that the authors of the cited reference start with a discretized well-focused image to which they add known mathematical noise and blurring. This is in contrast to our approach in which:

- (1) The readout array power distribution, which is the input to the ANN model, is produced by introducing a randomly discretized scene to the high-fidelity MCRT optical model of the imaging system, and
- (2) The readout array does not have the same number of pixels as the output of the ANN model, which represents the recovered discretized scene.

Rather than recording a replicate of the scene, the readout array is required only to record sufficient information to recover the original scene. Thus, our method is fundamentally different from previous deblurring paradigms based on the solution of Eq. (7-1). Instead, an artificial neural network (ANN) is used to characterize the relationship between the illumination pattern on the readout array and the corresponding discretized scene that produced it. The MCRT-based high-fidelity model (HFM) of the imager is used to train the ANN by presenting it with a large number of pairs of readout array power distributions and corresponding discretized scene intensity distributions. Once trained, the ANN may then be used

to predict the discretized scene corresponding to any recorded readout array power distribution. The logic flow of the technique is illustrated in Fig. 7.5.

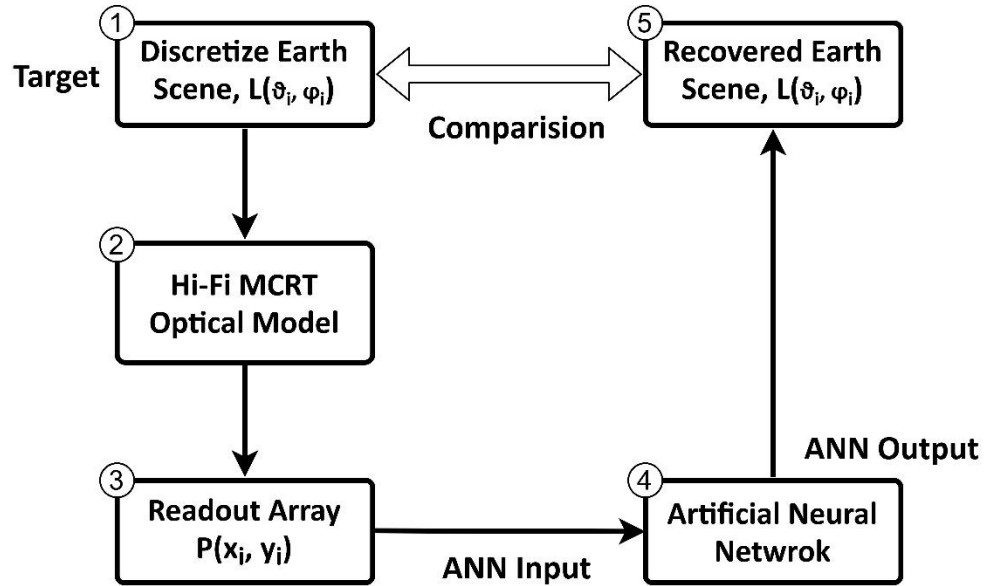


Figure 7.5. Numerical focusing logic block diagram.

Step 1. Creation of Scene/Readout array Pairs

Block 1 in Fig. 7.5 indicates a process in which scenes are synthesized as a collection of random-strength beams incident from a discrete set of directions. Each beam, representing light from a point source at infinity, consists of a large number of parallel rays that flood the entrance aperture of the high-fidelity Monte Carlo ray-trace imager model of the telescope shown in Fig. 7.4 and represented by Block 2 in Fig. 7.5. Details of the imager model are similar to those elaborated in Chapter 3 (pp. 85–94) of Ref. [3]. Block 3 records the output of the imager HFM on a plane two-dimensional 19×19 -pixel readout array. During Step 1, 2000 random-strength beams incident from 50 specified directions are input to the imager HFM, producing 2000 corresponding power distributions on the readout array.

Step 2. Training the Artificial Neural Network (ANN)

A random selection of 1950 of the 2000 readout array power distributions created in Step 1 and loaded into Block 3 are input one at a time into the artificial neural network represented by Block 4. For each of these readout array power distributions, the synaptic weights of the ANN are adjusted in an iterative process, described in Section 7.4, which minimizes the difference between the ANN output scene represented by Block 5 and the corresponding target scene in Block 1.

Step 3. Testing the Artificial Neural Network

The 50 readout array power distributions created in Step 1 that were not used to train the ANN in Step 2 are introduced sequentially into the trained ANN. Then the resulting output scene (Block 5) in each case is compared to the target scene (Block 1) used to create it. The pixel-by-pixel differences between corresponding ANN output and target scenes provide a measure of the success of the proposed numerical focusing scheme.

Step 4. Prediction of unknown scenes from recorded readout-array power distributions

Availability of a properly trained and tested ANN model of the imager renders further ray-tracing unnecessary. From this point forward, the trained ANN model can be reliably used to convert recorded readout array power distributions to corresponding discretized scenes by following the path Block 3→Block 4→Block 5. Alternatively, the operational instrument, once built, can be calibrated by introducing discrete beams from collimated sources incident from directions corresponding to the desired directional resolution. Preliminary versions of the ANN model can be used in the design phase of instrument development, while higher-order, more refined models can be used to yield scientifically accurate science data during on-orbit operation of the actual imager.

Details of the individual steps are provided in Section 7.3, Section 7.4 and Section 7.5.

7.3. Instrument model

The specific Ritchey-Chrétien telescope (RCT) which informs the current investigation is shown in Fig. 7.4. The three ray-traces shown indicate that beams entering at different field angles achieve focus on a curved surface (the dashed curve). Therefore, the PSF of a beam on the plane readout array will be increasingly misfocused with increasing incidence angle. While the results reported in the current investigation are specific to this particular optical system, the methodology used to obtain them is general and therefore applicable to virtually any optical system for which a high-fidelity performance model is available.

A Monte Carlo ray-trace is performed in which millions of rays are traced from each of 50 directions to form beams, each flooding the entrance aperture of the telescope shown in Fig. 7.4. Following Ashraf [118], the 50 directions are determined by first dividing an imaginary hemisphere surmounting the entrance aperture into equal-area sectors. Then the rays forming a given beam are constrained to pass parallel to a ray which passes normal to the centroid of one of the sectors. The rays are traced through the baffled telescope and eventually absorbed on a 361-pixel two-dimensional microbolometer array. Results of a ray-trace for a one-million-ray beam incident to the aperture at a zenith angle ϑ of 10.9 deg and an azimuth angle φ of 18.0 deg are shown in Fig. 7.6, and results for all 50 beams showing the distribution of absorbed power from each of the 50 directions on the 19-by-19-element array are given in Fig. 7.7. Each incident beam direction is assigned a number ranging from 1 to 50. Assigned beam numbers are indicated in red type. In Fig. 7.6 and Fig. 7.7, the red end of the color spectrum represents the largest number of rays absorbed by a pixel for a given direction, and the yellow end of the spectrum represents the smallest nonzero number of absorbed rays,

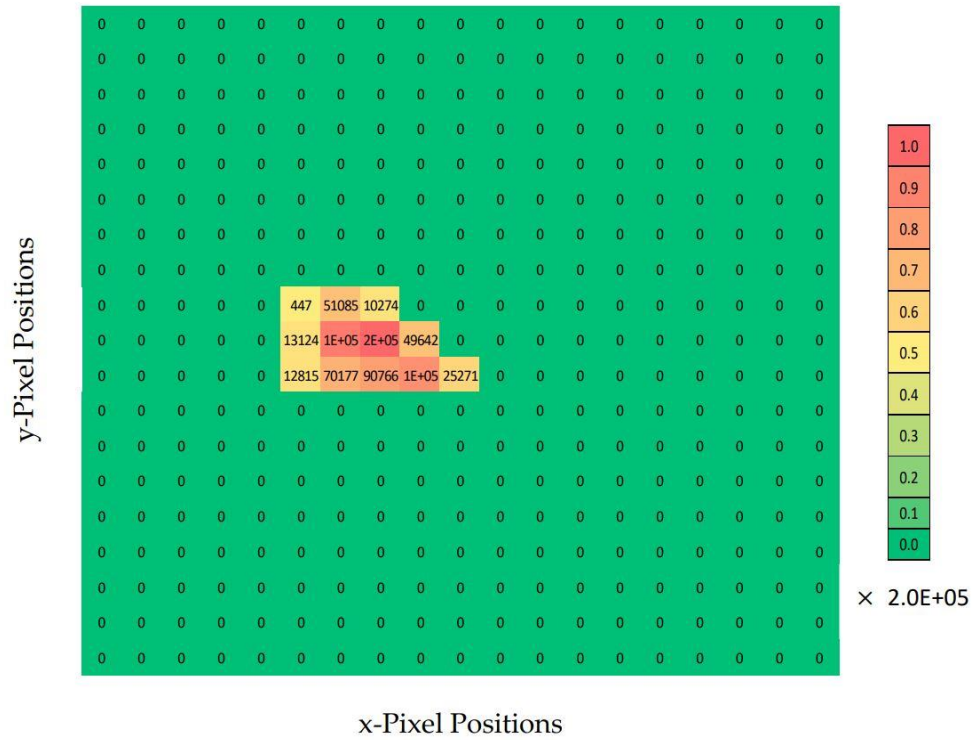


Figure 7.6. Distribution on the 19-by-19 microbolometer array of collimated rays forming Beam 1 in Figure 7.7.

with green indicating zero rays. Creation of the fifty “primitives” shown in Fig. 7.7 required about 250 min of machine time on a laptop PC.

It is clear from inspection of Fig. 7.6 that power from beams incident from a given direction is absorbed by several neighboring pixels. The distribution becomes increasingly distorted moving from $\vartheta = 10.9$ to $\vartheta = 33.1$ deg for a given value of φ . Also, the number of rays in the original beam that reach the readout plane decreases with zenith angle.

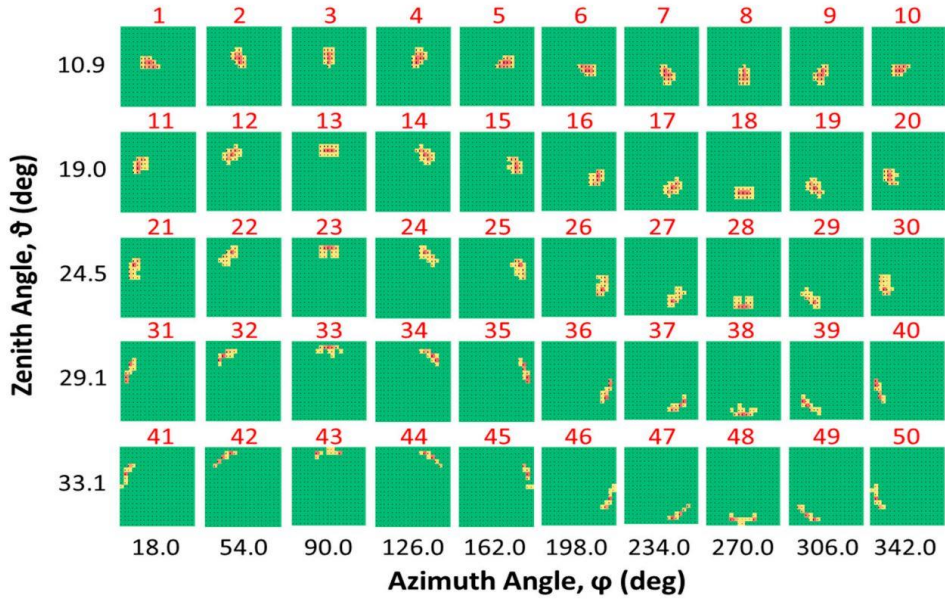


Figure 7.7. Distributions on the readout plane of rays incident to the instrument aperture from 50 directions.

7.4. Use of the Artificial Neural Network

In the current application the input layer of an ANN network consists of 361 nodes describing the power distribution on the readout array, and the output layer consists of 50 nodes describing the corresponding intensities of the beams incident to the instrument aperture. The ANN created for the current application features a 361-node input layer, two 100-node hidden layers, and a 50-node output layer. The output layer error can be determined by direct comparison between the recovered scene (Block 5 in Fig. 7.4) and the target discretized scene (Block 1 in Fig. 7.4). Training of the ANN adjusts its synaptic weights to minimize the errors between these two images. A supervised back propagation (BP) learning scheme was used as the training procedure for feed-forward networks. Also, an Adam optimization algorithm is used in the present study to converge the ANN output with the target scenes during the training process. Mean-squared error (MSE) is used as the objective loss function for the ANN optimization. The learning rate

was ultimately set to 0.0002. Training of the neural network is terminated when a predetermined maximum number of training cycles have been completed. In the current study 40,000 iterations were found as this maximum number to produce good results.

The relative error of predicted output i is defined by

$$RE_i = \frac{|target_i - output_i|}{target_i}, \quad (7 - 3)$$

where $output_i$ is the scene intensity predicted by the ANN, and $target_i$ is the corresponding known scene intensity. In the current investigation, performance is evaluated by calculating the mean value of the relative error,

$$MRE = \frac{1}{n} \sum_{i=1}^n RE_i, \quad (7 - 4)$$

where $n = 50$ for the predicted 50 incident directions in the scene.

7.5. Implementation and results

We create 2000 discretized scenes by combining the 50 primitive beam illumination patterns in Fig. 7.7 after first multiplying each of them by a random scaling factor representing the relative scene intensity corresponding to each direction. This produces a set of 2000 readout array power distributions corresponding to the 2000 scenes viewed by the instrument. Fig. 7.8(a) shows a typical scene intensity distribution and Fig. 7.8(b) shows the corresponding distribution of rays on the readout array. Even though the ray distribution in Fig. 7.8(b) is produced by the single random scene in Fig. 7.8(a), essential features of the optical system are already readily apparent.

We randomly select 1950 of the 2000 readout array/incident-scene pairs to train the ANN. Each of the 1950 361-pixel readout array power distributions is input to the ANN with the goal of reproducing the target 50-element scene. The training

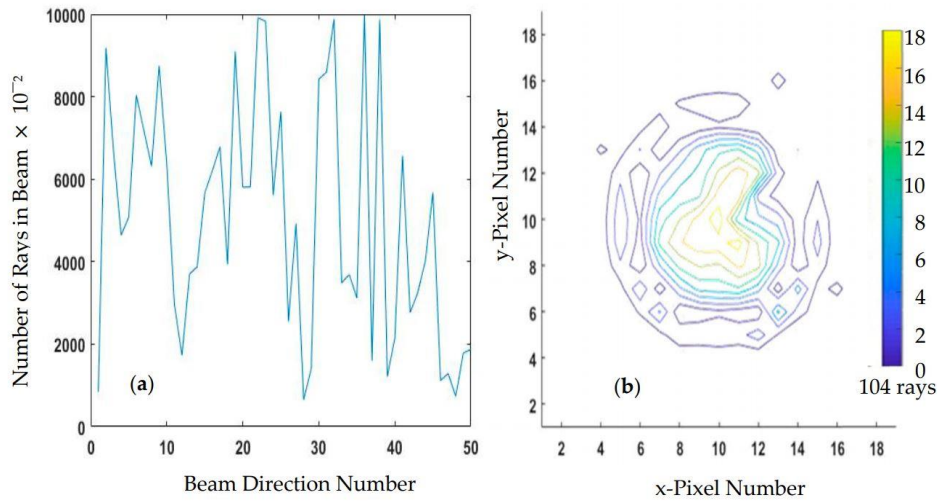


Figure 7.8. (a) A typical scene power distribution over 50 directions, and (b) the corresponding distribution of rays on the readout array.

process uses the optimization algorithm outlined in Section 7.4 to automatically adjust the synaptic weights of the ANN to minimize the global difference between the 1950 target scene intensity distributions and the 1950 scene intensity distributions returned by the ANN. It is emphasized that the ANN is used to solve the inverse problem directly based on the data obtained from the solution of the forward problem using a high-fidelity MCRT model.

We first test the ANN (i.e., establish its accuracy) by introducing the 50 sets of readout array power distributions not already used for training into the trained ANN to produce 50 test scenes. We then compare the test scenes created by the ANN with the corresponding target scenes. Figure 7.9 uses color variations to represent the fifty test “Earth” scenes and the corresponding scenes obtained using the ANN. In the figure, the red end of the color spectrum represents higher intensity and the green end represents lower intensity. While the similarity between Fig. 7.9(a) and Fig. 7.9(b) is evident, with many red and green groupings being clearly identifiable in both, it is also possible to visually discern differences.

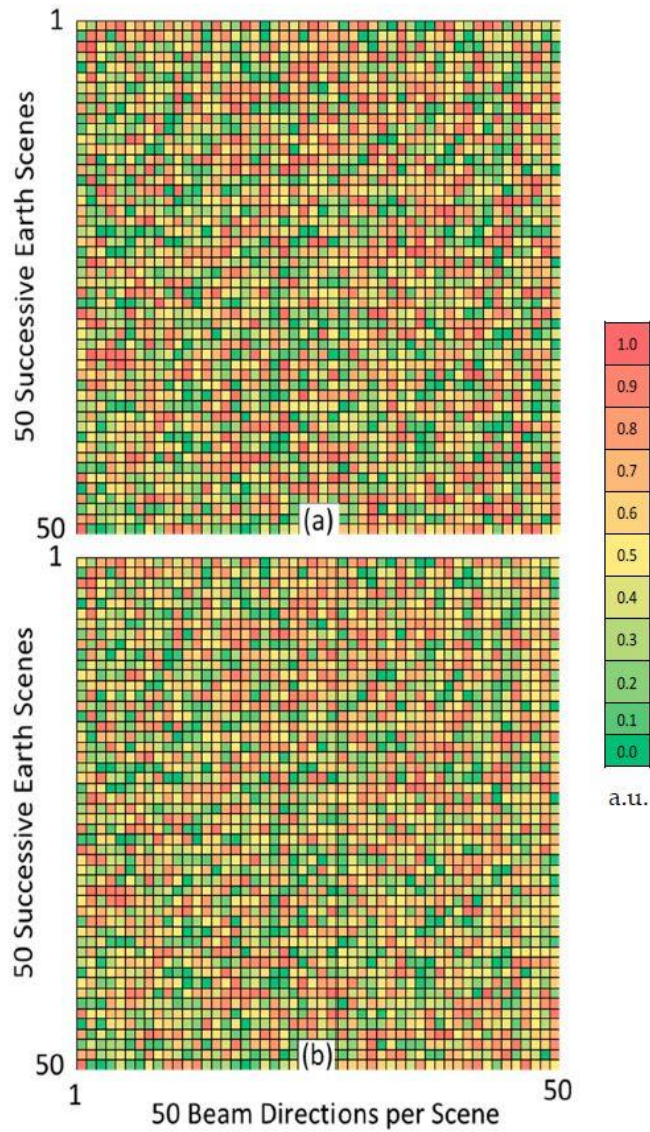


Figure 7.9. Each row represents (a) a random relative intensity distribution incident to the entrance aperture from 50 directions and (b) the corresponding directional relative intensity distribution produced by the ANN.

Figure 7.10 shows the direction-by-direction percentage difference in the scenes in Fig. 7.9(a) and Fig. 7.9(b). In the figure, the green cells indicate percentage differences of less than ± 1.0 percent, and the pink cells indicate differences of greater than ± 1.0 percent. Although the font size in the figure makes individual

numbers difficult if not impossible to read, most of the pink cells in the left-hand third of the figure show values of less than two percent, while a few of the pink cells in the right-hand third show values exceeding 100 percent. The left-to-right degradation of the ANN scene-recovery accuracy is attributable to the declining signal strength with increasing beam number. This conclusion is justified by reference to Fig. 7.8(b), which clearly shows the roll-off of absorbed power with distance from the center of the readout array, and to Fig. 7.7, which shows that Beams 41 through 50 are responsible for illuminating the outer edges of the array. The randomness and unordered sequencing of the 50 scenes used to produce Fig. 7.9 and Fig. 7.10 make it difficult to visually assess the remarkable potential of numerical focusing based on artificial neural networks. A clearer demonstration of



Figure 7.10. Map of the percentage differences between the two images shown in Figure 7.9. Green represents an error of within ± 1.0 percent, and pink represents an error of greater than ± 1.0 percent.

its potential is obtained based on the ordered sequence of fifty scenes shown in Fig. 7.11(a). In the figure each of the fifty scenes, or horizontal strips, can be thought of as emanating from a swath of the Earth that might correspond to an appropriate number of successive RBI scans illustrated in Fig. 7.1. Figure 7.11(a) would then be the result obtained by assembling the fifty RBI-like footprints into an Earth-emitted or Earth-reflected solar image of a region of a notional Earth. Figure 7.11(b) is the assembled sequence of 50 scenes produced by the ANN when the 50 readout array power distributions corresponding to the 50 scenes in Fig. 7.11(a) are input to the ANN.

The scene recovery error associated with a low signal-to-noise ratio in the final ten beam directions is apparent in the right-most portion of Fig. 7.11(b). Otherwise the ability of the ANN numerical focusing scheme to accurately recover the incident scene from the defocused readout array power distribution is well demonstrated.

Figure 7.12 shows the direction-by-direction percentage difference in the scenes in Fig. 7.11(a) and Fig. 7.11(b). In the figure, the green cells indicate percentage differences of less than ± 0.25 percent, and the pink cells indicate differences of greater than ± 0.25 percent. The ability of the ANN to produce results that are consistently within one-quarter of a percent of the actual scene when the scene is so dissimilar to the 2000 random scenes used for training and testing is evidence of strong generalization and a low likelihood of overfitting.

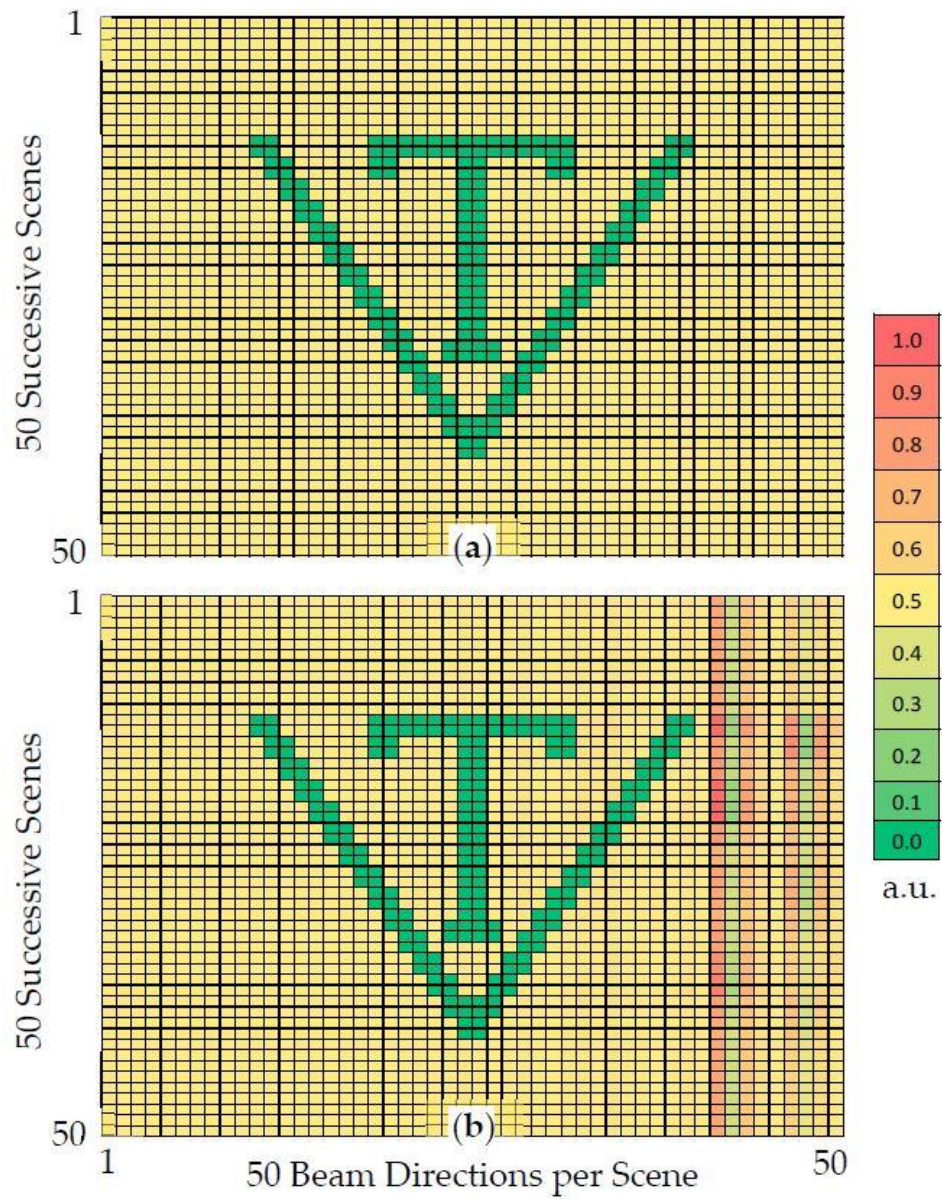


Figure 7.11. Two sets of 50 horizontal strips, each representing the relative beam power distribution incident to the instrument aperture from 50 directions. (a) Target scenes used to create the ANN input, and (b) the corresponding ANN output.

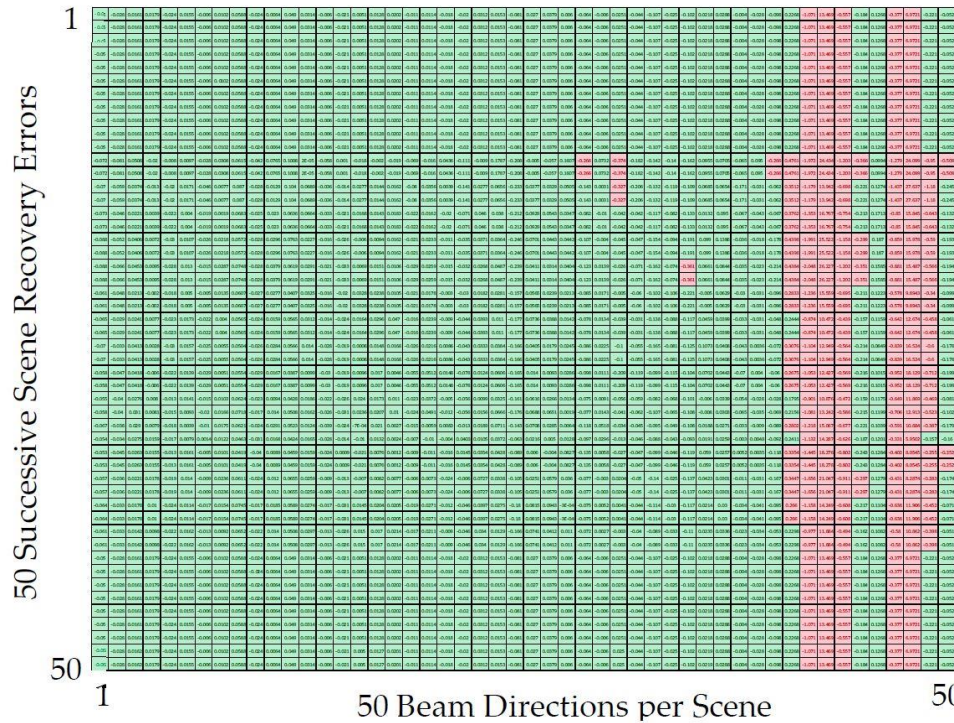


Figure 7.12. Map of the percentage differences between the two images shown in Figure 7.11. Green cells indicate errors less than ± 0.25 percent, pink cells indicate errors greater than ± 0.25 percent.

7.6. Summary and conclusions

Results of the proof-of-concept investigation reported here are limited to scenes consisting of 50 directionally incident beams imperfectly focused onto a 361-pixel microbolometer array. No attempt has been made to optimize or otherwise improve the results by increasing the directional resolution of the scene or the spatial resolution of the readout array. Even using these relatively coarse scene and readout array resolutions, we are able to obtain scene recovery accuracy at the sub-one-percent level over the center portion of the telescope field-of-view using an artificial neural network. An implication of the effort reported here that should not be overlooked is that, once an ANN has been trained on the basis of a high-fidelity

MCRT model of the optical system, the much faster low-order model can be used in subsequent performance evaluation of the system with a significant reduction in computer resources. This means that the actual instrument, once accurately modeled, can provide on-orbit Earth radiation scene observations in real time. An alternative to relying upon the high-fidelity MCRT model to tune the ANN model would be preflight calibration of the actual instrument. This would involve the use of a steerable beam light source of known intensity in a thermal-vacuum chamber. During on-orbit operation the elements of the two-dimensional readout array would be time-sampled to obtain a sequence of intensity distributions incident to the imager entrance aperture from the discrete directions for which it was trained. The inverse optical model is sufficiently fast to obtain these images in real time. Note that the image obtained is discretized even though the scene being observed is continuous, as is true in the case of any imager based on an ordinary focal-plane array (FPA). However, in this case the number of scene pixels—fifty in the current application—is generally different from the number of FPA pixels—361 in the current application. In a future effort the relationship between these two numbers could be studied in an effort to maximize the accuracy of the method.

We conclude that ANNs offer a viable means for creating computationally efficient models of complex optical systems from computationally intensive high-fidelity models based on the MCRT method. Specifically, while the MCRT method requires more than four hours to solve the forward problem of readout array illumination, the solution, once obtained, may be used to train an ANN to solve the much more interesting inverse problem of recovering the incident scene in real time.

Chapter 8:

Recovery of Water Cloud Properties Using an Artificial Neural Network

The influence of water clouds on the planetary energy budget depends on cloud top height, thickness, liquid water content, and droplet size distribution. Sun-photometry is one of the tools available for determining the latter two of these properties. Presented is a novel approach for interpreting the angular distribution of cloud radiance at nadir when viewed from below in terms of mean droplet size and liquid water content using an artificial neural network (ANN). A Monte Carlo ray-trace (MCRT) model based on Mie scattering is used to predict the angular distribution of transmitted solar radiance at nadir for a range of droplet size and

cloud liquid water content. Once a sufficiently large population of numerical experiments has been carried out, the results are used to train an artificial neural network. While creation of the ANN is numerically intensive, once created it can be used for real-time recovery of cloud properties from sun-photometer measurements. This chapter is based on an article by the author currently in press for publication in **Remote Sensing** entitled “Recovery of Water Cloud Properties from Solar Aureole Photometry Using an Artificial Neural Network”.

8.1. Introduction

Water clouds play an essential role in determining weather and climate [119-124]. Atmospheric aerosols may influence the climate either directly—by scattering and absorbing radiation—or indirectly—by acting as cloud condensation nuclei. Water clouds, once formed, are strong scatterers of solar radiation depending on their liquid water content and their liquid droplet size distribution. Measurement of cloud properties is key to building cloud models.

Sun-photometry, or aureolemetry, is a relatively inexpensive approach to cloud metrology when compared to the alternative of Raman lidar sounding [125], especially if the latter is to be implemented from low Earth orbit. In sun-photometry the measured angular distribution of cloud radiance observed from below uses a physics-based model to tease out the cloud properties. This is an inverse parameter estimation problem which can be stated, “given an observed angular distribution of solar radiation under a cloud bank, find the values of mean droplet size and cloud liquid water content that produced it.” We seek a computationally efficient and accurate strategy for solving this inverse problem in real time, that is, during observation. Our approach is based on that bastion of artificial intelligence, the Artificial Neural Network (ANN).

8.2. Simulation of scattering in water clouds

Consider the situation in which the circumsolar sky radiance ($\text{Wm}^{-2}\text{sr}^{-1}$) is monitored from below. Even on a perfectly cloudless day we find that the sky radiance decreases from a large value I_1 at the edge of the solar disk ($\vartheta = \vartheta_e \approx 0.3$ deg) to a smaller uniform value I_2 sufficiently far from the solar disk. The radiance distribution in the solar aureole may then be written

$$I(\vartheta) = (I_1 - I_2)f(\vartheta) + I_2, \quad (8 - 1)$$

where $f(\vartheta)$ is a monotonically decreasing function of ϑ varying from $f(\vartheta_e) = 1$ to $f(\vartheta_a) \rightarrow 0$ as $\vartheta \rightarrow \vartheta_a$, where ϑ_a is the angle at which the sky radiance can be considered uniform. The values of both ϑ_e and ϑ_a are somewhat vague, and so experimental results are normally presented over a range of I and ϑ where both can be conveniently measured. Measurements are typically made using a sun-photometer, or aureolemeter, with direct sunlight masked by an occulting element [126] or a solar radiation trap [127, 128]. Generally speaking, the values of I_1 , I_2 and the angular extent of the solar aureole are functions of droplet concentration and size distribution and wavelength.

8.2.1. Mie scattering in the MCRT environment

Mie scattering, which describes the phenomenon that occurs when light interacts with a particle that is similar to or larger than the wavelength of the light, is commonly used to simulate the interaction of light with atmospheric aerosols. Although scattering centers are usually assumed to be spherical, according to Bohren and Huffman [129], Mie theory provides a first-order description of optical effects in non-spherical particles and correctly describes many small-particle effects even when they are not immediately obvious.

According to the Mie scattering model, naturally polarized monochromatic light will be scattered into several lobes that are symmetric across the plane of incidence

but heavily favor forward-scattering (0 deg), as illustrated in Fig. 8.1. The refractive index m relative to air of pure water in the solar spectrum is essentially real, so that scattering is elastic; i.e., the power carried by a scattered ray remains constant.

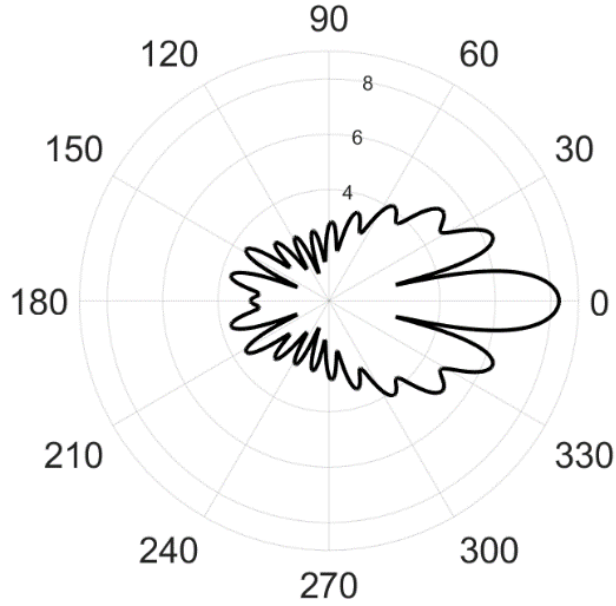


Figure 8.1. Cross-section in the plane of incidence showing the angular distribution, in degrees, of a Mie scattering event from a spherical liquid water droplet ($m = 1.304 - j 0.24 \times 10^{-6}$) of radius $a = 1 \mu\text{m}$ for a wavelength $\lambda = 0.55 \mu\text{m}$.

In 2002, Mätzler [130] published Matlab functions that serve as the foundation of our MCRT model. According to Mätzler the electric field distribution in the far field of a single scattering event may be expressed in spherical coordinates as

$$E_{s\vartheta} = \frac{e^{ikr}}{-ikr} \cos\varphi S_2(\cos\vartheta) \quad (8 - 2)$$

and

$$E_{s\varphi} = \frac{e^{ikr}}{ikr} \sin\varphi S_1(\cos\vartheta), \quad (8 - 3)$$

where

$$S_1(\cos \vartheta) = \sum_{n=1}^{\infty} \frac{2n+1}{n(n+1)} (a_n \pi_n + b_n \tau_n) \quad (8-4)$$

and

$$S_2(\cos \vartheta) = \sum_{n=1}^{\infty} \frac{2n+1}{n(n+1)} (a_n \tau_n + b_n \pi_n). \quad (8-5)$$

In Eqs. (8-2) and (8-3), r , ϑ , and φ are the usual spherical coordinates, and $k = 2\pi/\lambda$ is the angular wavenumber; in Eqs. (8-4) and (8-5) a_n and b_n are standard Mie coefficients whose formulas are given in Reference 130; and

$$\pi_n = \frac{2n-1}{n-1} \cos \vartheta \pi_{n-1} - \frac{n}{n-1} \pi_{n-2} \quad (8-6)$$

and

$$\tau_n = n \cos \vartheta \pi_n - (n+1) \pi_{n-1}. \quad (8-7)$$

In the MCRT environment, the angular distribution of scattered rays is determined using the scattering amplitude functions S_1 and S_2 . Because the current application deals with naturally polarized light, only two-dimensional scattering need be considered; radiance does not vary with azimuth angle φ and so we are concerned only with the zenith angle ϑ . For each ray, we draw a pseudorandom number R_ϑ and use it to calculate the corresponding scattering angle ϑ_s by numerically solving the integral equation

$$R_\vartheta = \frac{\int_0^{\vartheta_s} \sqrt{S_1^2 + S_2^2} d\vartheta}{\int_0^{2\pi} \sqrt{S_1^2 + S_2^2} d\vartheta}. \quad (8-8)$$

With the scattering angle calculated we then draw the next available pseudorandom number R_d and use it to calculate the distance d_s the ray travels before being scattered again [3] (p. 161),

$$d_s = -\frac{1}{\sigma_e} \ln(1 - R_d). \quad (8 - 9)$$

In Eq. (8-9), σ_e is the monochromatic aerosol extinction coefficient, which is related to the droplet mean size and the liquid water content, as developed in Eqs. (8-10) – (8-14). Each ray is scattered a predetermined maximum number of times before exiting a cloud, and the scattering angle and distance for each scattering event are stored for later use.

Finally, we assume independent scattering in the present treatment. That is, we assume that the observable effect of multiple scattering events can be summarized as a single scattering event. Dependent scattering occurs when particles are so densely packed that their electromagnetic fields interact with those of their neighbors, an effect excluded in ordinary Mie scattering theory. Bressel and Reich [131] have studied dependent scattering in the Monte Carlo ray-trace environment and present results which quantify the departure from (independent) Mie scattering due to this effect. The inclusion of dependent scattering in our model would presumably improve its ability to represent actual field data, thereby enhancing the success of our ANN-based strategy for recovering cloud properties from sun-photometer observations.

8.2.2. *Cloud properties*

The artificial neural network used to recover the cloud properties must be trained and validated using a large sky-radiance database that covers the range of cloud properties likely to be encountered. In the absence of a sufficiently massive experimental database, we have derived and used a heuristic cloud-radiance model to create one. The solar disk, when viewed from the Earth on a clear day, subtends a half-angle of about ± 0.3 deg, and is surrounded by an aureole of scattered light out to viewing angles of 7-9 deg. However, when observing the sun from below a sufficiently thick cloud bank, the well-defined solar disk is replaced by a circular region of the sky in which the intensity diminishes asymptotically with viewing

zenith angle, as described by Eq. (8 - 1). In the extreme case of a very thick cloud bank, it is no longer possible to locate the sun in the uniformly radiant sky. Because of the forward directional bias associated with Mie scattering, solar radiation incident to the top of the cloud bank at angles beyond 0.3 deg contribute progressively less to the circumsolar radiance viewed from below as the incidence angle increases. Therefore, as a matter of convenience, our cloud radiance model ignores radiation incident to the top of the cloud bank at zenith angles greater than 0.3 deg. Although compromised to the extent that cloud irradiation at zenith angles beyond 0.3 deg may be important from the point of view of cloud science, our model produces angular distributions of cloud radiance consistent with everyday experience on a gloomy day and in qualitative agreement with those reported in the literature [127, Figs. 8 and 10]. More to the point, and as subsequently demonstrated, our model produces a sky radiance angular distribution that is sensitive to cloud droplet mean size and liquid water content in cloud banks through which a solar aureole is visible. It is strenuously emphasized that, while the cloud model invoked here is intended to capture the essential elements of cloud optical physics, the author makes no claim as to its ability to match actual field observations. The goal of this contribution is not to shed new light on cloud science per se, but rather to establish the utility of a new measurement tool capable of furthering cloud science.

Observations of the solar aureole are often interpreted assuming diffraction as the primary scattering mechanism [127], but property recovery accuracy is expected to be improved using the more realistic Mie scattering model described in Section 8.2.1. In the current contribution, the gathering of scattered radiation by a sun-photometer, or aureolemeter, is simulated using the Monte Carlo ray-trace (MCRT) method [3]. In a previous simulation of solar aureolemeter performance using the MCRT method [128], it was found to be necessary to trace an excessively large number of rays to assure the desired accuracy. The current application involves a

parametric study requiring many ray traces in which the aerosol properties are varied from one ray-trace to the next. In anticipation of the implied potential for overloading available computational resources, we have developed an efficient ray-trace strategy in which far fewer rays are required to yield the same accuracy. We then use this cloud scattering model to produce the extensive dataset required to compose, train, and test an artificial neural network (ANN) capable of recovering H₂O droplets properties from solar aureole observations.

To demonstrate the methodology introduced here, we consider only the liquid H₂O droplet present in mature clouds. While all water cloud droplets are formed by the condensation of water vapor on dry aerosol cores such as volcanic ash, fine sand, sea salt, and pollen, we assume here that the resulting droplets are large compared to their original dry cores. This allows us to consider, without compromising the validity of the methodology, only droplets having the refractive index of pure water, a constraint that can be relaxed in future applications. The creation of candidate H₂O droplets in this scenario requires the convergence of concentrations of dry aerosols and a saturated air mass [119-124]. We further assume that mixing has progressed to the point that all of the dry aerosols have been consumed and local thermodynamic equilibrium has been established between the liquid and vapor phases. The type and concentration of available dry aerosols and water vapor depend on geography and season. Local relative humidity directly impacts the number and size distribution of water droplets in a portion of the sky. It follows that particulate-level metrology of the cloudy sky provides information of interest to weather and climate modelers. While cloud formation, evolution, and dissipation is a dynamic process, the observations modeled here are intended to simulate quasi-stationary conditions.

A robust cloud model must include the properties that characterize cloud structure. For each numerical experiment we specify the size of spherical water droplets in terms of a mean radius a , ranging from 1 to 50 μm , and the cloud liquid water

content LWC ranging from 0.5 to 1.5 gm^{-3} . Here we define LWC as the mass of water in a specified volume of dry air. The essential scattering behavior of the cloud can be deduced from these two properties.

The wavelength λ used in the model is 0.55 μm , which lies near the center of the visible spectrum. The refractive index of water droplets at this wavelength is $m = 1.304 - j 0.24 \times 10^{-6}$. Therefore, absorption of visible light in the cloud can be safely neglected compared to scattering. As demonstrated by Platt [15], this is not generally true in the infrared, so the applicability of the model developed here is limited to the visible part of the spectrum. This means that for pure water droplets the extinction efficiency Q_e is essentially equal to the scattering efficiency Q_s . Thus, the Mie extinction efficiency Q_e is

$$Q_e \approx Q_s = \frac{2}{x^2} \sum_{n=1}^{\infty} (2n+1)(|a_n|^2 + |b_n|^2), \quad (8-10)$$

where $x \equiv ka = 2\pi a/\lambda$, the size parameter.

The number density n of water droplets in a cloud of volume V_c is related to its liquid water content by

$$n = \left(\frac{LWC}{\rho} / \frac{4\pi}{3} a^3 \right) \frac{V_{da}}{V_c}, \quad (8-11)$$

where ρ is the mass density of liquid water in gm^{-3} and V_{da} is the volume of dry air within the cloud. In the simulation carried out here we assume that the ratio $V_{da}/V_c \approx 1$ for all practical purposes [132].¹ Given the droplet number density and the Mie extinction efficiency, we can find the collision cross section σ_c , the mean free path L between scattering events, and the extinction coefficient σ_e ;

¹ $V_c = V_l + V_g$ and if all available H_2O vapor has condensed $V_g = V_{da}$. According to Pelkowski and Frisius [131] (p. 2433), $V_l/V_g \ll 1$ in a cloud. Thus, $V_c/V_{da} = V_l/V_{da} + 1 \approx 1$.

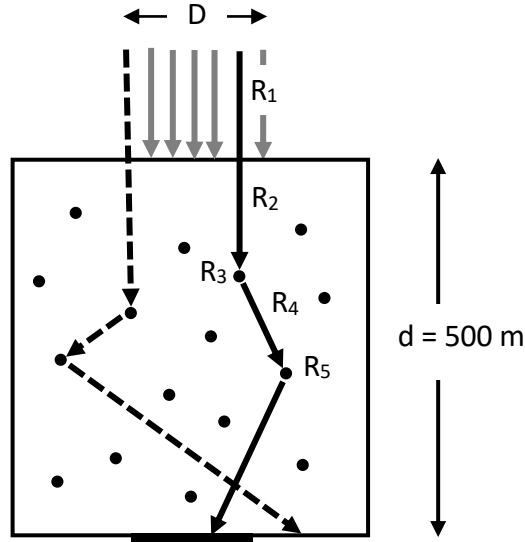


Figure 8.2. Ray-trace concept for cloud radiance and aureolemeter simulation (the beam diameter and detector size are not drawn to scale).

The blue ray is successful but the red ray is unsuccessful.

$$\sigma_c = 4\pi a^2 Q_s, \quad (8-12)$$

$$L = \frac{1}{n\sigma_c}, \quad (8-13)$$

and

$$\sigma_e = \sigma_s = \frac{1}{L}. \quad (8-14)$$

The cloud physical depth d can now be invoked to obtain its optical depth $\tau = \sigma_e d$.

8.2.3. MCRT-based multiple scattering simulation

A slab of cloudy atmosphere with a thickness $d = 500$ m is assumed to be populated by spherical water droplets suspended in otherwise fully transparent dry air and having a specified size distribution $n(a)$. Their relative refractive index with respect to air is assumed to be $m = n + ik = 1.304 - i 0.24 \times 10^{-6}$

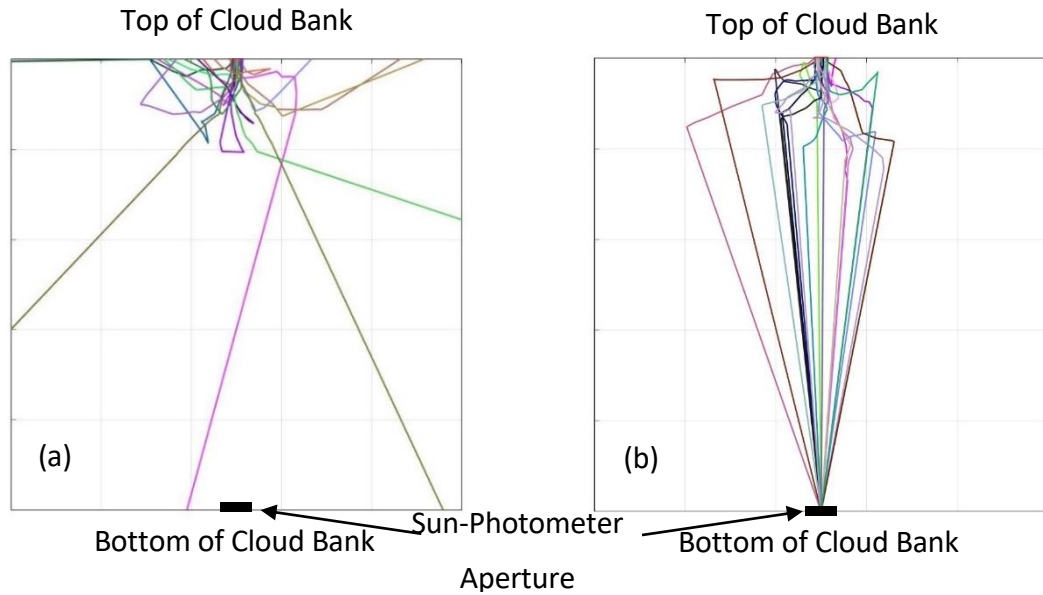


Figure 8.3. Ray-trace for (a) natural scattering and (b) for forced scattering in a vertically finite cloud for $N = 10$ scattering events.

corresponding to $\lambda = 0.55 \mu\text{m}$. Figure 8.2 is a schematic representation of individual rays traversing the simulation space. Consistent with the ideas introduced in Section 8.2.2, a collimated beam of sunlight with diameter D is normally incident on the upper surface of the slab representing the top of a cloud bank. We have found that varying the incidence angle of individual rays within this narrow range does not influence the outcome of the numerical experiment. Due to the relatively small size of the aureolemeter entrance aperture, a large number of rays is required to adequately simulate its illumination. This runs counter to the need for a computationally fast simulation.

Individual rays traced inside the cloud are deemed to be either successful or unsuccessful. The ray that strikes the photometer in Fig. 8.2, represented by the solid black arrows, is an example of a successful ray, while the ray that misses the photometer, represented by the dashed black arrows, is deemed unsuccessful. Back-scattered rays which reach the upper boundary of the simulation space are

abandoned and a new ray is launched into the solution space. Finally, when a ray reaches the underside of the cloud it is assumed to either enter or miss the photometer; both instances are archived.

In a scattering model, the path of a ray can be determined by $2N + 1$ random numbers for N scattering events. Figure 8.2 illustrates a two-dimensional model with only two scattering events per ray. For two successive scattering events, random number R_1 determines the location where the ray enters the cloud, random numbers R_2 and R_4 determine the distance the ray travels inside the slab between scattering events using Equation (8-9), and random numbers R_3 and R_5 determine the scattered direction of the ray, using Equation (8-8).

It is convenient to distinguish between *natural* scattering and *forced* scattering. By natural scattering we mean that rays entering the cloud from the top are scattered inside the cloud for up to N_{max} scattering events. Each scattering event has two corresponding results: the distance the ray travels inside the cloud before scattering d_s , and the new direction θ_s based on the Mie scattering model. The number N_{max} is a predefined value to be determined. Figure 8.3(a) shows a ray-trace using the natural scattering model for twenty rays with $N_{max} = 10$ scattering events.

We observe that none of the twenty rays in Fig. 8.3(a) are incident to the small photometer aperture at the center of the cloud lower boundary. Traced rays can fail in three different manners in the natural scattering model:

1. They can be backscattered and exit the cloud from the upper boundary.
2. They can exit the cloud through one of the lateral boundaries.
3. They can exit through the lower boundary without being detected.

Because of the small size of the photometer entrance aperture, it is very rare for a ray that survives the first two failure modes to intersect it.

It is obvious that during natural scattering an inadequate number of rays will be counted to obtain a statistically meaningful distribution of rays on the aperture. Even if the number of rays reaching the photometer is statistically significant, their number may still be insufficient to determine a meaningful angular distribution. Large numbers of rays must be traced in the natural scattering model, making it computationally extremely expensive. The natural scattering model cannot be used by itself because of its high demand on computational resources due the excessive number of rays that must be traced. However, it is still useful in combination with the concept of forced scattering. In forced scattering every ray is obliged to enter the photometer after a number N of scattering events, assuming it has not already exited the cloud. Natural scattering, but with a lesser number of rays traced, is then used to estimate the likelihood of the eventual occurrence of a given forced ray trajectory.

In natural scattering it is recognized that if a sufficiently large number of rays are traced, a statistically significant number will intercept the aperture in any given angular bin. Therefore, if the ray at the final scattering event is forced to enter the aperture, a ray history is involved that would eventually have occurred in natural scattering. In the forced scattering model, as in the case of natural scattering, the number of scattering events N is predefined. If the ray survives to the final scattering event, it is forced to continue to the photometer. This principle is illustrated in Figure 3(b), which shows forced scattering in a vertically finite, laterally infinite cloud with twenty rays and $N = 10$ scattering events.

Figure 8.3(b) shows that 18 of the 20 rays are successful in that they are incident to the small entrance aperture in the center of the lower cloud boundary. It is obvious that forced scattering in a vertically finite cloud significantly increases the number of successful rays compared to natural scattering. The likelihood of occurrence, or

weight w_i , of a forced-scattered ray trajectory is determined by counting successful rays in natural scattering experiments; that is,

$$w_i = \frac{S_i}{\sum_{j=1}^{N_{max}} S_j}, \quad i = 1, 2, \dots, N_{max}, \quad (8-15)$$

where w_i is the probability that a ray is collected by the photometer after the i th scattering event, S_i is the number of successful rays in natural scattering after i scattering events, and N_{max} is the maximum number of scattering events.

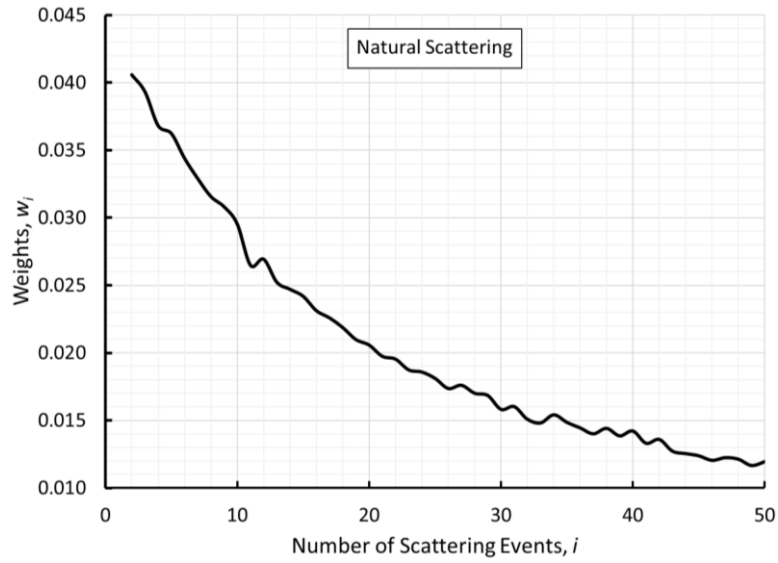


Figure 8.4. Weights determined from 49 natural scattering experiments, involving 25M rays per experiment, as a function of the number of scattering events, computed using Equation (8-15).

Figure 8.4 shows the values of the natural scattering weights as a function of the number of rays traced. It is based on 49 MCRT experiments, each involving 25 million rays traced and together requiring a total of 20 hours of execution time on an 806-GFlops/s system.

The average probability $p_{K,j}$ that the ray will enter angle bin j of the photometer after a given maximum number of scattering events $N_{max} = K$, is

$$p_{K,j} = \sum_{i=1}^{N_{max}=K} w_i p_{i,j}, \quad (8-16)$$

where $p_{i,j}$ is the probability that a ray strikes the photometer at angle j after i scattering events, and N_{max} is maximum number of scattering events.

Figure 8.5 is a probability density function computed using Equation (8-16) for a range of values of the maximum number of scattering events, $K = N_{max}$, and Figure 8.6 is a plot of the mean relative difference between the average of two consecutive curves in Figure 8.5, defined

$$\text{Mean Relative Difference} = \langle 100(p_{K,j} - p_{K-1,j})/p_{K,j} \rangle (\%) \quad (8-17)$$

Arbitrarily using a 5% Mean Relative Difference as a convergence criterion, we obtain $N_{max} = 39$. Figure 7 is the PDF corresponding to Equation (8-16) with $K = N_{max} = 39$ for a water droplet mean size of $25.6 \mu\text{m}$ and cloud liquid water content of 1.0165 gm^{-3} , yielding a scattering coefficient of $\sigma_e = 0.2212 \text{ m}^{-1}$.

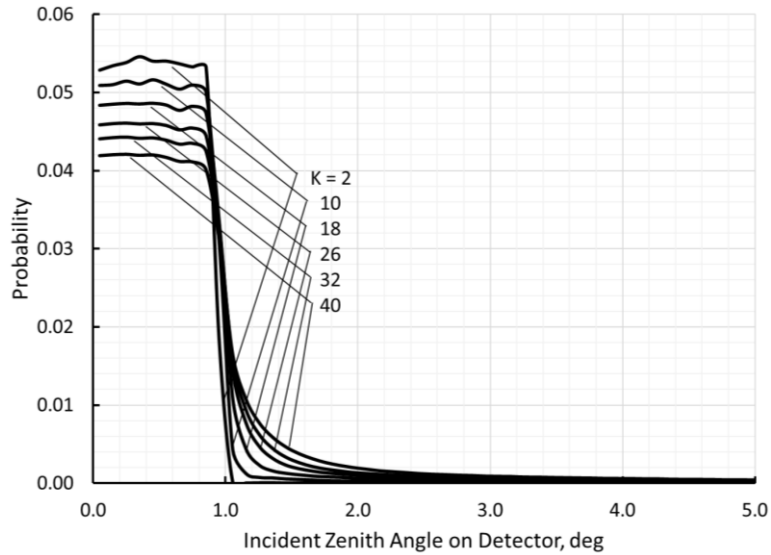


Figure 8.5. Average probability density functions (PDFs) corresponding to $N_{max} = K$ scattering events.

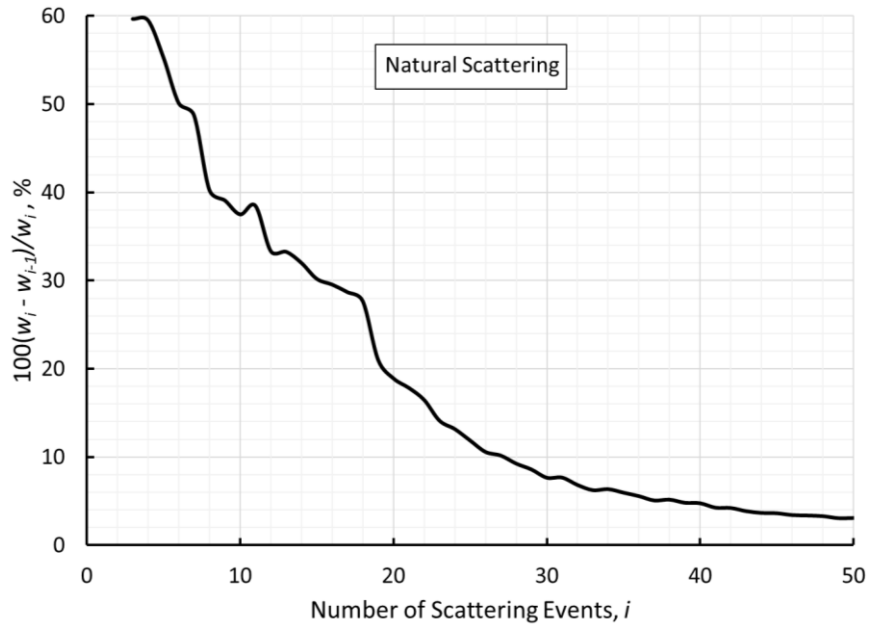


Figure 8.6. Convergence of the Mean Relative Difference with the number of maximum scattering events.

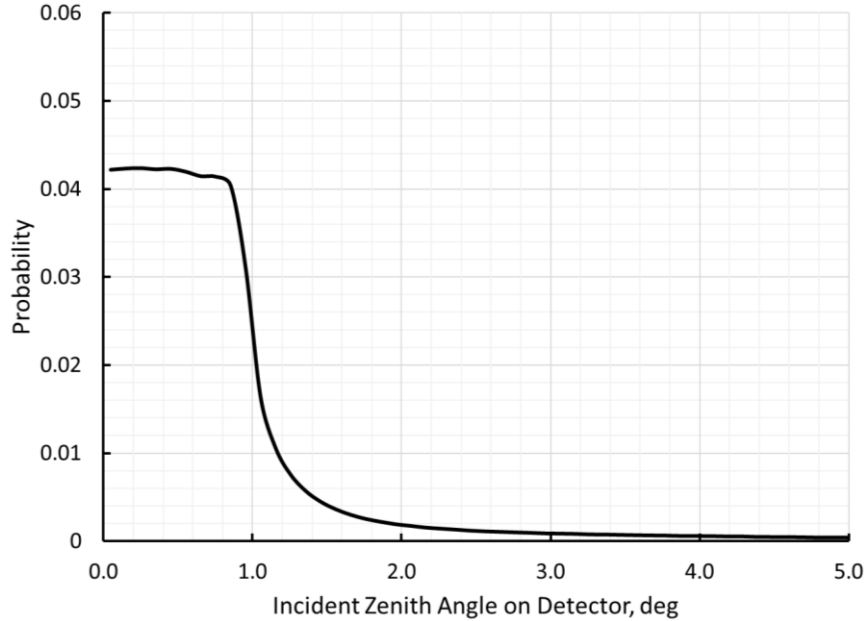


Figure 8.7. Probability distribution function (PDF) for a water droplet mean size of $a = 25.6 \mu\text{m}$ and a cloud liquid water content $LWC = 1.0165 \text{ gm}^{-3}$ ($\lambda = 0.55 \mu\text{m}$).

8.2.4. Parameterization of the PDF profile

Fig. 8.8 shows the PDF profiles for the incident zenith angle at the photometer for combinations of water droplet mean size and liquid water content selected because they produce distinctively different profiles. The profiles in the left-hand column are plotted on a linear scale, while those in the right-hand column are the same data plotted on a semi-log scale. The PDF profiles in the linear plots can be divided into three segments. Segment 1 lies to the left of the first vertical line, where the profile is relatively flat; segment 2 is the steeply sloped segment between the two vertical lines, and segment 3 is the more gently sloped segment lying to the right of the second vertical line. The first vertical line is drawn at the incident angle where the local slope goes above a predetermined threshold, and the second vertical line is drawn where the local slope drops back below the same threshold. The three segments can be characterized using five parameters. The first parameter c_1 is the average of the probability in segment 1, the second parameter c_2 is the probability at the intersection point of the profile with the first vertical line, and the third parameter c_3 is the probability at the intersection of the profile with the second vertical line. A first-order power-law curve,

$$f(\vartheta) = c_4 \vartheta^{c_5}, \quad (8 - 18)$$

is fitted to the logarithm of the PDF profile in segment 3. The five parameters and the corresponding cloud properties are listed in Table 8.1 for the two cases represented by Fig. 8.8. The similarity between the incident angle profiles revealed in this figure and those found in the literature; e.g., Figs. 8 and 10 in Devore et al. [127] is gratifying.

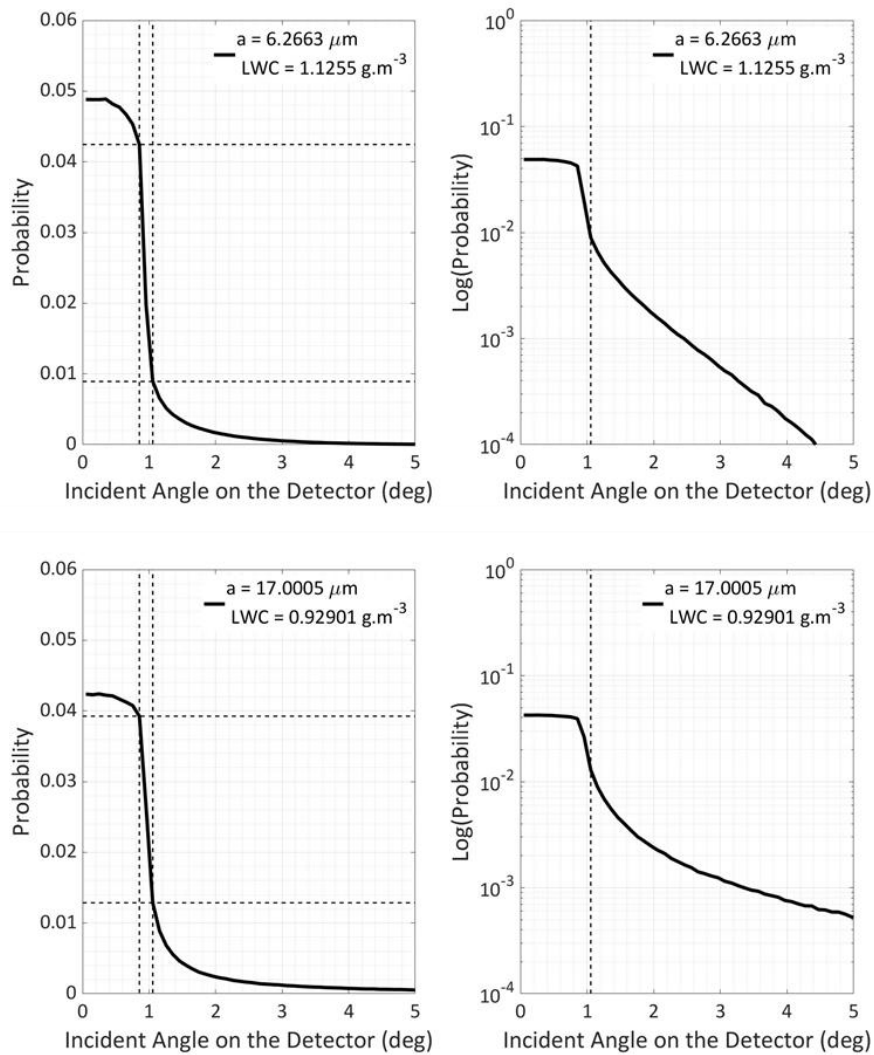


Figure 8.8. Probability distribution function of incident angle on the photometer aperture for two different pairs of cloud properties.

Table 8.1. Characterization numbers for two different pairs of cloud properties.

a (μm)	LWC (g.m^{-3})	c_1	c_2	c_3	c_4	c_5
6.2663	1.1255	0.0472	0.0424	0.0089	-3.5152	0.6979
17.0005	0.9290	0.0416	0.0393	0.0129	-4.9301	0.2663

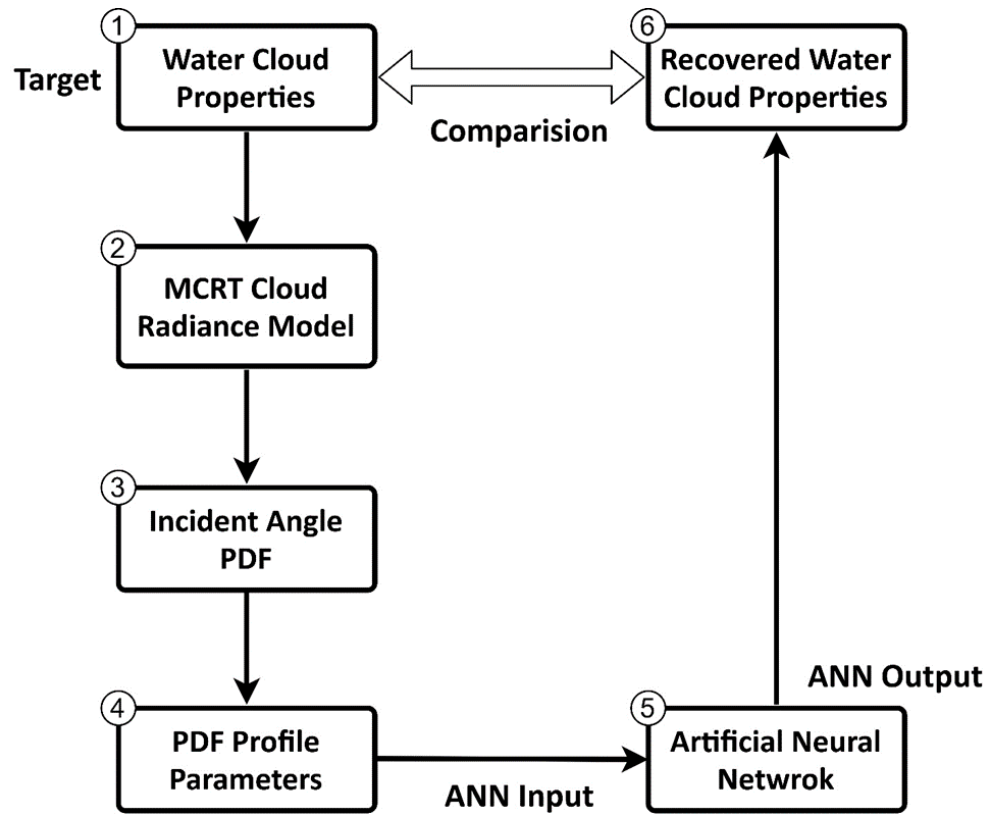


Figure 8.9. Logic flow in creating and using an ANN to recover cloud properties.

8.3. Property recovery using an Artificial Neural Network (ANN)

In this section a novel approach similar to that described in Chapter 7, is presented for recovering water cloud properties from the incident zenith angle PDF profiles recovered from sun photometer observations. The first step is to simulate the physical measurement. Simulation is necessary because of the current lack of an adequately voluminous database containing both sun-photometer angular incidence data and the corresponding water cloud properties. As described in Section 8.2, a Mie-scattering-based Monte Carlo ray-trace model is used to create a large population of PDF profiles corresponding to randomly selected values for the droplet mean size a and cloud liquid water content LWC . For each

combination of cloud properties, the parameters listed in Table 8.1 are recovered as described in Section 8.2.4. These parameters then become the input to an Artificial Neural Network (ANN) whose output is the recovered water cloud properties. Ninety percent of the population of simulated sun-photometer measurements is randomly selected to train the ANN and the remaining ten percent is used to test it. Once validated, the ANN may then be used to recover the water cloud properties for any subsequently measured incident angle distribution. The logic flow diagram of the approach appears in Fig. 8.9.

8.3.1. Creation and training of the ANN

Step 1. Create a population of cloud property/PDF profile parameter pairs

Block 1 in Fig. 8.9 represents a pool of random-valued water cloud properties. Random water droplet mean sizes are distributed between 1 to 50 μm , and random values of cloud liquid water content are distributed between 0.5 to 1.5. These values are introduced into the MCRT simulation described in Section 8.2 and represented by Block 2. The PDF profile of the zenith angles of rays collected by the sun-photometer are formed in Block 3, and in Block 4 the PDF profile is interpreted in terms of the five parameters discussed in Section 8.2.4. During Step 1, 1000 sets of random-valued water cloud properties are created and passed to the MCRT simulation, producing 1000 corresponding incident zenith angle distributions on the sun photometer. These are in turn converted to 1000 sets of PDF profile parameters.

Step 2. Training the ANN

A random selection of 90 percent of the 1000 pairs of cloud properties and corresponding PDF profile parameters are used to train the ANN represented by Block 5. In each case, the five PDF profile parameters are introduced to the ANN, which then produces a corresponding set of cloud parameters. Synaptic weights of the ANN are adjusted in an iterative process, described in Section 8.3.2, which

minimizes the difference between the cloud properties produced by the ANN, represented by Block 6, and the corresponding target cloud properties in Block 1.

Step 3. Testing the ANN

The 10 percent of the PDF profiles created in Step 1 that were not used to train the ANN in Step 2 are converted to profile parameters and then introduced into the trained ANN as test data. The resulting water cloud properties (Block 6) in each case is compared to the target cloud properties (Block 1) used to create them. The differences between corresponding ANN output and target properties provide a measure of the success of the proposed neural network scheme.

Step 4. Prediction of unknown water cloud properties from sun-photometer measurements.

Availability of a properly trained and tested ANN model renders further MCRT-based simulation unnecessary. From this point forward, the trained ANN model can be reliably used to recover the water cloud properties from sun-photometer measurements by following the path Block 3→Block 4→Block 5→Block 6. Of course, this supposes that the cloud radiance model used to train the ANN represents actual cloud physics. Implied is the need for a campaign in which actual sun photometer observations, backed up by simultaneous independent cloud property measurements, are used to improve the MCRT-based cloud radiance model.

8.3.2. ANN implementation

An RMS-prop optimization algorithm is used here to converge the ANN output during the training process. RMS-prop uses a moving average of squared gradients to normalize the gradient itself. That has the effect of balancing the step size; it decreases the step size for large gradients to avoid exploding, and increases the step size for small gradients to avoid vanishing. This optimization method has several

advantages; for one, it is a very robust optimizer which preserves pseudo curvature information. Additionally, it effectively deals with stochastic objectives.

The training, validation, and test loss functions are all mean-squared errors (MSE). The learning rate was ultimately set to 0.005 and 30,000 iterations were found to produce good results.

The relative error of predicted output i is defined

$$RE_i = \frac{|target_i - output_i|}{target_i}, \quad (8 - 19)$$

where $output_i$ can be either of the two water cloud properties predicted by the ANN, and $target_i$ is the corresponding known cloud property.

8.4. Results

A population of 1000 random combinations of water droplet mean size and cloud liquid water content was created. Each combination of cloud properties was then introduced into the MCRT simulation to produce a set of 1000 simulated incident angle distributions, as described in Section 8.2.3. The resulting PDF profiles were then parameterized, as described in Section 8.2.4. A randomized subset of 900 of the 1000 PDF profile parameters/cloud property pairs was used to train the ANN. Each PDF profile parameter set is introduced into the ANN with the goal of recovering the two related water cloud properties. The training process uses the optimization algorithm described in Section 8.3.4 to automatically adjust the synaptic weights of the ANN to minimize the global difference between the target water cloud properties and those returned by the ANN. The target water cloud properties are those used in the MCRT simulation to produce the PDF profile parameters. It is emphasized that the ANN is used to solve the inverse problem directly based on the data obtained from the MCRT simulation of the forward problem. After training the ANN, it is tested (i.e., its accuracy is established) by introducing the 100 remaining sets of PDF profile parameter not already used for

training into the trained ANN. In a final step, the recovered cloud properties created by the ANN are compared with the corresponding target cloud properties. The ability of the trained ANN to recover the target droplet size from corresponding sets of PDF profile parameters for both the training and the test data is illustrated in Fig. 8.11. The corresponding percentage errors,

$$\text{Percentage Size Error} = \frac{|a_{ANN} - a_{Target}|}{a_{Target}} \times 100\%, \quad (8 - 20)$$

are plotted in Fig. 8.12. While acceptably small for droplet sizes exceeding about 10 μm , size error expressed as a percentage becomes large for small droplet size. This is because of the small target water droplet size in the denominator and the more or less fixed absolute error in the numerator in Eq. (8-20). The apparent contradiction between Figures 8.11 and 8.12 at small droplet sizes is an artifact of the definition of absolute and relative errors. To put this result in perspective, less

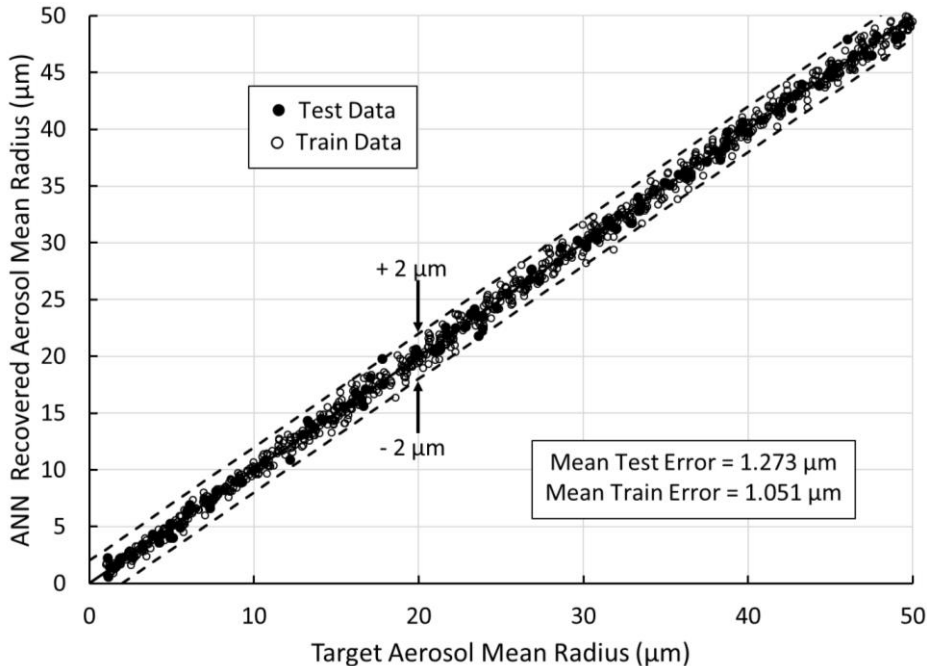


Figure 8.10. Comparison of ANN recovered droplet mean radius with target mean radii used in the MCRT-based cloud radiance model.

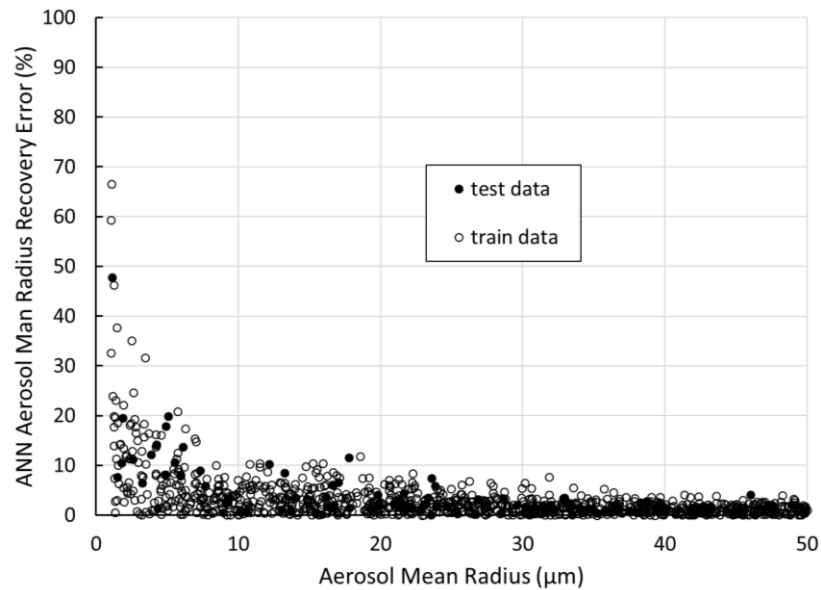


Figure 8.11. Variation of ANN droplet mean radius recovery error with droplet mean radius.

than ten percent of the droplets making up cumulus clouds have sizes of 10 μm or less. These results clearly reveal the potential of the ANN approach for recovering the water droplet mean size within a cloud bank. The mean error associated with the ANN-recovered droplet mean size relative to the true droplet mean size is 3.22% for the training cases and 4.81% for the test cases. The relative error is even less when only droplet mean sizes of larger than 10 μm are considered. The relative error in the ANN prediction of the small (and statistically unlikely) droplet mean sizes can approach 70%, as indicated in Fig. 8.12.

Training and test dataset results for the cloud liquid water content are shown in Figs. 8.13 and 8.14. The ANN-recovered values are once again in excellent agreement with the target values. Essentially all of the recovered results in Fig. 8.13 fall within $\pm 10\%$ of the target values, with a mean training error of 2.20% and a mean test error of 2.68%. Figure 8.14 shows the variation of relative error in the prediction of cloud liquid water content with the target value for both the training and test data.

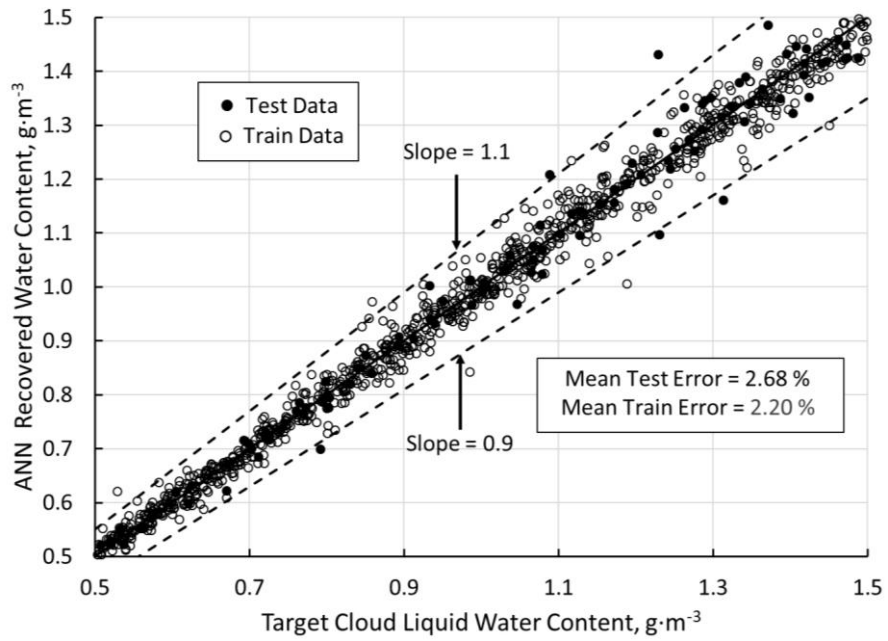


Figure 8.12. Comparison of ANN recovered liquid water content with target liquid water content used in the MCRT-based cloud radiance model.

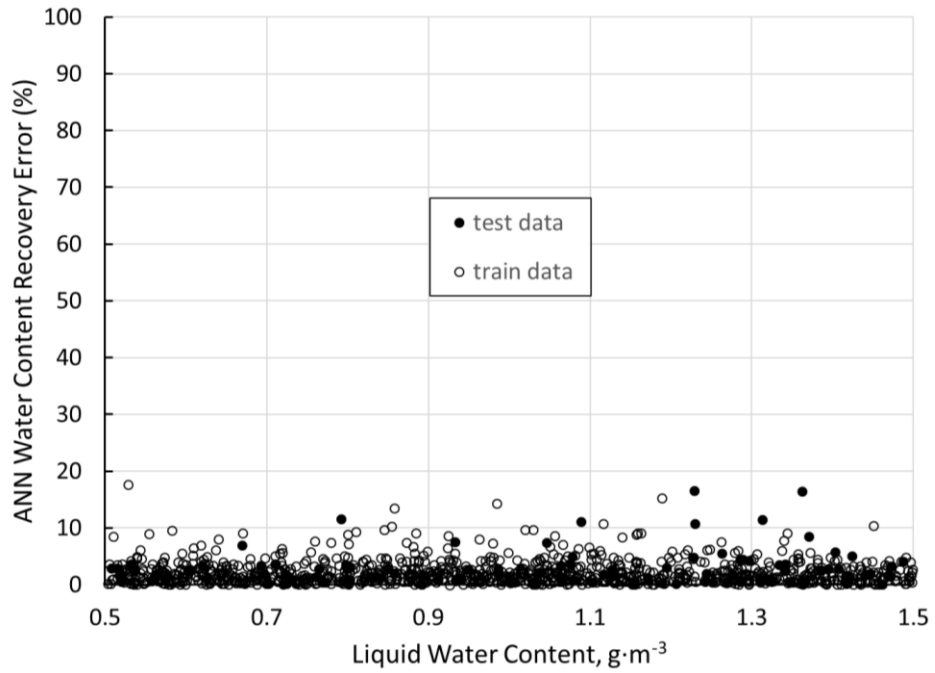


Figure 8.13. Variation of ANN liquid water content recovery error with liquid water content.

The results for water droplet mean size and cloud liquid water content show that the ANN recovery accuracy for both training and test data is very high. These results demonstrate the potential of using the ANN model as an alternate approach to the recovery of cloud properties from sun-photometer measurements.

8.5. Discussion

A cardinal rule of ANN modeling is that the input and output parameters must be causally independent. The ANN formulation presented here supposes that water droplet size and cloud liquid water content are independent cloud properties but, strictly speaking, this is not the case. Ming et al. [119], Christensen et al. [123], Deaconu et al. [122], Diem and Brown [120], Rosenfeld et al. [121], and Toll et al. [124], all explore the role of dry aerosols such as sea salt, pollen, desert sand, and volcanic ash in determining the size, number, and survival time of liquid water droplets formed in air masses having more or less the same cloud-forming potential. The apparent success of the ANN developed and demonstrated here is due to the fact that, while a causal relationship probably does exist between cloud droplet size and liquid water content, it is of second-order importance compared to other influences, and so any correlation that may exist between them is sufficiently weak that the independence requirement is not violated.

We have already pointed out that a first-principle MCRT model based on Mie scattering is the source of both the training and the test datasets used to compose our ANN model. This is necessitated by the sheer volume of data required. It might be argued that, even though the model produces angular distribution profiles having the same features and general shape as those reported in the literature, they are not based on real cloud sun-photometry and thus are of limited utility to the community. Our response to this legitimate concern is that the ANN approach presented here could be part of an iterative scheme in which the MCRT cloud radiance model is informed, and thereby improved, by an ever-growing population

of experimental measurements in which the ANN approach introduced here plays an increasingly important role.

The MCRT model used to build the database which is in turn used to train and test the ANN model can also be criticized on theoretical grounds. Rather than tracing rays through a cloud composed of droplets having a realistic size distribution $n(a)$, from which a mean size could be determined, we chose to trace rays through a cloud composed of liquid water droplet having a uniform size distribution. This approach does not address the reality that water droplet at the cloud tops and bottoms might be smaller than those in the cloud center, which could be important in determining the angular radiance distribution under the cloud.

Furthermore, the Mie single-scattering theory at the heart of the MCRT model does not consider the near-field effect that arises when scattering particles are densely packed [131], as would undoubtedly be the case in a mature water cloud. When Eqs. (8-10) – (8-14) are used to compute the ray mean free path for the range of droplet sizes and liquid water content explored here, values on the order of a few meters are obtained (for example, for $a = 25.6 \mu\text{m}$ and $LWC = 1.0165 \text{ gm}^{-3}$, a mean free path of 4.52 m is found). This mean free path, when used in Eq. (8-9), produces path lengths between scattering events on the order of few tens of meters, depending on the value of the random number used in Eq. (8-9). Therefore, the model is at least internally consistent since the scattering centers are typically separated by thousands of wavelengths. Indeed, Fig. 8.6 establishes that 39 scattering events could account for the distance needed for a ray to traverse the 500-m thick cloud bank. Still, the relatively long ray paths do not address the fact that the electric fields of Mie scattering centers are perturbed by those of near neighbors which otherwise do not directly participate in the scattering event. It should be emphasized that ANN theory is not physics based, but rather is based on observed input-output relationships. Therefore, as the cloud radiance theory

improves under the influence of actual measurements, so will the corresponding ANN model, but this does not necessarily mean that its accuracy will improve.

Finally, the approach suggested here does not address the altitude of the cloud or its vertical position relative to the sun-photometer. This latter distance would be relevant only in a situation in which the distance between the underside of the cloud bank and the measurement station is large compared to the lateral extent of the cloud bank.

8.6. Conclusions and Recommendations

An artificial neural network is presented that successfully predicts the water droplet mean radius a and the cloud liquid water content LWC from five parameters describing the radiance angular distribution profile obtained using simulated sun-photometry. Cloud radiance is simulated using a Monte Carlo ray-trace cloud scattering model based on Mie single-scattering theory. We conclude that a properly trained ANN model holds promise as an alternative method of interpreting sun-photometry measurements in terms of cloud properties. Advantages are that the ANN directly solves what is naturally an inverse problem, and that it does so in real time. A campaign is recommended in which field measurements, either those already available in the literature or new results obtained with this purpose in mind, are used to converge the MCRT cloud radiance model.

References

1. Howell, J.R., *The Monte Carlo Method in Radiative Heat Transfer*. Journal of Heat Transfer, 1998. **120**(3): p. 547-560.
2. Mahan, J.R., *Radiation Heat Transfer: A Statistical Approach*. 2002, Hoboken, New Jersey: John Wiley & Sons.
3. Mahan, J.R., *The Monte Carlo Ray-Trace Method in Radiation Heat Transfer and Applied Optics*. 2019, Hoboken, New Jersey: John Wiley & Sons.
4. Tan, H.P., Zhang, H.C., and Zhen, B., *Estimation of Ray Effect and False Scattering in Approximate Solution Method for Thermal Radiative Transfer Equation*. Numerical Heat Transfer, Part A: Applications, 2004. **46**(8): p. 807-829.
5. Eckert, E.R.G. and Drake Jr, R.M., *Heat and Mass Transfer*. 1959, New York: McGraw-Hill.
6. Gebhart, B., *Heat Transfer*. 2nd ed. 1971, New York: McGraw-Hill.
7. Hottel, H.C. and Sarofim, A.F., *Radiative Transfer*. 1967, New York: McGraw-Hill.
8. Jakob, M., *Heat Transfer, Volume Ii*. 1957, New York: John Wiley & Sons.
9. Kreith, F., *Radiation Heat Transfer for Spacecraft and Solar Power Plant Design*. 1962, Scranton, Pennsylvania: International Textbook Company.
10. Love, T.J., *Radiative Heat Transfer*. 1968, New Jersey: CE Merrill Pub. Co.
11. McAdams, W.H., *Heat Transmission*. 1954, New York: McGraw-Hill
12. Sparrow, E.M. and Cess, R.D., *Radiation Heat Transfer*. 1966, Baltimore, MD: Brookes.
13. Wiebelt, J.A., *Engineering Radiation Heat Transfer*. 1966, New York: Holt, Rinehart and Winston.
14. Gebhart, B., *Surface Temperature Calculations in Radiant Surroundings of Arbitrary Complexity—for Gray, Diffuse Radiation*. International Journal of Heat and Mass Transfer, 1961. **3**(4): p. 341-346.
15. Howell, J.R., *Application of Monte Carlo to Heat Transfer Problems*, in *Advances in Heat Transfer*. 1969, Elsevier. p. 1-54.
16. Mahan, J.R. and Eskin, L.D. *The Radiation Distribution Factor Its Calculation Using Monte Carlo and an Example of Its Application*. in *First UK National Heat Transfer Conference*. 1984. Leeds, UK.
17. Mahan, J.R. and Eskin, L.D. *Application of Monte Carlo Techniques to Transient Thermal Modeling of Cavity Radiometers Having Diffuse-Specular Surfaces*. in *4th Conference on Atmospheric Radiation*. 1981. Toronto, Canada.
18. Daun, K.J., Morton, D.P., and Howell, J.R., *Smoothing Monte Carlo Exchange Factors through Constrained Maximum Likelihood Estimation*. Journal of Heat Transfer, 2005. **127**(10): p. 1124-1128.

19. Loehrke, R.I., Dolaghan, J.S., and Burns, P.J., *Smoothing Monte Carlo Exchange Factors*. Journal of Heat Transfer, 1995. **117**(2): p. 524-526.
20. Yuen, W.W., *The Multiple Absorption Coefficient Zonal Method (Maczm), an Efficient Computational Approach for the Analysis of Radiative Heat Transfer in Multidimensional Inhomogeneous Nongray Media*. Numerical Heat Transfer, Part B: Fundamentals, 2006. **49**(2): p. 89-103.
21. Larsen, M.E. and Howell, J.R., *The Exchange Factor Method: An Alternative Basis for Zonal Analysis of Radiating Enclosures*. Journal of Heat Transfer, 1985. **107**(4): p. 936-942.
22. Lin, S.H. and Sparrow, E.M., *Radiant Interchange among Curved Specularly Reflecting Surfaces—Application to Cylindrical and Conical Cavities*. Journal of Heat Transfer, 1965. **87**(2): p. 299-307.
23. Barker, E., Feldman, L., and Witte, G., *Recommendation for Random Number Generation Using Deterministic Random Bit Generators*. National Institute of Standards and Technology, 2015.
24. Farmer, J.A. and Roy, S.P. *An Efficient Monte Carlo-Based Solver for Thermal Radiation in Participating Media*. in *ASTFE Digital Library*. 2019. Las Vegas, NV: Begel House Inc.
25. Chang, L.C., Yang, K.T., and Lloyd, J.R., *Radiation-Natural Convection Interactions in Two-Dimensional Complex Enclosures*. Journal of Heat Transfer, 1983. **105**(1): p. 89-95.
26. Ramankutty, M.A. and Crosbie, A.L., *Modified Discrete Ordinates Solution of Radiative Transfer in Two-Dimensional Rectangular Enclosures*. Journal of Quantitative Spectroscopy and Radiative Transfer, 1997. **57**(1): p. 107-140.
27. Ismail, K.A. and Salinas, C.S., *Application of Multidimensional Scheme and the Discrete Ordinate Method to Radiative Heat Transfer in a Two-Dimensional Enclosure with Diffusely Emitting and Reflecting Boundary Walls*. Journal of Quantitative Spectroscopy and Radiative Transfer, 2004. **88**(4): p. 407-422.
28. Hayasaka, H., Kudo, K., Taniguchi, H., Nakamachi, I., Omori, T., and Katayama, T., *Radiative Heat Transfer Analysis by Radiation Heat Ray Method, Transactions*. Japan Society of Mechanical Engineering, 1986. **52**: p. 1734-1740.
29. Jinbo, H., Liming, R., and Heping, T., *Effect of Anisotropic Scattering on Radiative Heat Transfer in Two-Dimensional Rectangular Media*. Journal of Quantitative Spectroscopy and Radiative Transfer, 2003. **78**(2): p. 151-161.
30. Ravigururajan, T.S. and Beltran, M.R., *A Model for Attenuation of Fire Radiation through Water Droplets*. Fire Safety Journal, 1989. **15**(2): p. 171-181.
31. Coppalle, A., Nedelka, D., and Bauer, B., *Fire Protection: Water Curtains*. Fire Safety Journal, 1993. **20**(3): p. 241-255.
32. Consalvi, J.L., Porterie, B., and Loraud, J.C., *On the Use of Gray Assumption for Modeling Thermal Radiation through Water Sprays*. Numerical Heat Transfer: Part A: Applications, 2003. **44**(5): p. 505-519.

33. Berour, N., Lacroix, D., Boulet, P., and Jeandel, G., *Radiative and Conductive Heat Transfer in a Nongrey Semitransparent Medium. Application to Fire Protection Curtains*. Journal of Quantitative Spectroscopy and Radiative Transfer, 2004. **86**(1): p. 9-30.
34. Yang, W., Parker, T., Ladouceur, H.D., and Kee, R.J., *The Interaction of Thermal Radiation and Water Mist in Fire Suppression*. Fire Safety Journal, 2004. **39**(1): p. 41-66.
35. Collin, A., Boulet, P., Lacroix, D., and Jeandel, G., *On Radiative Transfer in Water Spray Curtains Using the Discrete Ordinates Method*. Journal of Quantitative Spectroscopy and Radiative Transfer, 2005. **92**(1): p. 85-110.
36. Li, H.Y., *Inverse Radiation Problem in Two-Dimensional Rectangular Media*. Journal of thermophysics and heat transfer, 1997. **11**(4): p. 556-561.
37. Sarvari, S.M.H., Mansouri, S.H., and Howell, J.R., *Inverse Boundary Design Radiation Problem in Absorbing-Emitting Media with Irregular Geometry*. Numerical Heat Transfer: Part A: Applications, 2003. **43**(6): p. 565-584.
38. Sarvari, S.M.H. and Mansouri, S.H., *Inverse Design for Radiative Heat Source in Two-Dimensional Participating Media*. Numerical Heat Transfer, Part B, 2004. **46**(3): p. 283-300.
39. Berrocal Tito, M.J., Roberty, N.C., Silva Neto, A.J., and Cabrejos, J.B., *Inverse Radiative Transfer Problems in Two-Dimensional Participating Media*. Inverse Problems in Science and Engineering, 2004. **12**(1): p. 103-121.
40. Daun, K.J., Howell, J.R., and Morton, D.P., *Optimization of Transient Heater Settings to Provide Spatially Uniform Heating in Manufacturing Processes Involving Radiant Heating*. Numerical Heat Transfer, Part A: Applications, 2004. **46**(7): p. 651-667.
41. Daun, K.J. and Howell, J.R. *Inverse Design Methods for Radiative Transfer Systems*. in *Fourth International Symposium on Radiative Transfer*. 2004. Istanbul, Turkey: Begel House Inc.
42. Kowsary, F., Pooladvand, K., and Pourshaghaghay, A., *Regularized Variable Metric Method Versus the Conjugate Gradient Method in Solution of Radiative Boundary Design Problem*. Journal of Quantitative Spectroscopy and Radiative Transfer, 2007. **108**(2): p. 277-294.
43. Pourshaghaghay, A., Pooladvand, K., Kowsary, F., and Karimi-Zand, K., *An Inverse Radiation Boundary Design Problem for an Enclosure Filled with an Emitting, Absorbing, and Scattering Media*. International Communications in Heat and Mass Transfer, 2006. **33**(3): p. 381-390.
44. Mehraban, S. and Farahat, S. *A Quasi-Steady Method for Inverse Design and Control of a Two-Dimensional Radiant Oven in Transient State*. in *ICHMT International Symposium on Advances in Computational Heat Transfer*. 2008. Janeiro, Brazil: Begel House Inc.
45. Salinas, C.T., *Inverse Radiation Analysis in Two-Dimensional Gray Media Using the Discrete Ordinates Method with a Multidimensional Scheme*. International Journal of Thermal Sciences, 2010. **49**(2): p. 302-310.

46. Bayat, N., Mehraban, S., and Sarvari, S.M.H., *Inverse Boundary Design of a Radiant Furnace with Diffuse-Spectral Design Surface*. International Communications in Heat and Mass Transfer, 2010. **37**(1): p. 103-110.
47. Amiri, H., Hossein, M.S., and Coelho, P.J., *Inverse Optimal Design of Radiant Enclosures with Participating Media: A Parametric Study*. Heat Transfer Engineering, 2013. **34**(4): p. 288-302.
48. Sarvari, S.M.H., Howell, J.R., and Mansouri, S.H., *Inverse Boundary Design Conduction-Radiation Problem in Irregular Two-Dimensional Domains*. Numerical Heat Transfer: Part B: Fundamentals, 2003. **44**(3): p. 209-224.
49. Kim, K.W., Baek, S.W., Kim, M.Y., and Ryou, H.S., *Estimation of Emissivities in a Two-Dimensional Irregular Geometry by Inverse Radiation Analysis Using Hybrid Genetic Algorithm*. Journal of Quantitative Spectroscopy and Radiative Transfer, 2004. **87**(1): p. 1-14.
50. Mossi, A.C., Vielmo, H.A., França, F.H.R., and Howell, J.R., *Inverse Design Involving Combined Radiative and Turbulent Convective Heat Transfer*. International Journal of Heat and Mass Transfer, 2008. **51**(11-12): p. 3217-3226.
51. Moghadassian, B. and Kowsary, F., *Inverse Boundary Design Problem of Natural Convection–Radiation in a Square Enclosure*. International Journal of Thermal Sciences, 2014. **75**: p. 116-126.
52. Oguma, M. *Solution of Two-Dimensional Blackbody Inverse Radiation Problem by Inverse Monte Carlo Method*. in *ASME-JSME Thermal Engineering Joint Conference*. 1995. Lahaina, Maui.
53. Erturk, H., Ezekoye, O.A., and Howell, J.R. *Inverse Solution of Radiative Heat Transfer in Two-Dimensional Irregularly Shaped Enclosures*. in *International Mechanical Engineering Congress and Exposition (IMECE)*. 2000. Orlando, FL.
54. Baek, S.W. and Kang, S.J., *The Combined Monte-Carlo and Finite-Volume Method for Radiation in a Two-Dimensional Irregular Geometry*. International Journal of Heat and Mass Transfer, 2000. **43**(13): p. 2337-2344.
55. Safavinejad, A., Mansouri, S.H., and Sarvari, S.M.H., *Inverse Boundary Design of Two-Dimensional Radiant Enclosures with Absorbing—Emitting Media Using Micro-Genetic Algorithm*. Proceedings of the Institution of Mechanical Engineers, Part C: Journal of Mechanical Engineering Science, 2007. **221**(8): p. 945-948.
56. Safavinejad, A., Mansouri, S.H., Sakurai, A., and Maruyama, S., *Optimal Number and Location of Heaters in 2-D Radiant Enclosures Composed of Specular and Diffuse Surfaces Using Micro-Genetic Algorithm*. Applied Thermal Engineering, 2009. **29**(5-6): p. 1075-1085.
57. Mosavati, M., Kowsary, F., and Mosavati, B., *A Novel, Noniterative Inverse Boundary Design Regularized Solution Technique Using the Backward Monte Carlo Method*. Journal of Heat Transfer, 2013. **135**(4).
58. Mosavati, B., Mosavati, M., and Kowsary, F., *Solution of Radiative Inverse Boundary Design Problem in a Combined Radiating-Free Convecting Furnace*.

- International Communications in Heat and Mass Transfer, 2013. **45**: p. 130-136.
59. Mulford, R.B., Collins, N.S., Farnsworth, M.S., Jones, M.R., and Iverson, B.D., *Total Hemispherical Apparent Radiative Properties of the Infinite V-Groove with Specular Reflection*. International Journal of Heat and Mass Transfer, 2018. **124**: p. 168-176.
 60. Yarahmadi, M., Mahan, J.R., and Kowsary, F. *A New Approach to Inverse Boundary Design in Radiation Heat Transfer*. in *16th UK Heat Transfer Conference*. 2019. Nottingham, England.
 61. Vick, B., Mahan, J.R., and Yarahmadi, M., *Combined-Mode Conduction/Radiation Heat Transfer Analysis Based on Discrete Green's Functions*. Journal of Heat Transfer, 2020.
 62. Cheng, Y., Li, H., Zhang, J., and Huang, Z., *Solution of Radiative Intensity with High Directional Resolution in Heterogeneous Participating Media and Irregular Geometries by the Null-Collision Reverse Monte Carlo Method*. International Journal of Heat and Mass Transfer, 2020. **152**: p. 119475.
 63. Yarahmadi, M., Mahan, J.R., McFall, K., and Ashraf, A.B., *Numerical Focusing of a Wide-Field-Angle Earth Radiation Budget Imager Using an Artificial Neural Network*. Remote Sensing, 2020. **12**(1): p. 176.
 64. Lloyd, P., *Us Army Is Working on Ai-Guided Missiles That 'Pick Their Own Targets' to Blow up after Scanning Ground Below*, in *DailyMail*. 2019.
 65. Irick, K. and Brown, E. *In-Situ Thermal Rom-Based Optimization Using Borg Moea: A Preliminary Study*. in *Heat Transfer Summer Conference*. 2019. Bellevue, WA: American Society of Mechanical Engineers.
 66. Yarahmadi, M. and Mahan, J.R., *Verification of Two-Dimensional Monte Carlo Ray-Trace Methodology in Radiation Heat Transfer Analysis*. arXiv preprint arXiv:1810.05204, 2018.
 67. Yarahmadi, M., *An Engine for Computing Radiation Distribution Factors for Two-Dimensional Enclosures*. Zenodo, Geneva, Switzerland (epub), 2018. **10**.
 68. Yarahmadi, M., Mahan, J.R., and Priestley, K.J., *Uncertainty Analysis and Experimental Design in the Monte Carlo Ray-Trace Environment*. Journal of Heat Transfer, 2019. **141**(3).
 69. Howell, J.R., *Monte Carlo Treatment of Data Uncertainties in Thermal Analysis*. Journal of Spacecraft and Rockets, 1973. **10**(6): p. 411-414.
 70. Almazan, P.P., *Statistical Error Control for Radiative Software Based on Monte Carlo Methods*. SAE Transactions, 1993: p. 1498-1506.
 71. Taylor, R.P., Luck, R., Hodge, B.K., and Steele, W.G. *Uncertainty Analysis of Diffuse-Gray Radiation Enclosure Problems: A Hypersensitive Case Study*. in *The Fifth Annual Thermal and Fluids Analysis Workshop*. 1993. NASA. Lewis Research Center.
 72. Taylor, R.P., Luck, R., Hodge, B.K., and Steele, W.G., *Uncertainty Analysis of Diffuse-Gray Radiation Enclosure Problems*. Journal of thermophysics and heat transfer, 1995. **9**(1): p. 63-69.

73. Kline, S.J. and McClintock, F.A., *Describing Uncertainties in Single-Sample Experiments,'a Sme Mechanical Engineering, Vol. 75*. Mechanical Engineering, 1953. **75**: p. 3-8.
74. Almazan, P.P. *Accuracy of Monte Carlo Ray-Tracing Thermal Radiation Calculations: A Practical Discussion*. in *Sixth European Symposium on Space Environmental Control Systems*. 1997. Noordwijk, Netherlands.
75. Sánchez, M.C., Mahan, J.R., Ayala, E.A., and Priestley, K.J. *Tools for Predicting Uncertainty and Confidence Intervals in Radiometric Data Products*. in *Sensors, Systems, and Next-Generation Satellites III*. 1999. International Society for Optics and Photonics.
76. Sánchez, M.C., Mahan, J.R., Nevarez, F.J., and Sorensen, I.J. *Bounding Uncertainty in Monte Carlo Ray-Trace Models*. in *Sensors, Systems, and Next-Generation Satellites V*. 2001. International Society for Optics and Photonics.
77. Sánchez, M.C., Nevarez, F.J., Mahan, J.R., and Priestley, K.J. *Uncertainty and Confidence Intervals in Optical Design Using the Monte Carlo Ray-Trace Method*. in *Sensors, Systems, and Next-Generation Satellites IV*. 2001. International Society for Optics and Photonics.
78. Sánchez, M.C., *Uncertainty and Confidence Intervals of the Monte Carlo Ray-Trace Method in Radiation Heat Transfer*. 2002, Ph.D Dissertation, Virginia Tech.
79. Press, W.H., Teukolsky, S.A., Flannery, B.P., and Vetterling, W.T., *Numerical Recipes in Fortran 77: The Art of Scientific Computing*. 2 ed. 1992, Cambridge, England: Cambridge University Press.
80. Yarahmadi, M., Mahan, J.R., and Priestley, K.J., *Estimation and Use of the Radiation Distribution Factor Median for Predicting Uncertainty in the Monte Carlo Ray-Trace Method*. Journal of Heat Transfer, 2019. **141**(6).
81. Yarahmadi, M., Mahan, J.R., and McFall, K., *Artificial Neural Networks in Radiation Heat Transfer Analysis*. Journal of Heat Transfer, 2020.
82. Lin, T.Y. and Tseng, C.H., *Optimum Design for Artificial Neural Networks: An Example in a Bicycle Derailleur System*. Engineering Applications of Artificial Intelligence, 2000. **13**(1): p. 3-14.
83. Thibault, J. and Grandjean, B.P.A., *A Neural Network Methodology for Heat Transfer Data Analysis*. International Journal of Heat and Mass Transfer, 1991. **34**(8): p. 2063-2070.
84. Pacheco-Vega, A., Sen, M., Yang, K.T., and McClain, R.L., *Neural Network Analysis of Fin-Tube Refrigerating Heat Exchanger with Limited Experimental Data*. International Journal of Heat and Mass Transfer, 2001. **44**(4): p. 763-770.
85. Bechtler, H., Browne, M.W., Bansal, P.K., and Kecman, V., *Neural Networks—a New Approach to Model Vapour-Compression Heat Pumps*. International Journal of Energy Research, 2001. **25**(7): p. 591-599.
86. Lazrak, A., Boudehenn, F., Bonnot, S., Fraisse, G., Leconte, A., Papillon, P., and Souyri, B., *Development of a Dynamic Artificial Neural Network Model of*

- an Absorption Chiller and Its Experimental Validation*. Renewable Energy, 2016. **86**: p. 1009-1022.
87. Azizi, S. and Ahmadloo, E., *Prediction of Heat Transfer Coefficient During Condensation of R134a in Inclined Tubes Using Artificial Neural Network*. Applied Thermal Engineering, 2016. **106**: p. 203-210.
 88. Chang, W., Chu, X., Fareed, A.F.B.S., Pandey, S., Luo, J., Weigand, B., and Laurien, E., *Heat Transfer Prediction of Supercritical Water with Artificial Neural Networks*. Applied Thermal Engineering, 2018. **131**: p. 815-824.
 89. Ye, K., Zhang, Y., Yang, L., Zhao, Y., Li, N., and Xie, C., *Modeling Convective Heat Transfer of Supercritical Carbon Dioxide Using an Artificial Neural Network*. Applied Thermal Engineering, 2019. **150**: p. 686-695.
 90. Kaya, M. and Hajimirza, S., *Surrogate Based Modeling and Optimization of Plasmonic Thin Film Organic Solar Cells*. International Journal of Heat and Mass Transfer, 2018. **118**: p. 1128-1142.
 91. Kaya, M. and Hajimirza, S., *Application of Artificial Neural Network for Accelerated Optimization of Ultra Thin Organic Solar Cells*. Solar Energy, 2018. **165**: p. 159-166.
 92. Kamble, L.V., Pangavhane, D.R., and Singh, T.P., *Heat Transfer Studies Using Artificial Neural Network—a Review*. International Energy Journal, 2014. **14**(1).
 93. Mohanraj, M., Jayaraj, S., and Muraleedharan, C., *Applications of Artificial Neural Networks for Thermal Analysis of Heat Exchangers—a Review*. International Journal of Thermal Sciences, 2015. **90**: p. 150-172.
 94. Basheer, I.A. and Hajmeer, M., *Artificial Neural Networks: Fundamentals, Computing, Design, and Application*. Journal of Microbiological Methods, 2000. **43**(1): p. 3-31.
 95. Teng, F., *Application of Neural Networks to Adaptive Control of Nonlinear Systems*, by Gw Ng, Research Studies Press Ltd, Taunton, Uk, 1997. 198 Pages, Isbn 0-471-97263-0. International Journal of Robust and Nonlinear Control: IFAC-Affiliated Journal, 2001. **11**(9): p. 879-880.
 96. Haykin, S., *Neural Networks: A Comprehensive Foundation*. 2007, New Jersey: Prentice-Hall, Inc.
 97. Kingma, D.P. and Ba, J., *Adam: A Method for Stochastic Optimization*. arXiv preprint arXiv:1412.6980, 2014.
 98. Li, Z.L., Becker, F., Stoll, M.P., and Wan, Z., *A Method for Monitoring the Temporal Variation of Surface Spectral Emissivity: Application to Thermal Infrared Multispectral Scanner (Tims) Data in Hapex-Sabel*. Journal of Geophysical Research: Atmospheres, 1999. **104**(D24): p. 31217-31224.
 99. Raj, V.C. and Prabhu, S.V., *A Refined Methodology to Determine the Spatial and Temporal Variation in the Emissivity of Diffusion Flames*. International Journal of Thermal Sciences, 2017. **115**: p. 89-103.
 100. Caldwell, M.E., Spilling, D.A.V., Delderfield, J., Ward, K., and Whalley, M., *Radiometric Characteristics of the Broadband Radiometer (Bbr) Instrument for the*

- Earthcare Mission*. Journal of Atmospheric and Oceanic Technology, 2017. **34**(8): p. 1783-1794.
101. Barkstrom, B.R., *The Earth Radiation Budget Experiment (Erbe)*. Bulletin of the American Meteorological Society, 1984. **65**(11): p. 1170-1185.
 102. Wielicki, B.A., Barkstrom, B.R., Harrison, E.F., Lee III, R.B., Smith, G.L., and Cooper, J.E., *Clouds and the Earth's Radiant Energy System (Ceres): An Earth Observing System Experiment*. Bulletin of the American Meteorological Society, 1996. **77**(5): p. 853-868.
 103. Georgieva, E., Priestley, K., Dunn, B., Cageao, R., Barki, A., Osmundsen, J., Turczynski, C., and Abedin, N., *Radiation Budget Instrument (Rbi) for Jpss-2*. 2015.
 104. Harries, J.E., Russell, J.E., Hanafin, J.A., Brindley, H., Futyan, J., Rufus, J., Kellock, S., Matthews, G., Wrigley, R., and Last, A., *The Geostationary Earth Radiation Budget Project*. Bulletin of the American Meteorological Society, 2005. **86**(7): p. 945-960.
 105. *The Clouds and the Earth's Radiant Energy System (Ceres)*. Available from: <https://ceres.larc.nasa.gov/>.
 106. Pratt, W.K., *Introduction to Digital Image Processing*. 2013, Boca Raton, Florida: CRC press.
 107. Lucy, L.B., *An Iterative Technique for the Rectification of Observed Distributions*. The astronomical journal, 1974. **79**: p. 745.
 108. Richardson, W.H., *Bayesian-Based Iterative Method of Image Restoration*. Journal of the Optical Society of America, 1972. **62**(1): p. 55-59.
 109. Krishnan, N., Muthukumar, S., Ravi, S., Shashikala, D., and Pasupathi, P., *Image Restoration by Using Evolutionary Technique to Denoise Gaussian and Impulse Noise*, in *Mining Intelligence and Knowledge Exploration*. 2013, Springer. p. 299-309.
 110. Saini, D., Purohit, M., Singh, M., Khare, S., and Kaushik, B.K. *Analysis and Comparison of Regularization Techniques for Image Deblurring*. in *Fifth International Conference on Soft Computing for Problem Solving*. 2016. Roorkee , Uttarakhand, India: Springer.
 111. Hongying, Z., Qicong, P., and Yadong, W. *Variational Image Deblurring Using Modified Hopfield Neural Network*. in *International Conference on Communications, Circuits and Systems*. 2006. Guilin, China: IEEE.
 112. Jubien, C.M. and Jernigan, M.R. *A Neural Network for Deblurring an Image*. in *IEEE Pacific Rim Conference on Communications, Computers and Signal Processing*. 1991. Victoria, BC, Canada: IEEE.
 113. Kumar, N., Shrivastava, M., and Rahim, N., *Image Deblurring Using a Neural Network Approach*. International Journal of Engineering and Innovative Technology (IJEIT), 2012. **2**(3).
 114. Reshma Vijay, V.J. and Deepa, P.L., *Image Deblurring Using Convolutional Neural Network*. IOSR Journal of Electronics and Communication Engineering, 2016. **11**: p. 7-12.

115. Schuler, C.J., Christopher Burger, H., Harmeling, S., and Scholkopf, B. *A Machine Learning Approach for Non-Blind Image Deconvolution*. in *IEEE Conference on Computer Vision and Pattern Recognition*. 2013. Portland, Oregon.
116. Ashraf, A.B., Mahan, J.R., Priestley, K.J., and Shankar, M. *Numerical Focusing of a Wide Field-of-View Instrument for Monitoring the Planetary Energy Budget*. in *Multidisciplinary Digital Publishing Institute Proceedings*. 2019.
117. Subashini, P., Krishnaveni, M., and Singh, V., *Image Deblurring Using Back Propagation Neural Network*. *World Comp Sci Inf Technol J*, 2011. **1**(6): p. 277-282.
118. Ashraf, A.B., *A New Paradigm for End-to-End Modeling of Radiometric Instrumentation Systems*. 2020, Ph.D Dissertation, Virginia Tech.
119. Ming, Y., Ramaswamy, V., Donner, L.J., Phillips, V.T.J., Klein, S.A., Ginoux, P.A., and Horowitz, L.W., *Modeling the Interactions between Aerosols and Liquid Water Clouds with a Self-Consistent Cloud Scheme in a General Circulation Model*. *Journal of the atmospheric sciences*, 2007. **64**(4): p. 1189-1209.
120. Diem, J.E. and Brown, D.P., *Anthropogenic Impacts on Summer Precipitation in Central Arizona, U.S.A*. *The Professional Geographer*, 2003. **55**(3): p. 343-355.
121. Rosenfeld, D., Zhu, Y., Wang, M., Zheng, Y., Goren, T., and Yu, S., *Aerosol-Driven Droplet Concentrations Dominate Coverage and Water of Oceanic Low-Level Clouds*. *Science*, 2019. **363**(6427): p. eaav0566.
122. Deaconu, L.T., Ferlay, N., Waquet, F., Peers, F., Thieuleux, F., and Goloub, P., *Satellite Inference of Water Vapour and above-Cloud Aerosol Combined Effect on Radiative Budget and Cloud-Top Processes in the Southeastern Atlantic Ocean*. *Atmos. Chem. Phys.*, 2019. **19**(17): p. 11613-11634.
123. Christensen, M.W., Jones, W.K., and Stier, P., *Aerosols Enhance Cloud Lifetime and Brightness Along the Stratus-to-Cumulus Transition*. *Proceedings of the National Academy of Sciences of the United States of America*, 2020. **117**(30): p. 17591-17598.
124. Toll, V., Christensen, M., Quaas, J., and Bellouin, N., *Weak Average Liquid-Cloud-Water Response to Anthropogenic Aerosols*. *Nature*, 2019. **572**(7767): p. 51-55.
125. Whiteman, D.N. and Melfi, S.H., *Cloud Liquid Water, Mean Droplet Radius, and Number Density Measurements Using a Raman Lidar*. *Journal of Geophysical Research: Atmospheres*, 1999. **104**(D24): p. 31411-31419.
126. Ritter, J.M., Voss, K.J., and Gordon, H.R. *A New Instrument for Shipborne Radiometric Measurements of the Solar Aureole*. in *American Geophysical Union/Mineralogical Society of America Spring Meeting*. 1997. Baltimore, MD, U.S.A.
127. DeVore, J.G., Stair, A.T., LePage, A., Rall, D., Atkinson, J., Villanucci, D., Rappaport, S.A., Joss, P.C., and McClatchey, R.A., *Retrieving Properties of Thin*

- Clouds from Solar Aureole Measurements*. Journal of Atmospheric and Oceanic Technology, 2009. **26**(12): p. 2531-2548.
128. Mahan, J.R., Carnicero, B.A., Nevarez, F.J., and Sorensen, I.J. *Novel Solar Aureolometer Concept Based on Reflective Optics*. in *Design and Engineering of Optical Systems II*. 1999. International Society for Optics and Photonics.
129. Bohren, C.F. and Huffman, D.R., *Absorption and Scattering of Light by Small Particles*. 2008: John Wiley & Sons.
130. Mätzler, C. *Matlab Functions for Mie Scattering and Absorption (Version 2)*. in *Research Report of the Institut für Angewandte Physik*. 2002. University of Bern
131. Bressel, L. and Reich, O., *Theoretical and Experimental Study of the Diffuse Transmission of Light through Highly Concentrated Absorbing and Scattering Materials: Part I: Monte-Carlo Simulations*. Journal of Quantitative Spectroscopy and Radiative Transfer, 2014. **146**: p. 190-198.
132. Pelkowski, J. and Frisius, T., *The Theoretician's Clouds—Heavier or Lighter Than Air? On Densities in Atmospheric Thermodynamics*. Journal of the atmospheric sciences, 2011. **68**(10): p. 2430-2437.

